

SONOCHEMICAL SYNTHESIS OF MOLYBDENUM DISILICIDE (MoSi_2)

AFOSR Grant No. F 49620-93-1-0131

Final Technical Report

**S.M.L. Sastry
W.E. Buhro
R. Suryanarayanan
T.J. Trentler**

**Washington University
St. Louis, MO. 63130**

DTIC QUALITY INSPECTED 2

**Submitted to
Air Force Office of Scientific Research
Attention: Major C. Ward
Building 410
Bolling Air Force Base
Washington, D.C. 20332**

October 22, 1997

19971119 114

DISTRIBUTION STATEMENT A

**Approved for public release;
Distribution Unlimited**

ABSTRACT

Solution phase synthesis (SPS) is a promising approach for producing nanometer-scale particles of metals, intermetallics, and ceramics. In this method, chemical reactions are conducted at low temperatures ($<200^{\circ}\text{C}$) in solution to form solid precursors which are subsequently annealed in the solid state at temperatures of $500\text{--}1000^{\circ}\text{C}$ to produce by nucleation and growth $10\text{--}100\text{ nm}$ crystallites. With such nanoparticles, consolidation temperatures required for full densification are significantly reduced and secondary processing/fabrication can be carried out at much lower temperatures.

Two successful solution phase synthesis methods were developed for the preparation of nanocrystalline ($<100\text{ nm}$ size) MoSi_2 . The first method consisted of coreducing molybdenum and silicon halides by NaK alloy in an ultrasonically agitated hydrocarbon solvent followed by thermal processing at $<1000^{\circ}\text{C}$ under vacuum to eliminate byproduct salts. MoSi_2 crystallites averaging $20\text{--}50\text{ nm}$ were obtained. Solvent degradation during this process resulted in the incorporation of substantial carbonaceous impurity (believed to be SiC) in these products. To eliminate the carbon, similar solventless reductions (without ultrasound) were conducted in molten magnesium, but average particle sizes have not been refined into the nanometer regime (currently $100\text{--}200\text{ nm}$). The second method was the reaction of MoCl_3 and Si in the solid state. These reactants underwent an ignition at approximately 500°C that resulted in the evolution of SiCl_4 and the formation of MoSi_2 crystallites. Crystallite size was dependent on reaction scale and was only nanocrystalline for very small scales. Addition of an inert salt to the reaction mixture, however, moderated the exothermic process and allowed for the preparation of nanocrystalline product (50 nm).

A micromechanism based model was developed for nanoparticle densification during uniaxial and hydrostatic pressing. The model takes into account the effects on densification of agglomeration, bulk and surface impurities, fewer dislocations per particle, low stability of dislocations due to fine size, and other factors unique to nanoparticle systems. The model is applicable to a general nanoparticle system, and is capable of predicting density, densification rate(s), dominant densification mechanism(s), and microstructural features, as a function of consolidation parameters. Nanoparticles were compacted by vacuum hot pressing, or inert -atmosphere hot pressing, and/or hot isostatic pressing using a range of process variables. Precision density measurements and metallography were performed on the as-pressed samples. A good agreement of model predictions with experimental data was observed for a wide range of material and processing variables.

Microhardness, bend strength, compression strength, ductility, and toughness were determined for the consolidated nanocrystalline MoSi_2 . Significant strength increases were observed for nanocrystalline MoSi_2 . However, the expected improvements in fracture toughness and ductility were not observed presumably because of high levels of carbon and oxygen in the particles and residual porosity in the compacts.

TABLE OF CONTENTS

1. INTRODUCTION.....	3
2. OBJECTIVES OF THE PROGRAM.....	5
3.SYNTHESIS OF NANOCRYSTALLINE MoSi ₂	7
3.1 Solution-Based Coreduction Route to <i>nano</i> -MoSi ₂	7
3.2 Preparation of MoSi ₂ by Metallothermic Reactions.....	28
3.3 Solid-State Route to MoSi ₂	36
4. CONSOLIDATION OF NANOPARTICLES.....	54
4.1 Development of Micromechanistic Model.....	54
4.2 Comparison of Model Predictions with Experimental Measurements...	72
5. MECHANICAL PROPERTIES OF NANOCRYSTALLINE MoSi ₂	87
6. CONCLUSIONS.....	91
REFERENCES.....	94
APPENDIX A Material Property Data.....	99

1. INTRODUCTION:

The field of nanophase materials is recognized as an emerging technology that holds promise for producing radical improvements in materials. Success of nanophase material technology depends on demonstration of the interrelationships between synthesis and processing, structural details, and mechanical properties. The potential of nanophase materials has not been fully realized because the programs hitherto have emphasized either processing or structural characterization without adequate property evaluation. The principal objective of our AFOSR program is a systematic investigation of the processing-structure-property correlations of nanocrystalline MoSi_2 produced by solution phase synthesis (SPS).

Solution-phase processing is an extremely promising new strategy for producing nanometer-scale particles of metals, intermetallics, and ceramics. In this method solution-phase chemical reactions are conducted at low temperatures ($<200^\circ\text{C}$) in solution to afford conversion of solid precursors to nanocrystalline particles. The solid precursors obtained from such solution-phase reactions are extremely reactive powders comprising very small primary particles (1-5 nm). These reactive powders are subsequently annealed in the solid state at temperatures of about $500\text{-}1000^\circ\text{C}$, resulting in the nucleation and growth of 10-100 nm crystallites.

The synthesis routes used to produce nanocrystalline particles are diverse and result in nanoparticles with a range of characteristics, such as, size, size distribution, morphology, composition, defects, impurities, and agglomeration (for reviews on this subject see Refs. [1-4]). An inseparable element of nanostructured materials development is the consolidation of particles into useful product forms that preserve the inherent benefits of ultrafine grain size and nanosize reinforcements. Increased bulk and grain boundary diffusion rates coupled with fine grain size will have a dramatic effect on reducing the time, temperature, and pressure for complete densification of nanocrystalline particles. Successful consolidation to near theoretical densities of nanocrystalline particles presents several challenges. The densification behavior of nanoparticles was studied by modeling as well as experimental measurements. Hot isostatic pressing (HIP) diagrams/maps which identify the dominant mechanisms and predict densification rates and times as functions of temperature and pressure are being developed and the model predictions were validated by experimental measurements of densification of nanocrystalline compacts as functions of temperature, pressure, and time.

MoSi_2 with its high strength to weight ratio, retention of strength at high temperatures, large thermal conductivity, and low thermal expansion coefficient is an attractive material for advanced gas turbine engine applications requiring service temperatures greater than possible with nickel-base superalloys. However, low temperature fracture toughness and high temperature creep resistance of MoSi_2 are not adequate for damage critical applications. With the objective of improving the room temperature toughness and high temperature creep resistance of MoSi_2 , several

approaches have been tried [5-12]; but the results obtained thus far are only mildly encouraging. One of the objectives of our program, was to determine whether significant improvements in low temperature toughness can be obtained through grain refinement down to the nanometer regime. Nanograined materials exhibit a drastically altered defect structure compared to coarser grained counterparts in that grain boundaries are abundant. The nanometer grains, and large number of grain boundaries lead to low dislocation density, increased grain boundary diffusion and sliding and dissipation of crack tip stresses by crack deflection and splitting at grain boundaries. Such processes should result in improved toughness. The research presented herein was conducted to determine whether the onset of grain boundary sliding could improve fracture toughness at low temperatures. The differences in deformation behavior of nanocrystalline and conventional MoSi_2 were studied by microhardness measurements, compression and three-point bend testing, and microstructural observations of deformed specimens. The extent of toughening improvements was determined by analyzing cracks formed at microhardness indentations.

2.. OBJECTIVES OF THE PROGRAM

The objectives of the program were to (I) produce by solution phase synthesis nanosized MoSi_2 powder particles, (ii) determine the purity, size distributions, morphologies, crystal structures, and microstructures of nanosize particles, (iii) determine the thermal stability and phase evolution as functions of temperature and time, (iv) develop densification models by taking into account the fine particle sizes, faster diffusion rates, and presence of impurities in ultrafine powders, (v) determine consolidation characteristics and mechanical lproperties of nanosize particles consolidated by different combinations of hot pressing and hot isostatic pressing, and (vi) determine the effects of processing parameters and consolidation variables on microstructures and mechanical properties of nanocrystalline MoSi_2 .

The following is a brief description of our approach for accomplishing the program objectives.

Survey of Sonochemical Reaction Conditions:

Establish the ability to reliably produce nanocrystalline MoSi_2 . Establish the beneficial effects of sonochemical promotion on the co-reduction synthesis of nanocrystalline MoSi_2 . Investigate the effects of sonochemical reaction variables on the stoichiometries, crystallinities, compositional homogeneities, sizes and size distributions, and chemical purities of nanocrystalline MoSi_2 particles. Perform thermal annealing studies of nanocrystalline MoSi_2 . Produce sufficient quantities of nanocrystalline MoSi_2 powders for initial consolidation experiments.

Evaluation of Sizes, Morphologies, and Stabilities of Molybdenum Silicide Nanoparticles.

Optimize the sonochemical annealing conditions for nanocrystalline MoSi_2 . Optimize the sonochemical procedure to produce chemically pure nanocrystalline MoSi_2 . Optimize the reaction conditions to produce preferred nanostructures, in terms of particle morphologies and size distributions. Investigate the surface capping of the MoSi_2 nanoparticles and/or the use of polymeric dispersants during the sonochemical synthesis in order the control nanostrucutres.

Refinement of Nanostructural control and large-scale Procedure

Establish nanostructural control in the sonochemical synthesis such that a variety of morphologies and size distributions may be reliably produced. Establish which nanoparticle-synthesis conditions ultimately produce consolidated nanocrystalline MoSi_2 phases having the most desirable properties.

Thermal Stability and Phase Evolution of Nanocrystalline Molybdenum Silicide Intermetallics.

Determine by X-ray diffraction, scanning electron microscopy and transmission electron microscopy size distributions, morphologies, chemical composition, and crystal structures of phases in as synthesized powders and powders annealed at 400-1400 °C.

Consolidation and Mechanical Properties Evaluation of Nanocrystalline Molybdenum Silicide Intermetallics.

Evaluate different consolidation strategies and determine the optimum conditions for consolidating to full density the nanocrystalline powders . Develop and validate a densification model for the consolidation of nanocrystalline particles by incorporating the unique characteristics of nanoparticles. Determine the room temperature microhardness of the compacts and assess the ductilities of the compacts with slip line markings and extent of cracking in the vicinity of microhardness indentations. Deform selected samples at room temperature under compression and determine strength, ductility, and fracture toughness.

3.SYNTHESIS OF NANOCRYSTALLINE MoSi₂

3.1 Solution-Based Coreduction Route to *nano*-MoSi₂

Solution-based methods to prepare nanocrystalline materials may afford discrete nanocrystallites, and they are potentially as versatile or more so (homogeneous and heterogeneous chemical mixtures may afford extensive alloying possibilities) than other strategies. Indeed, a wide variety of solution-based nanoparticle preparations have appeared in the literature. Most of these preparations, however, have been of metals, metal oxides, and semiconductors, not of high-melting intermetallics or structural ceramics. Our work represents the first time that MoSi₂ has been produced by solvent-based chemical procedures.

General Procedures and Instrumentation. Manipulations were carried out under an atmosphere of dry N₂ using standard-inert atmosphere techniques. SiCl₄ (Hulls) was distilled and stored under N₂. MoCl₅ (99.5%) (Alfa-Aesar or Stream) was used as received. K stick (Stream) and Na lump (Aldrich) were rinsed with hexane, dried *in vacuo* and then combined to form the liquid Na_xK_y alloy. Hexane was distilled from sodium benzophenone ketyl and stored under N₂ over type 4A sieves. Elemental analyses were performed by Galbraith Laboratories, Inc. Carbon content was determined with a Leco induction furnace (capable of refractory carbide analysis), and molybdenum, silicon, and chlorine quantities were established by the lithium borate fusion method.

Ultrasonic reactions were conducted using equipment from Sonics and Materials. A VC 600 processor was used to operate a 3/4" diameter, direct-immersion horn. This equipment provided ultrasonic irradiation with a frequency of 20 kHz and a maximum power of 600 W. A stainless steel adjustable adapter was used to mount a sonication flask (3-neck, 250 mL capacity) to the titanium horn. This adapter simply screws onto the horn, so the assembly was not air tight as received. Consequently, an O-ring groove was machined into the adapter above the threads. The O-ring seal rendered the assembly suitable for inert atmosphere and vacuum (10⁻³ torr) service. This ultrasonic assembly is depicted in Figure 3.1. For the reaction system described below, it can be used for reaction scales of up to ~ 6 g of MoSi₂ (theoretical). This capacity was doubled by elongating the flask to match the threshold at which ultrasonic agitation dissipated. Efficient processing of increased reaction scales will require larger immersion horns or assisted-mixing strategies.

High-Speed stirring was accomplished using a Talboys Instrument Corp. model 104 motor (5000 r.p.m.) equipped with a stainless-steel (Teflon is not compatible with NaK alloy) propeller blade. Stirring was completed in an inert atmosphere dry-box under N₂.

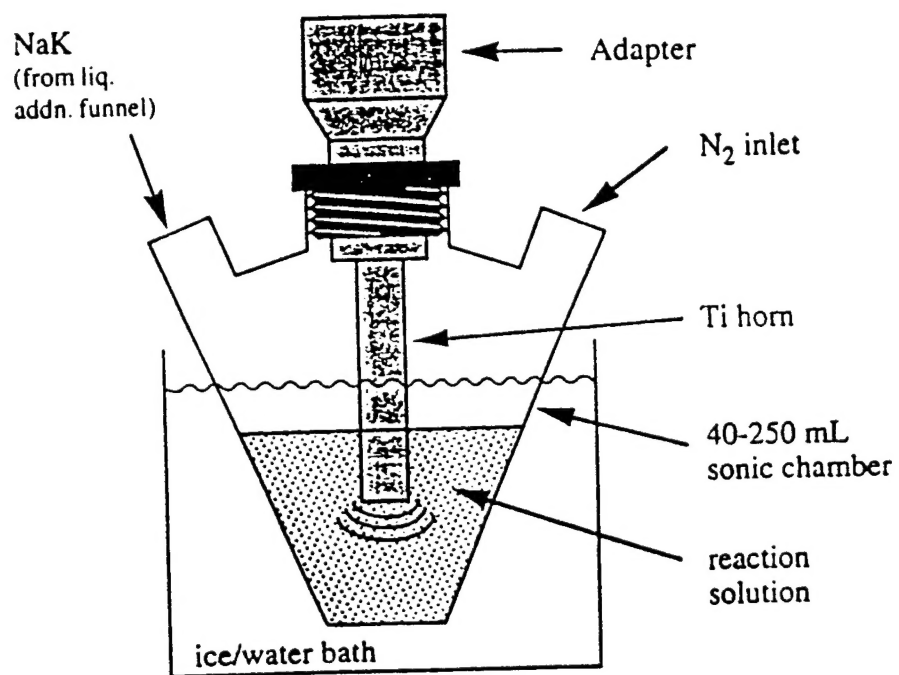


Figure 3.1 The ultrasonic assembly used for preparing MoSi_2 (6 g capacity)

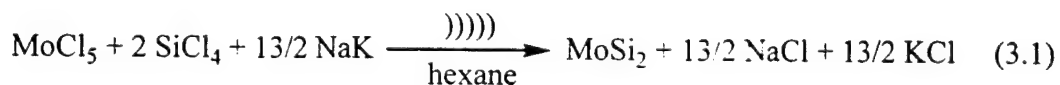
XRD data were collected on a Rigaku DmaxA diffractometer and were analyzed using Materials Data, Inc. software. JCPDS reference patterns were used for identification of crystalline phases. Coherence lengths were calculated by the JADE X-ray powder data processing program. Reported values for α - MoSi_2 correspond to the average of the values calculated for the four strongest reflections appearing below $50^\circ 2\theta$. For β - MoSi_2 , the value of the 100% reflection is given. XRD samples of crude " MoSi_2 " reaction precipitates were prepared under a thin film of PVT, whereas XRD samples of products subjected to subsequent thermal treatments were prepared in air. TEM analysis was performed on a JEOL 2000 FX microscope operating at 200 keV. EDS analyses of elemental compositions were achieved using a Noran Voyager X-ray spectrometer. TEM specimens were prepared on Cu grids covered with a holey carbon film.

Preparation of " MoSi_2 " Precursor Powders Using Ultrasonic Mixing. In a typical preparation MoCl_5 (10.777 g, 39.447 mmol) was added to a sonication flask (250 mL capacity)/horn assembly. Subsequently, dry hexane (150.0 mL) was added, and then SiCl_4 (13.6 mL, 119 mmol) was injected into the hexane. Though MoCl_5 is not soluble in hexane, the solution took on an orange coloration. The horn immersed about 1 cm into the solvent. $\text{NaK}_{3.54}$ alloy (25.000 g, 702.98 mmol Na + K) was added to a pressure-equalizing addition funnel (with a liberally greased glass stopcock, not teflon). The reaction flask was immersed in an ice-water bath, and the $\text{NaK}_{3.54}$ alloy was added dropwise to the reaction flask while sonicating the mixture. A 50% duty cycle (irradiating the solution half of every 3 seconds) was implemented, and the processor was set to provide ultrasound of maximum intensity (amplitude). $\text{NaK}_{3.54}$ addition required approximately 40 minutes, and once complete, continuous ultrasonic irradiation was applied for 30 minutes at full amplitude. A thick brown suspension was formed from which the solvent was stripped in vacuo. This product was collected and stored under N_2 pending further processing to isolate MoSi_2 . The crude yield of precipitates including byproduct salts was 94.5 %. *Warning: This reaction should be conducted with extreme care, as NaK is a very reactive, air and moisture sensitive, reducing agent, and this reactivity is exacerbated here by the implementation of high-intensity ultrasound. Accidental explosions or fires are possible.*

Preparation of Precursor Powders Using High-Speed Stirring. MoCl_5 (40.008 g, 146.44 mmol) was weighed into a 4 L beaker, and then hexane (2 L) was added, followed by SiCl_4 (74.9 g, 441 mmol). $\text{NaK}_{3.54}$ (90.8 g, 2.55 mol) was added dropwise from a pressure-equalizing addition funnel while the mixture was stirred at 5000 r.p.m. NaK addition took 2 hours to complete, and stirring was continued for an additional 2 hours. A dark grey precipitate was obtained under a colorless supernatant. The hexane was decanted, and the product was transferred to a Schlenk flask where it was dried *in vacuo*. The precipitate yield was 86.5 %.

Thermal Processing. Reaction products were heated under dynamic vacuum (10^{-3} torr) to remove byproduct salts by sublimation. Initial heating was accomplished in a Schlenk flask immersed in an oil bath at about 200°C to eliminate volatiles and excess NaK, which occurs rapidly and potentially violently due to the rapid evolution of a noncondensable gas. Subsequently, most samples were heated in quartz tubes inserted into a Lindbergh tube furnace. The furnace was typically programmed for a 20°C/min ramp to 900°C. Soak times to eliminate salt were variable as this depended on sample quantity. (For a 6 g scale, 2-3 hours was adequate, whereas a few minutes sufficed for a scale of a few hundred milligrams.) Some samples bumped extensively when at 900°C, and use of a static vacuum for the bulk of sublimation minimized this problem. Furthermore, unreacted alkali metals reacted with the quartz tubes, which could lead to tube failure, as could cool down after incomplete sublimation (contraction of molten salts on solidification). For these reasons, a reusable annealing tube was designed out of the corrosion resistant alloy, Haynes[®] 556TM, which is illustrated in Figure 3.2.

Synthesis. The strategy used for the production of nanocrystalline molybdenum silicide powders was the coreduction of molybdenum and silicon chlorides with alkali metal in hexane. Equation 3.1 shows the idealized reaction using 1:1 NaK alloy and MoCl₅ as the molybdenum source. (Reactions have also been performed using MoCl₃, which requires less reducing agent and generates less byproduct salts to be removed. Preparations of this compound from MoCl₅ in organic solvents, however, often include substantial carbonaceous impurities which can contribute to the formation of carbide phases, which is a difficulty for this solution-based strategy.) To minimize the formation of Mo₅Si₃, however, a 3:1 molar ratio of SiCl₄:MoCl₅ (with a corresponding excess of NaK) was used for most reactions. The reaction system is heterogeneous as NaK and MoCl₅ are both insoluble in hexane, so high-intensity ultrasound was implemented to efficiently mix the system and accelerate reaction. NaK (or often the eutectic or other compositions) was used as reducing agent rather than sodium alone because NaK is molten at room temperature. The use of insoluble solid powders for the reduction of metal halides has been previously shown to result in the inclusion of substantial quantities of unreacted halides in reaction products, which is attributable to inadequate mobility of the solid.



Nanocrystalline MoSi₂ was not precipitated directly from the solution-based reaction. Products were amorphous aside from alkali metal salts according to XRD (Figure 3.3), and they are believed to have consisted of incompletely reduced reactants, despite the use of a strong liquid reducing agent. TEM images showed large, amorphous grains several hundred nanometers to a couple of microns across (Figure 3.4) that possessed a texture of poorly resolvable features of ~ 1 nm in size. The chemical composition of the grains consisted of an intimate mixture of Mo, Si, Cl, Na, and K

according to EDS, but the ratio of these elements was variable. Furthermore, discrete particles of Mo, Si or Mo_xSi_y phases could not be resolved within the grains.

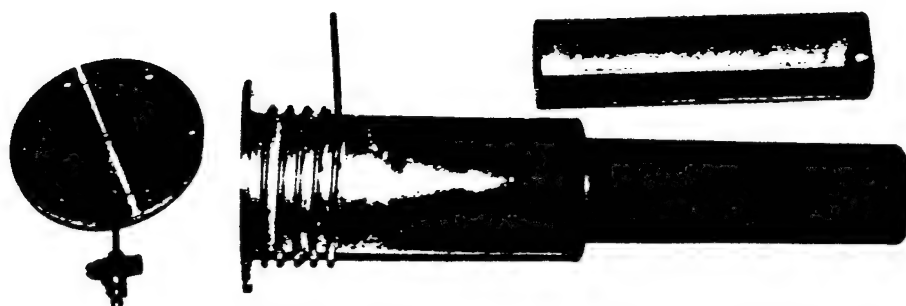


Figure 3.2 A reusable annealing tube made of Haynes 556 designed for thermal processing of crude MoSi_2 powders. The boat (top) containing sample is inserted into the narrow end of the tube (inserted into the furnace), and byproduct salts collect in the wide end. The end-cap (made of stainless steel) has a viton O-ring that forms a vacuum tight seal. The O-ring is kept cool by running cold water through the coil on the wide end of the tube. Not pictured is a cover panel that has been added to the end-cap to block byproducts from entering and clogging the exit tube while heating under dynamic vacuum.

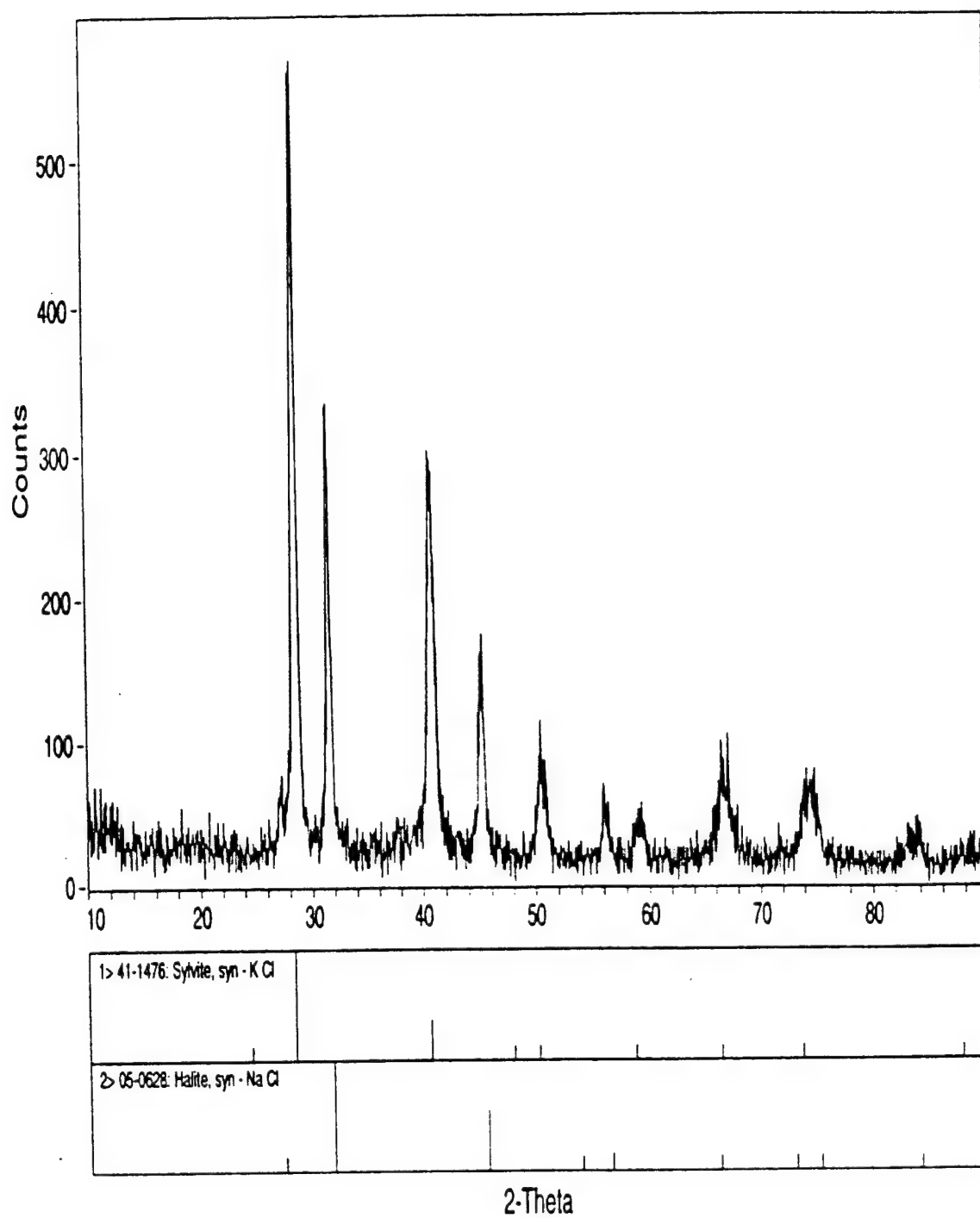


Figure 3.3 XRD pattern of a sonochemical reduction precipitate. Only byproduct salts exhibit crystallinity.



Figure 3.4 TEM images of a sonochemical reduction precipitate. Scale bars are 20 nm (top) and 5 nm.

Convergence of the electron beam on grains caused shrinkage and a dramatic reduction in Cl, Na, and K content, which may constitute resumed reduction of molybdenum and silicon halides under the heat induced by the electron beam.

In addition to microscopy, the detection of HCl fumes (a byproduct of SiCl_4 hydrolysis) emanating from reaction solvents stripped from the precipitates supports the conclusion that the precipitates contained partially reduced reactants. Incomplete reaction is a reasonable consequence of the heterogeneous reaction system. Though NaK is molten, it would still be prone to entrapment by the solid products and byproducts as a reaction proceeds, which would isolate it from reactants and diminish its mobility. Further, NaK could have been consumed by over-reduction of some of the Si with the formation of solid alkali metal silicides or Zintl phases.

The reductions were completed by heating the precipitates under vacuum (10^{-3} torr). An exothermic reaction, which may correspond to the process observed in the TEM, generally initiated at temperatures below 200°C to as low as room temperature. Normally the initiation temperature was between 130°C and 180°C . During this exotherm, unreacted NaK alloy was expelled from the powder, and a gas that was not condensable in a liquid N_2 trap was evolved. The extent of the exotherm, both in terms of amount and rate of expelled NaK and volatiles, was variable. Sometimes a slow venting of gas and NaK occurred over several minutes, but normally a rapid process initiated that was completed in seconds. This could be violent when much gas was evolved rapidly, as a large scale (28 g) reaction did explode (with evacuation at room temperature). The heat generated by the exotherm is presumed to have frequently resulted in transient melting of byproduct salts, as brown precipitate powders often fused into black, granular solids.

Some post-exotherm products were washed with deionized water (to remove byproduct salt) and characterized. XRD patterns still indicated substantial amorphous or poorly crystallized material. The predominate crystalline component was always Mo, which generally possessed a crystalline coherence length of 10-15 nm (Figure 3.5a). Sometimes, however, the Mo was poorly crystallized (≤ 3 nm) according to XRD (Figure 3.5b). This appeared to be a consequence of a less vigorous exotherm. TEM images on the product of Figure 3.5A showed some well-defined Mo particles in an amorphous, Si rich matrix (Figure 3.6). The particle sizes were consistent with the XRD pattern. The preponderance of Mo rather than silicide phases by XRD and the segregation of Mo and Si in TEM indicates that the reaction of Equation 3.1 largely failed to precipitate Mo-Si compound phases directly, which was a consequence of the heterogeneity of the reaction system.

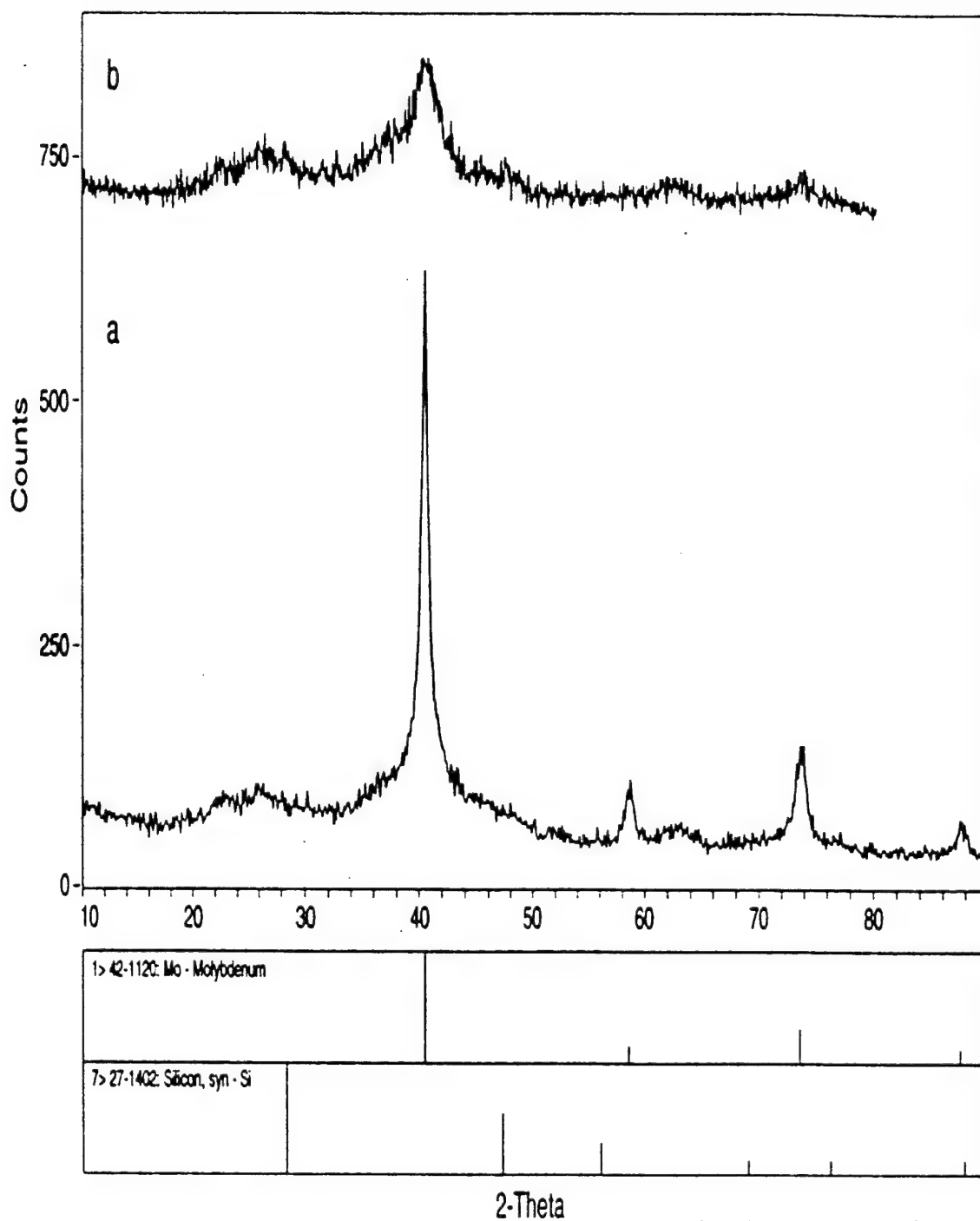


Figure 3.5. XRD patterns of sonochemical reaction products after thermal processing at $< 200^{\circ}\text{C}$ to initiate an exothermic event (byproducts salts removed by water wash). (a) intense exotherm (Mo, 11nm); (b) less intense exotherm (Mo, 3 nm). The broad band at $25^{\circ} 2\theta$ is possibly silaceous material.



Figure 3.6. TEM image of a sonochemical reaction product after low-temperature exothermic ignition (byproduct salts eliminated by water wash). Distinct, dark features are Mo particles.

Molybdenum silicides were obtained by diffusion reactions at higher temperatures. The formation of MoSi_2 , however, was more complicated than mere reaction of Si with Mo, as carbide phases were observed as intermediates. Figure 3.7 illustrates the evolution of MoSi_2 with a series of XRD patterns obtained for powders annealed under dynamic vacuum (10^{-3} torr) at different temperatures. The powders that were annealed at temperatures below the melting point of the byproduct salts ($< 800^\circ\text{C}$) were washed with H_2O to eliminate salt reflections in the XRD patterns (The salts evaporated from the high-temperature samples.). Annealing at 700°C for 1 hour resulted in the conversion of Mo to Mo_2C and $\text{Mo}_{4.8}\text{Si}_3\text{C}_{0.6}$ (the Nowotny phase) exhibiting very poor crystallinity.[14]. With a much longer time at 700°C (12 h), crystallinity improved, but the composition was essentially unchanged. Annealing at 800°C for 12 h resulted in nearly complete conversion to Nowotny phase possessing substantially larger crystallites (32 nm compared to ~ 15 nm). Significant reflections matching MoSi_2 or other non-carbidic silicide phases were not observed. At 900°C , however, these silicide phases rapidly formed. β - MoSi_2 (hexagonal, C40) was often observed in combination with the Nowotny phase after only a few minutes (5-10 min). Within 30 minutes, α - MoSi_2 (tetragonal, C11b) reflections were obtained, and carbide phases were absent. Note that the conversion from the β to the α modification of MoSi_2 was a consequence of crystalline domain size. β - MoSi_2 is preferred for very fine crystallites because it has a higher density, which results in a lower surface area and surface free energy. As crystals grow by diffusion, the surface free energy becomes less significant than the bulk free energy so the crystals convert to the thermodynamically favored lattice structure. Sometimes a small Si reflection was evident in addition to the MoSi_2 reflections owing to the excess SiCl_4 used in the reactions, but more frequently Mo_5Si_3 was observed despite the excess SiCl_4 (Figure 3.8). The average α - MoSi_2 grain sizes determined from XRD line broadening ranged between 17 and 50 nm (normally at least 30 nm), but this can not presently be controlled. Prolonged annealing (12 h) at 900°C resulted in only minor grain growth, but with annealing at higher temperatures (1100°C , 5 h) grains grew out of the nanometer regime (> 100 nm). These results indicate that nanocrystalline MoSi_2 is best obtained by annealing at about 900°C .

Some of the products were characterized by TEM. Samples obtained from annealing at 900°C for at least 30 minutes exhibited average particle sizes that appeared consistent with the XRD determinations, but the size distributions were rather wide (Figure 3.9). The smallest particles were around 15 nm, but a few were larger than 100 nm. The particles lacked faceting and were relatively equiaxed in morphology. The particles were grouped into large agglomerates, but not much sintering was apparent. However, the particles in these agglomerates often appeared to be embedded within an amorphous, silicon rich matrix, so they may not have been held together by mere electrostatic forces.

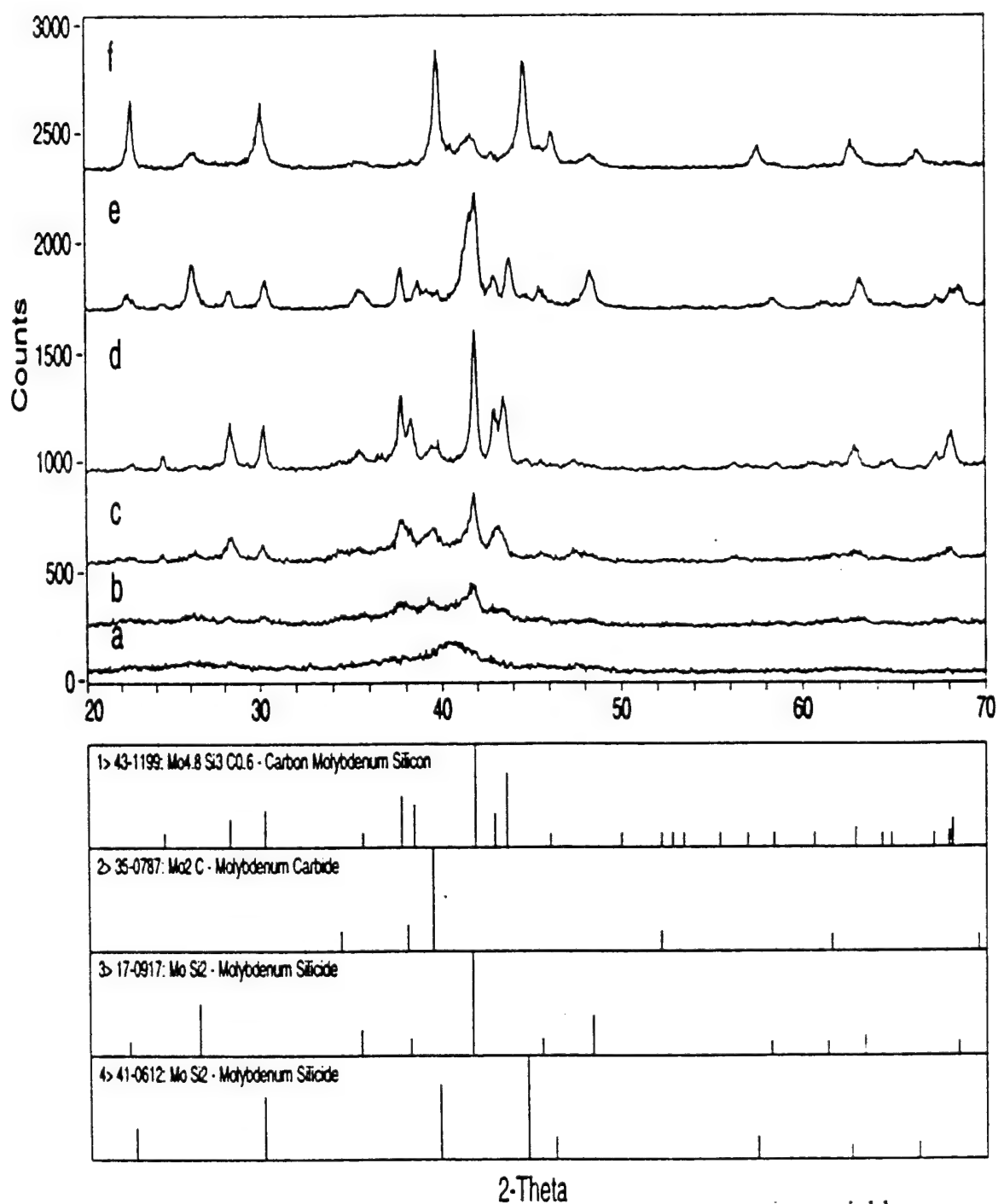


Figure 3.7 XRD patterns of sonochemical reaction products annealed at different temperatures. (a) 200 °C, only Mo; (b) 700 °C, 1h Mo₅Si₃C; (c) 700 °C, 12h, Mo₅Si₃C, Mo₂C; (d) 800°C, 12h, Mo₅Si₃C and some, Mo₂C; (e) 900°C, 5 min; β MoSi₂, Mo₅Si₃C; (f) 900°C 55 min. α MoSi₂ and β MoSi₂

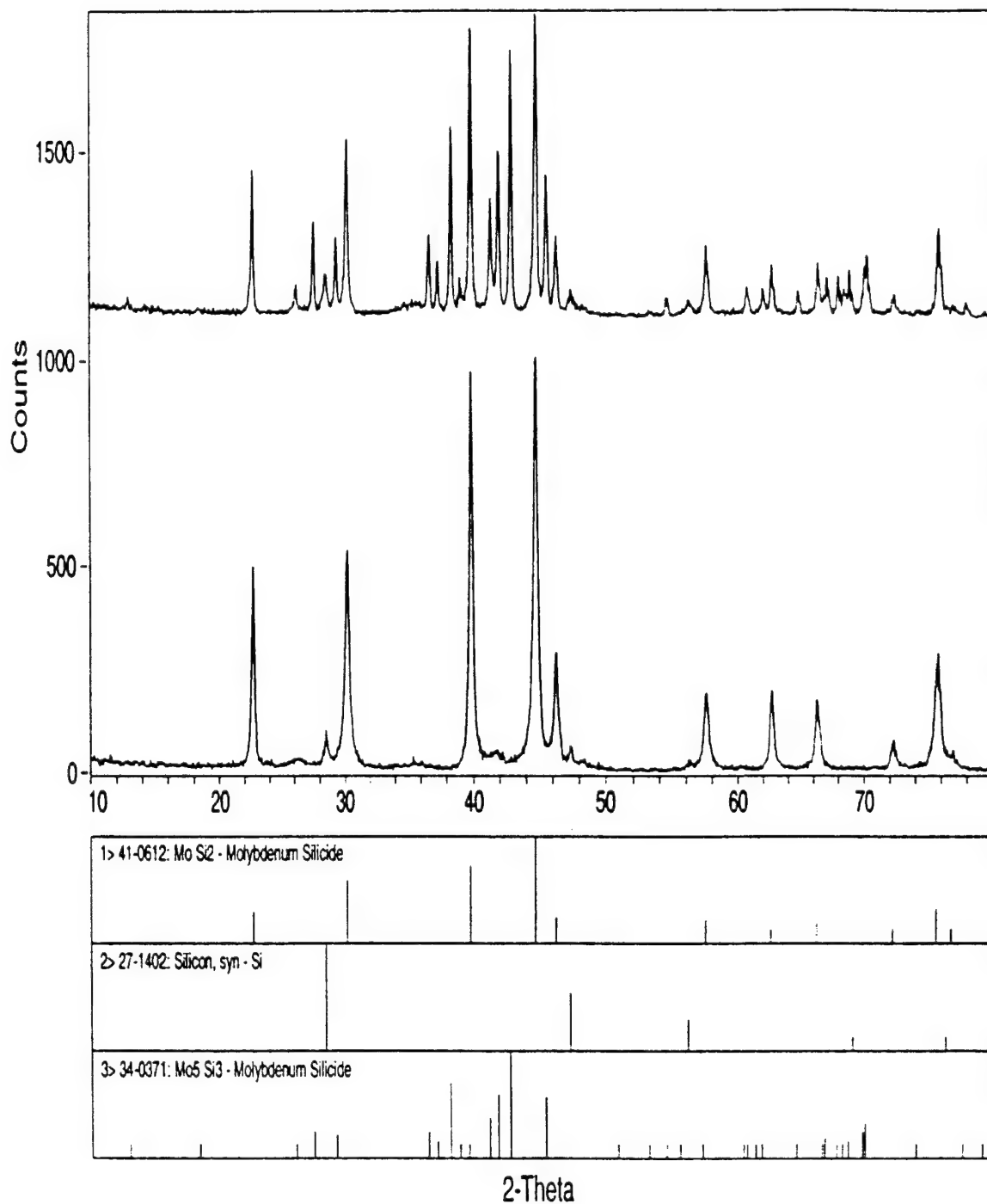


Figure 3.8 XRD patterns illustrating the variability in annealed (900°C, > 30 min) product compositions obtained for reaction using equivalent reactant ratios (3SiCl₄:1MoCl₅).

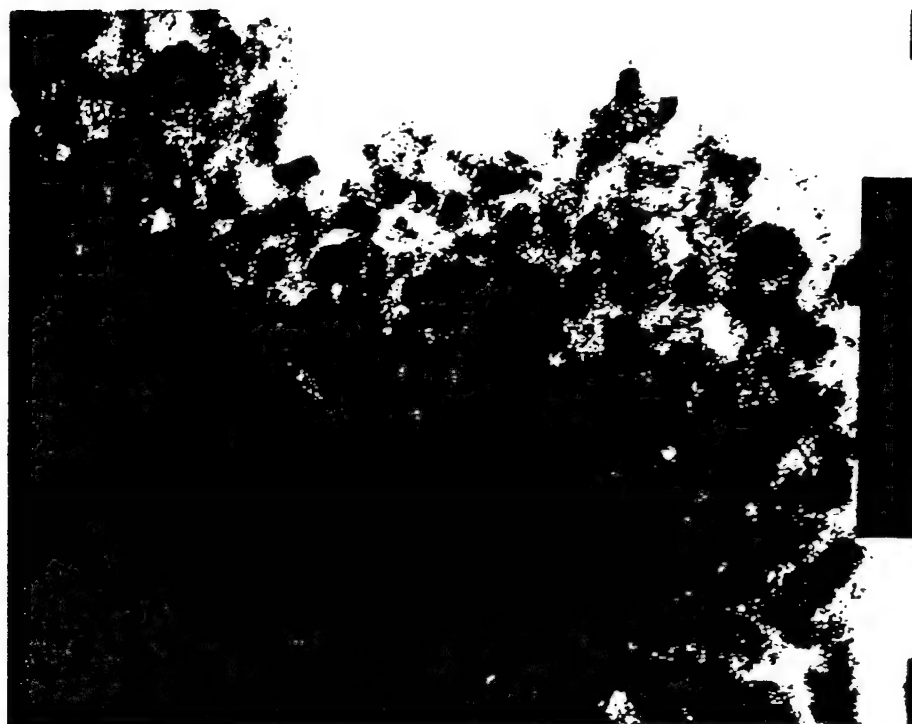


Figure 3.9 TEM images of MoSi_2 obtained by annealing sonochemical reaction products at 900°C for > 30 min. Scale bars are 20 nm (top) and 200 nm.

Samples annealed at 1100°C exhibited a significant amount of sintering (Figure 3.10), which was anticipated considering the grain growth indicated by XRD (Ostwald ripening would not be significant given the low vapor pressure of MoSi₂). The grains were again variable in size, but were typically between 200 and 500 nm. The particles were often somewhat oblong in shape, but faceting was still absent.

Impurity Phases. Though carbide phases essentially disappeared by XRD with annealing at $\geq 900^\circ\text{C}$, copious amounts of carbon were retained in the products according to elemental analysis. Mo:Si:C compositions were found to be 1:2.7-2.9:0.5-1. Note molar ratio of 3:1 SiCl₄:MoCl₅. By the Mo-Si-C phase diagram (Figure 3.11), these compositions fall within one of two three-phase fields, the MoSi₂-Mo₅Si₃-SiC or the MoSi₂-Si-SiC field, or on the two-phase tie-line between MoSi₂ and SiC. This indicates that any carbon that was present should have existed in the form of SiC if the mixtures attained equilibrium. The presence of SiC in the annealed products is supported by the phase evolution that was observed with variable-temperature annealing (Figure 3.7). The diffusion path established (Figure 3.11) for silicon-carbon diffusion into molybdenum passes through Mo₂C and Nowotny as was observed herein. By this path, SiC follows the Nowotny phase, so the formation of SiC upon conversion of Nowotny to MoSi₂ is the logical conclusion.[15].

The lack of SiC reflections in the XRD patterns can be accounted for by the combination of two factors. 1) Because SiC is comprised of considerably lighter elements than the molybdenum compounds, it has fewer electrons to interact with X-rays. This means reflections are much less intense. A demonstration of this has been afforded by the XRD pattern obtained for the annealed products of a solution-based MoSi₂ reaction that was conducted in the presence of sufficient crystalline, SiC whiskers to comprise a 35 volume percent fraction (Figure 3.12). 2) Crystalline coherence lengths may have been very short, leading to broadened reflections with diminished intensities. Short coherence lengths can be explained by the SiC being amorphous owing to the refractory nature of this compound, and also because it may exist as a thin film coating the MoSi₂ particles. A crystalline thin film of SiC less than 4 nm thick coating 50 nm diameter, spherical MoSi₂ particles would be sufficient to comprise 20 volume % of a product. These values are consistent with particle sizes and carbon content established in this research. The thin crystalline films were verified by TEM.

Increasing the ratio of SiC to MoSi₂ obtained by solution-based reactions would increase the likelihood of SiC being observed by XRD. This was accomplished with a reaction conducted with a 6:1 ratio of SiCl₄:MoCl₅. SiC reflections were clearly represented in the XRD pattern of the annealed product (Figure 3.13), but the intensities were weak and the reflections broad, indicating a crystalline coherence length of ~ 7 nm. This product possessed some Mo₅Si₃ reflections because regardless of the Si to Mo ratio, if enough carbon is present, then the composition will reside in the MoSi₂-Mo₅Si₃-SiC field.

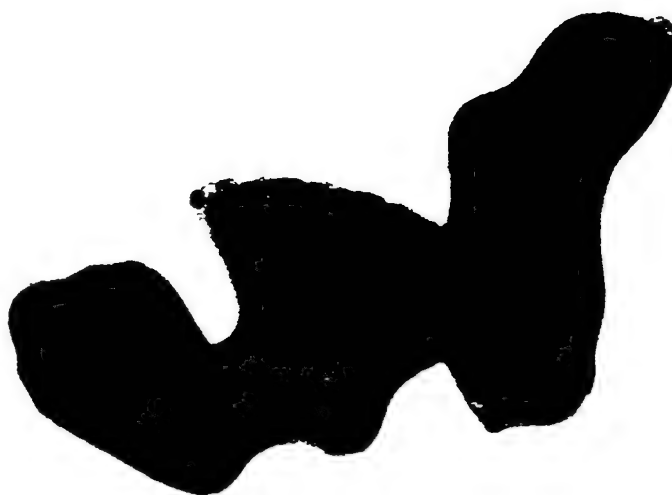


Figure 3.10 TEM images of a sonochemical reaction product annealed at 1100°C for 2h. Scale bars are 200 nm.

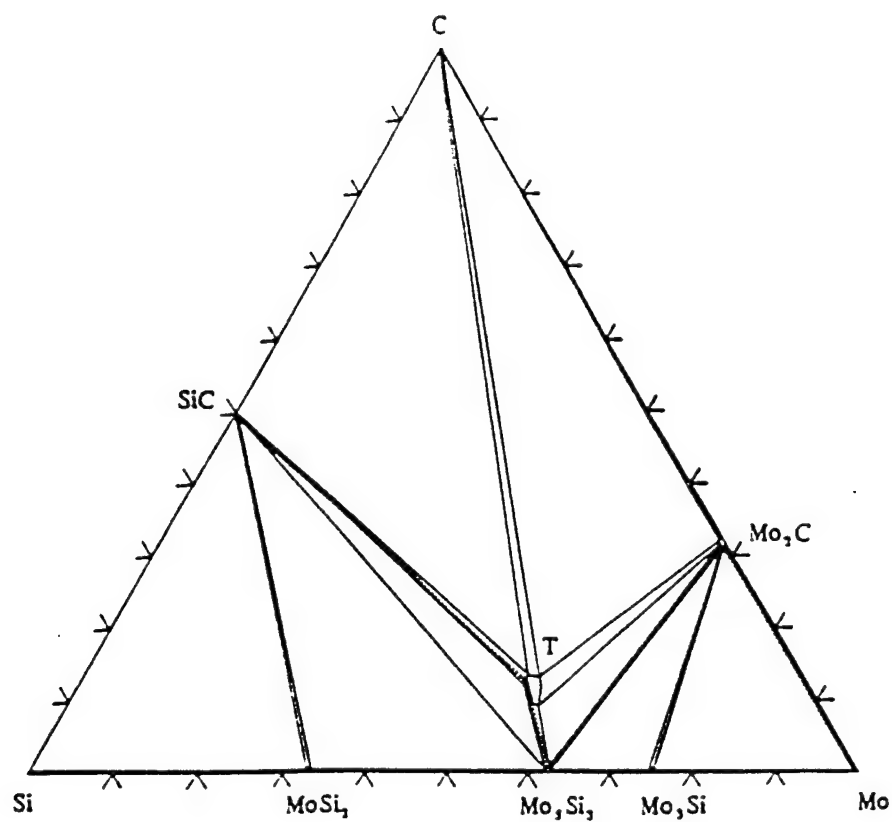


Figure 3.11 The ternary Mo-Si-C phase diagram at 1200°C. $T = \text{Mo}_5\text{Si}_3\text{C}$. The diffusion path for SiC into Mo is provided by the thick lines (Mo- Mo_2C - Mo_5Si_3 -T-SiC).

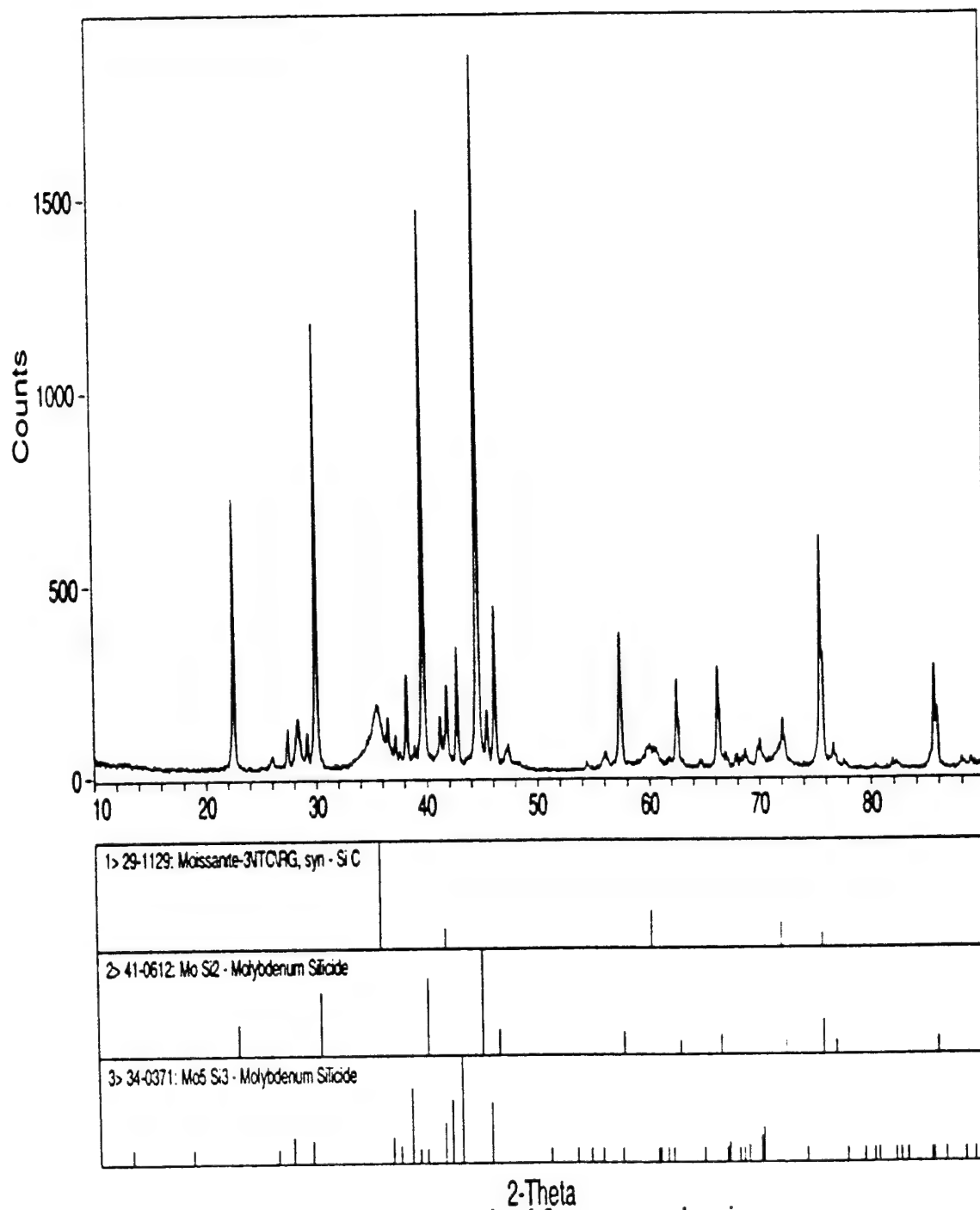


Figure 3.12 XRD pattern of a product derived from a sonochemical reaction using a 6:1 $\text{SiCl}_4\text{:MoCl}_4$ molar ratio (annealed at 1100°C, 1h).

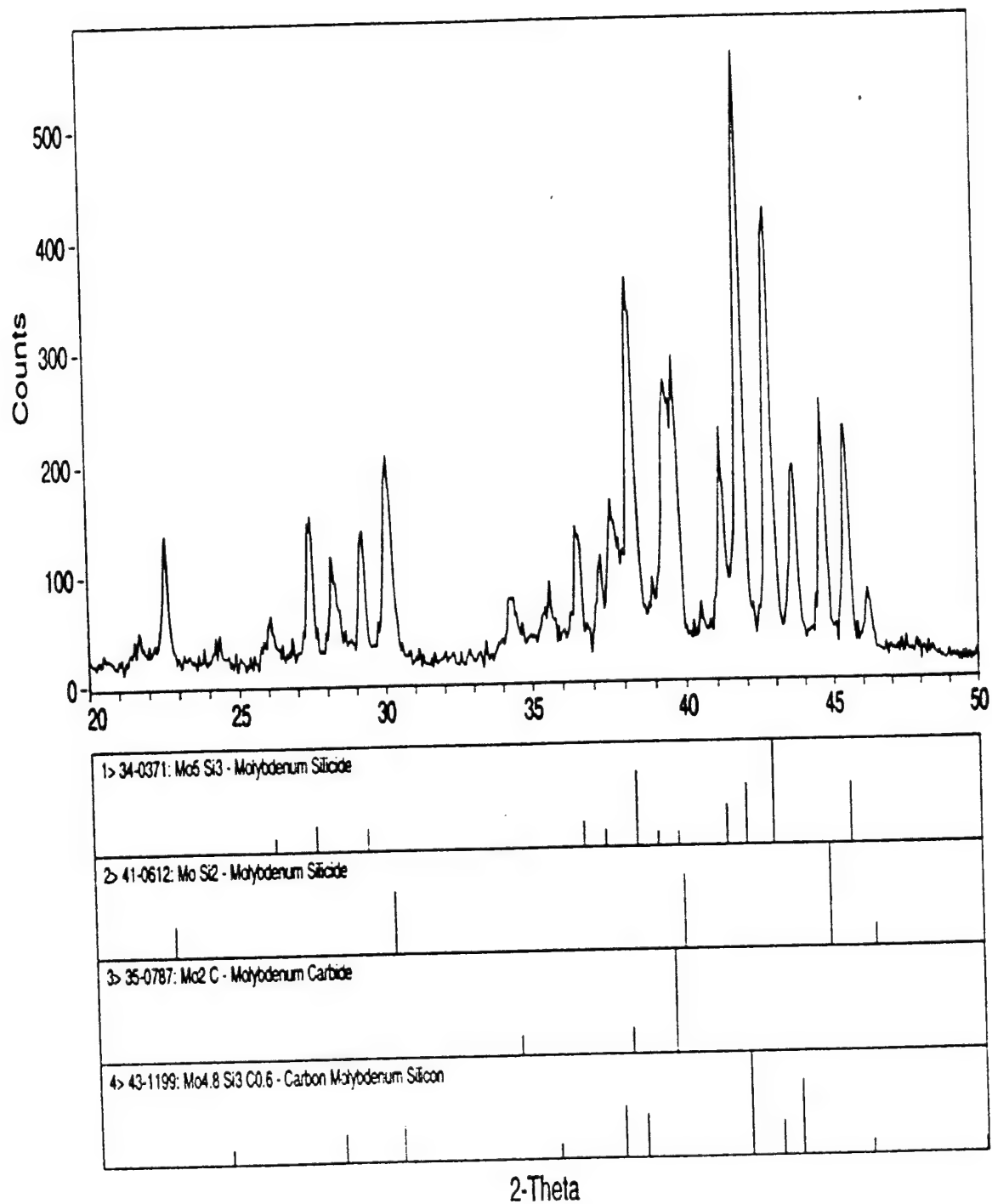


Figure 3.13 XRD pattern of a reaction product obtained by high-speed, high-shear stirring (annealed at 900°C, 20h).

The formation of Mo_5Si_3 in many products can be attributed to carbon scavenging silicon for formation of SiC . However, Mo_5Si_3 was observed even when the Mo-Si-C composition was determined to reside within the MoSi_2 -Si-SiC field rather than the MoSi_2 - Mo_5Si_3 -SiC field. This is attributed to another impurity, oxygen, which also scavenges silicon to form SiO_2 , so in reality the Mo-Si-C-O phase diagram must be considered. Atmospheric contamination while annealing nanocrystalline powders under dynamic vacuum has previously been demonstrated by Crane [16], and this is a likely problem here as well. Oxygen analyses have not been conducted, but the amount of SiO_2 in the products must be much less than SiC considering the mass that was unaccounted for following Mo, Si, C and Cl analyses (Cl was less than 0.5 wt%). Indeed, it would not seem probable that given the rather short annealing times applied that much oxidation could have occurred under a pressure of 10^{-3} torr.

Carbon was prevalent in products because there was an abundant source, the reaction solvent. Hexane was the only available carbon source, as functionalized carbon impurities were scarce because distilled, high-purity solvent was used. It is surmized that oxidative addition of hexane C-H bonds to reduced species in solution resulted in bound alkyls that subsequently decomposed and formed carbides upon thermal processing. Generally, C-H bonds favor reductive elimination over oxidative addition, so the species obtained would have been quite unstable and prone to decomposition, which is believed to account for the low-temperature exothermic process. The noncondensable gas released was likely H_2 formed during this decomposition.

Elimination or control of carbon content in MoSi_2 products will be required for generating practical materials with reproducible mechanical properties, as the carbon influences the phase composition and possibly the MoSi_2 grain sizes. Because no organic solvents are likely to be more inert than hydrocarbons, different solvents would probably lead to at least as much incorporated carbon. Reaction parameters, such as mode and duration of mixing and bulk solution temperature, however, could be influential factors. A reaction was conducted under high-speed mechanical stirring rather than ultrasound to eliminate the cavitation phenomena and ascertain whether this was responsible for solvent degradation that was activating it towards reaction. The stirred reaction was less vigorous than sonochemical reactions because the NaK could not be emulsified as efficiently. Consequently, much SiCl_4 remained unreacted despite mixing for a total of 4 hours (compared to ~ 1 h for sonochemical reactions). The products obtained actually contained a higher proportion of carbon than did the sonochemical reactions according to elemental analysis (Mo:Si:C 1:1.95:0.99), and XRD patterns showed predominately the Nowotny phase (Figure 3.13), so cavitation phenomena may not be the root of the carbon problem. Note the phases were not those dictated by the composition in the phase diagram. This could be due to macroheterogeneities in the precipitated products compared to sonochemical products because of the less efficient mixing afforded by mechanical stirring. The stirred reaction was not cooled by an ice-bath as the sonochemical reactions were, however, so bulk solution temperature could be a key

factor. Changing the reducing agent to CsK alloy, which melts at -48°C , may reduce solvent reactivity by allowing the reactions to be conducted at lower temperatures.

It is possible that the reactivity of the solvent could be averted by modifying the reaction system. It is known that alkali metal reductions produce intermediates that activate hydrogen sources towards the formation of hydrides.[17,18] A solution then, could be to change the reducing agent. This, author, however, is not aware of a suitable alternative. The various hydrides will have a tendency to generate SiH_4 . Furthermore, they are solid powders that will react inefficiently unless dissolved in a coordinating solvent. Such solvents will coordinate molybdenum halides and thereby provide a more severe source of carbon incorporation. Indeed, reductions of molybdenum chlorides in THF have been implemented to neatly generate nanocrystalline Mo_2C [19], and attempts at preparing MoSi_2 in ethereal solvents have generated Nowotny phase in the absence of molybdenum silicides[20]. Note, the phases were incorrectly identified as MoSi_2 , SiC and unidentified reflections in this reference. The difficulties associated with coordinating solvents was observed by this author as well and provided the impetus for concentrating efforts on the heterogeneous reaction of equation 3.1 despite the inability of this system to directly precipitate amorphous MoSi_2 , a shortcoming that has implications on particle size control. Nanoparticles are obtained in the present system by high temperature diffusion processes, which prevents formation of particles at the low end of the nanometer regime.

Simple alternatives to molybdenum and silicon halides as reactants also appear limited. There are few viable inorganic molybdenum or silicon compounds that can be reduced in solution. Organometallic compounds will be prone to carbon incorporation unless efficient elimination pathways for organic substituents can be devised. A search of the literature turned up no satisfactory chemical pathways for depositing molybdenum cleanly.

Other Alkali Metal Reductions. Analogous reactions to those presented herein have been conducted previously by Ritter for other compound ceramics, including SiC , TiC , TiB_2 , and B_4C . Unlike here, those reactions benefited from homogeneity derived from solubility of both reactants, but it was not established in that work whether this afforded direct precipitation of the compounds. It was not even claimed that nanocrystalline products were derived, though it is believed that they were. The results from those reactions were analogous to those obtained here. Reaction completion was difficult to achieve, and after 72 hours of high-speed high-shear stirring, only 90% yields could be affected. Also, for the TiB_2 case, a carbide impurity (TiC) was obtained (It should be noted that this could be a consequence of the reaction temperatures in excess of 100°C .). Finally, a noncondensable gaseous byproduct was evolved on thermal processing of the reaction products under vacuum, though the temperatures ($300\text{--}400^{\circ}\text{C}$) for this were reported to be much higher than was observed herein. These results provide examples of the universal applicability of this reaction strategy, though stoichiometric control and impurity incorporation may be pervasive difficulties.

3.2 Preparation of MoSi₂ by Metallothermic Reactions

The previous section discussed the coreduction of oxidized molybdenum and silicon compounds by a reducing metal. This type of reaction has been widely applied in the absence of a solvent for the preparation of coarse-grained MoSi₂. Examples that have been reported in the literature are provided in Equations 3.2[22,23] and 3.3[23] (Equation 3.2 constitutes the common commercial MoSi₂ preparative method). In light of the difficulties with carbon incorporation in the products and with stoichiometric completion of the reactions discussed in section 3.1, consideration was given to whether nanocrystalline MoSi₂ could be produced by solventless metallothermic reductions. This has not been previously addressed to my knowledge. Preliminary experiments that yielded considerably submicron particles are presented herein that indicate that this should be possible.



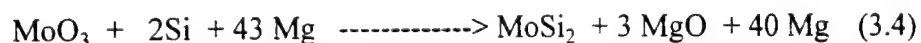
General Procedures. MoO₃ (Mallinckrodt, 99.5%), Mg (Strem, 99%), MoCl₃ (Alfa-Aesar, 99.5%), Si (1-5 μm, Alfa-Aesar, 5N purity) powders were used as received. XRD and TEM analyses were conducted as per section 3.1. All reaction products were treated as air stable.

Preparation of MoSi₂ in a Magnesium Melt. MoO₃ (294 mg, 2.04 mmol), Si (116 mg, 4.12 mmol), and Mg (2.143 g, 88.17 mmol) powders were thoroughly mixed in a mortar under N₂. This mixture was added to a MgO boat and inserted into a quartz tube (note that this is not an ideal procedure, as Mg vapors react with quartz at elevated temperatures), which was evacuated and refilled with argon because Mg will react with nitrogen at elevated temperature. The mixture was heated with a ramp rate of 50°C/min to 1050°C and soaked for 2140 min. Mg (b.p. 1107°C) evaporated over the duration of the experiment leaving behind MgO/MoSi₂ product according to XRD. The yield, however, was high (682 mg, 122.3%), which was attributed to adventitious oxidation of Mg during the reaction.

A reaction of identical scale was also conducted using MoCl₃ (413 mg, 2.04 mmol) instead of MoO₃. Here the mixture was ramped up to 900°C and soaked for 9 h, then cooled, and finally reheated under vacuum to 900°C for 40 min to remove Mg. A yield of 744 mg (133%) was obtained, as oxygen incorporation, most likely from air leakage during evacuation, led to MgO formation.

Metallothermic reductions are highly exothermic and are therefore ignited by localized heating (a wick) and then allowed to self-propagate under internally released heat at temperatures that exceed 2000°C (the thermite process). The large product particles that have been reported can be attributed to the extreme temperatures, as nanocrystallites are thermodynamically metastable and prone to diffusional growth. Note: MoSi₂ melts at the high temperatures which will lead to formation of large particles. Diminishing particle sizes obtained from a metallothermic reaction, then, would require reducing the temperature achieved, which can be accomplished by adding a diluent to absorb heat. With enough diluent, a reaction would not be able to self-propagate through a mixture. Such a mixture would require bulk heating by a furnace, the temperature of which would control the temperature attained by the reaction mixture. Note that localized temperatures at the reactive interfaces will be much higher, but this will be transient as the heat rapidly dissipates to surrounding diluent. In conventional thermite reactions, heat generated by reaction is dissipated to reactants, which leads to release of more heat, or to products, which prevents rapid cool-down. Consequently the products experience elevated temperatures for prolonged times, and diffusional growth processes are allowed, with diffusion distances being shorter than they would be for a diluted mixture.

The initial reaction system investigated (Equation 3.4) was analogous to the magnesiothermic reaction of Equation 3.3, but with elemental Si used rather than SiO₂. Use of Si alloyed with a metal is a common for thermite preparations of silicides and with a large excess of Mg added to serve as the diluent and as a solvent. A compound silicon source was not used because its reduction would just form Si (Reduction of Mo and Si source compounds would proceed independently in this dilute, unstirred system.).



This reaction was expected to proceed by the following mechanism. When the melting point of Mg (649°C) was reached, a rapid reduction of MoO₃ would occur. Mo has negligible solubility in Mg[24], so high supersaturation would be achieved, resulting in a rapid and large scale nucleation event that would give rise to small Mo nanoparticles (the LaMer model[25]). Si would alloy with the Mg once it melted (See the phase diagram, Figure 3.14), which would accelerate mass transport of Si to the Mo particles, enabling reaction to form MoSi₂. The Mo particle sizes would essentially dictate the MoSi₂ particle sizes obtained provided that little sintering occurred in the melt. Because MoSi₂ and Mo have negligible solubility in Mg, little growth arising from enhanced solubility of the smaller particles would be anticipated. This last fact provided a key motivation for using Mg as the reducing metal and solvent. The other common reducing metals for metallothermic reductions, Al and Zn, will alloy with Mo and therefore possibly lead to larger particles.

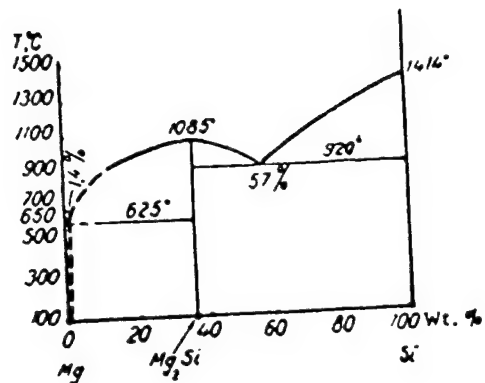


Figure 3.14. The Mg-Si binary phase diagram.

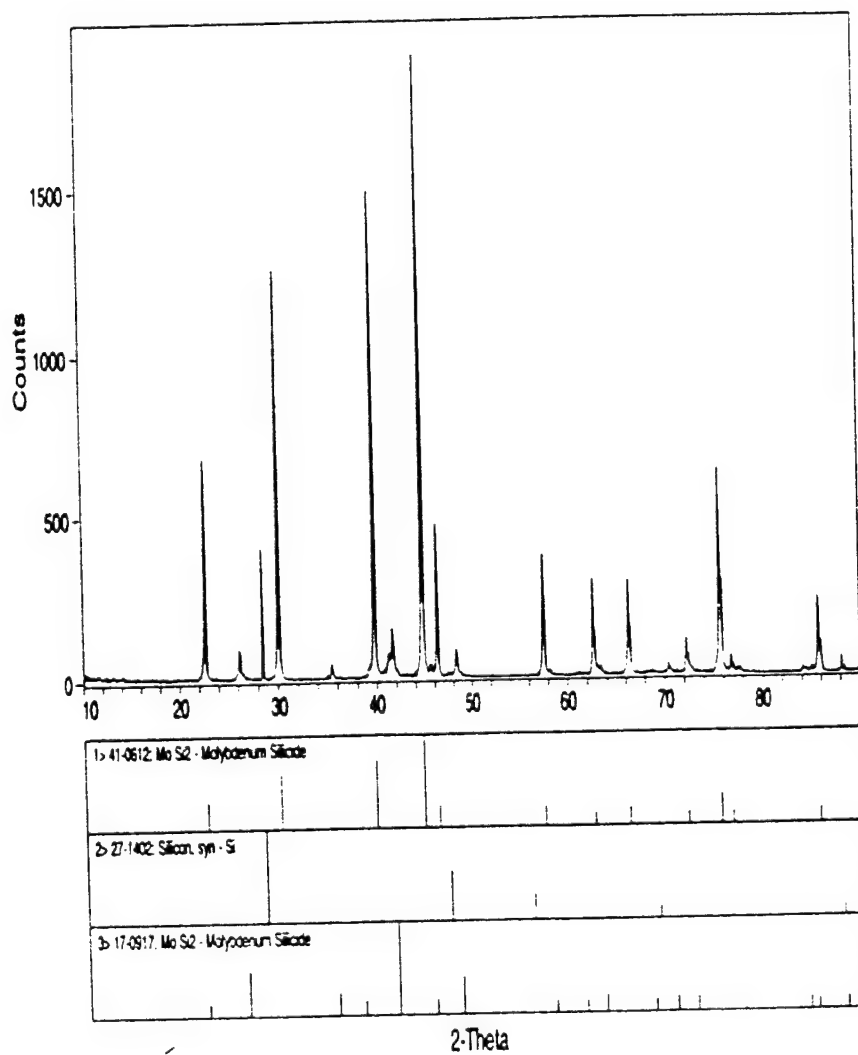
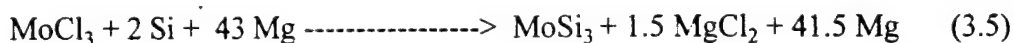


Figure 3.15 XRD pattern of the product obtained from the magnesiothermic reduction of MoO₃ in the presence of Si at 1050°C for 36h.

A mixture of MgO_3 , Si and Mg was heated at 1050°C for ~ 36 hours. The Magnesium (b.p. 1107°C) evaporated during this period leaving behind the products. Analysis of the products showed that MoSi_2 crystallites were obtained that were by in large smaller than what has been reported for metallothermic reaction products. XRD line broadening indicated an average particle size of 99 nm (Figure 3.15). Measured sizes from transmission electron micrographs (Figures 3.16 and 3.17) were inconsistent, as the bulk of the crystallites were in the 100-200 nm range. The distribution of sizes, however, was wide. Many particles were indeed in the nanometer regime (down to 20 nm), but a few exceeded $1\text{ }\mu\text{m}$ (up to $5\text{ }\mu\text{m}$). With the exception of some of the large particles, most of the particles were unsintered, roughly spherical, and embedded in magnesium oxide byproducts. Considering that Mg evaporated over the course of this reaction, the MgO byproducts were probably important for minimizing direct MoSi_2 particle contacts and inhibiting sintering. Sintering of particles that were not adequately protected by oxides probably accounts for the large particles observed. An analogous reaction was also performed using MoCl_3 rather than MoO_3 (Equation 3.5). To our knowledge, halides have not been used in thermite preparations of MoSi_2 ;



The motivation for changing reactants was to obtain a more easily removed byproduct (The oxide was used initially merely because oxides are the standard thermite reactants.). The oxide generates MgO which is undesirable as a reinforcement phase because of its poor mechanical properties and can not be removed by sublimation since it has a high melting point (2852°C). MgO, therefore, has been removed by washing with strong acids. This would likely introduce surface oxides to the products, which would not be desired because grain boundary SiO_2 leads to problematic creep in MoSi_2 . Mg reacts vigorously with acids and would have to be sublimed before washing, making isolation of products a 2 step procedure. With MoCl_3 , however, MgCl_2 is formed which can be removed easily *in vacuo* at just above its melting point of 714°C , at which temperature Mg can also be sublimed (It can also be washed away with alcohol.).

The $\text{MoCl}_3/\text{Si}/\text{Mg}$ mixture was annealed at lower temperature (900°C) for a shorter time ($\sim 10\text{ h}$) than was the oxide mixture. MoSi_2 was obtained, and by XRD, a slightly shorter average crystallite coherence length of $x\text{ nm}$ was calculated (Figure 3.18). As for the oxides, however, the bulk of the particles observed in TEM images were greater than 100 nm. Unlike for the oxide products, they were highly sintered. Figure 3.19 shows a sintered agglomerate possessing particles ranging from 50 to 500 nm, which was typical for the sample. The sintered agglomerates are attributed to the lack of MgO byproduct formation during this reaction. MgCl_2 is molten at the temperature of the reaction mixture and therefore probably does not inhibit sintering. MgO was observed in the XRD pattern of this product, but this is believed to have been due to adventitious oxidation of Mg at the surface of the melt and not in the vicinity of the MoSi_2 being formed.

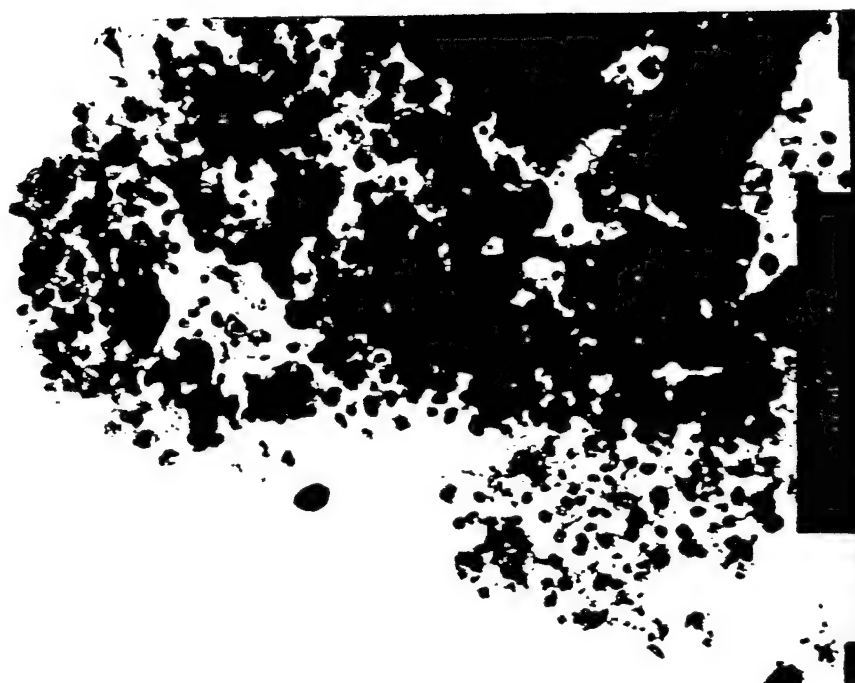


Figure 3.16 TEM images of the product of equation 3.4 showing MoSi₂ crystallites (dark particles) dispersed in MgO (light contrast). Most of the MoSi₂ is present as 100-300 nm spheres (top), but smaller particles (bottom) are common too.

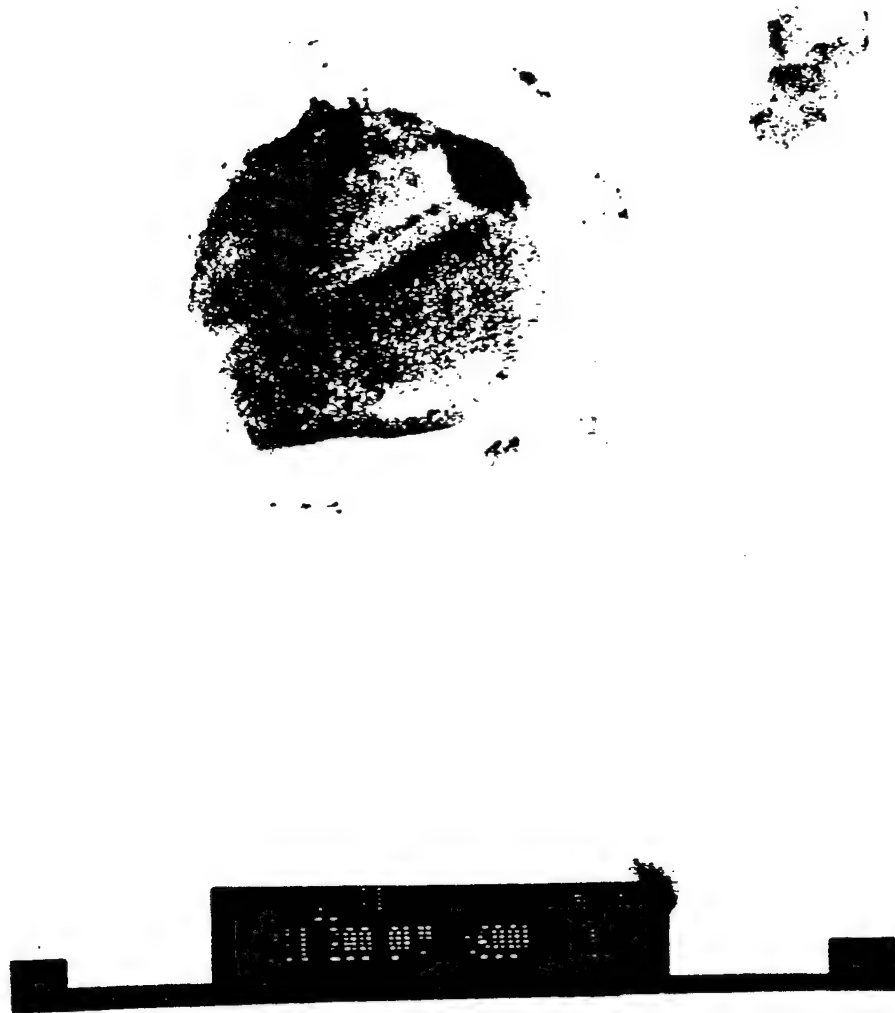


Figure 3.17 TEM image showing an MoSi₂ particle that appears to be encased in the MgO. Such coatings could be controlling particle size and inhibiting sintering.

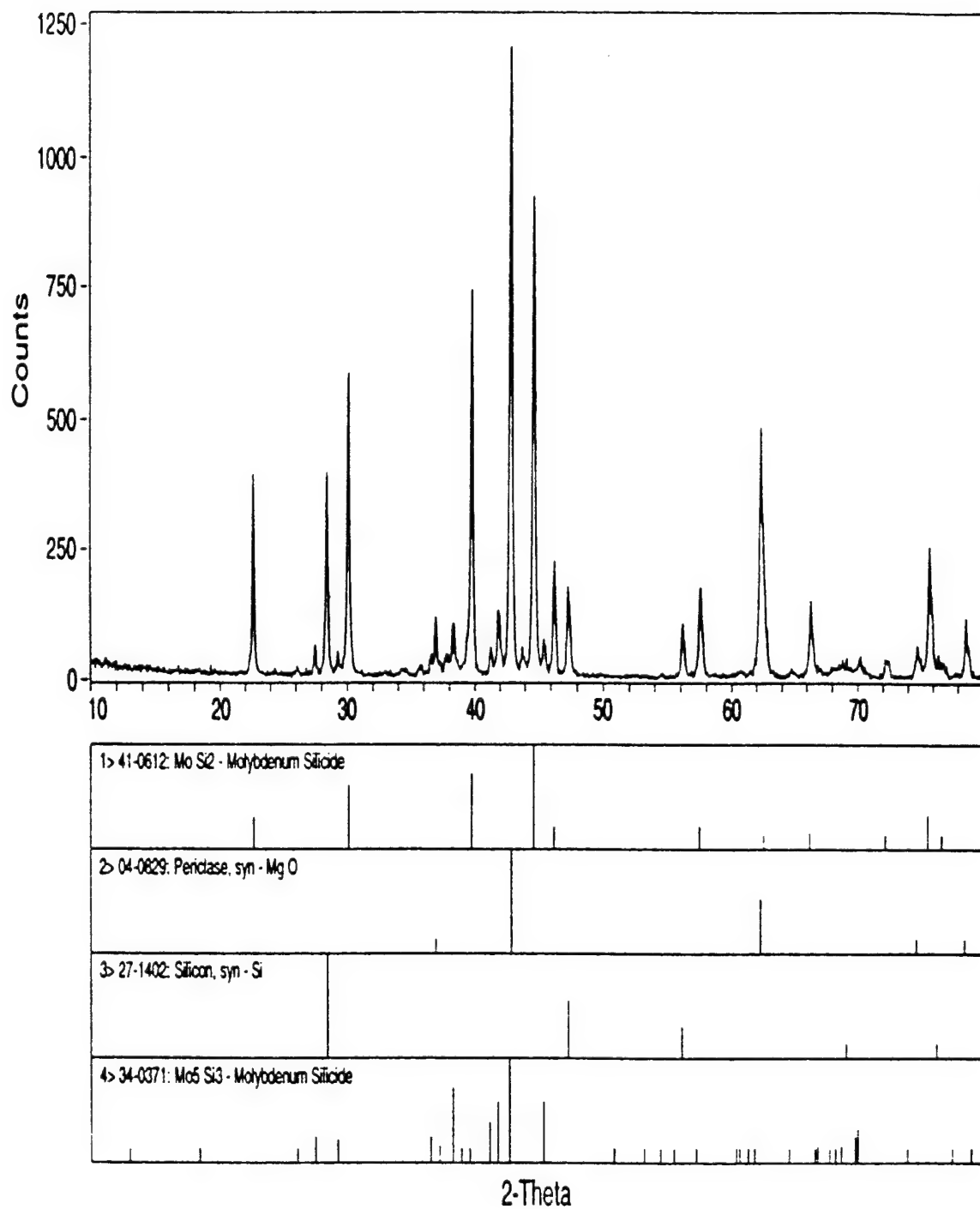


Figure 3.18 XRD pattern of the product obtained from the magnesiothermic reduction of MoCl_3 in the presence of Si at 900°C for 10 h.



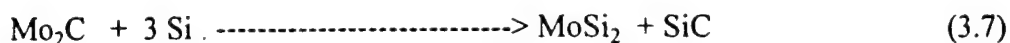
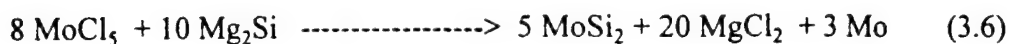
Figure 3.19 TEM image showing sintered MoSi₂ particles obtained from the magnesothermal reductions of MoCl₃ in the presence of Si.

Substantial Si reflections were present in the XRD pattern of this product. Unlike for the solution-based reactions, then, the diffusion reaction of Mo and Si was not completed rapidly at 900°C. This may be a consequence of slow dissolution of Si into Mg. It would perhaps have been better to use a compound silicon source that would have been reduced to form ultrafine particles that could be rapidly dissolved. Alternatively, it may be possible to pre-alloy Mg and Si. Implementing such strategies would make the reactions more similar to the solution-based reactions, and smaller particles similar to those products may consequently be obtained. However, it may be found that the carbonaceous impurities derived from the solvent were critical to the success of those reactions.

The reactions described above did not generate nanocrystalline MoSi₂, but these were only preliminary experiments, and it is believed that this should be possible with further optimization. There are two basic reasons that could explain why the products obtained herein were not within the nanometer regime. First is that these reactions lacked carbonaceous impurities to inhibit grain growth. This may be a factor, but the next chapter will describe a reaction mixture that did not contain any significant growth inhibitors but yet yielded nanocrystalline MoSi₂ by Mo and Si interdiffusion at 900°C. The more likely reason, then, is that these reactions did not generate an intimate mixture of Mo and Si initially. Mo particles may have grown substantially before silicon alloyed with magnesium so that molybdenum-silicon interdiffusion could proceed to convert the product to MoSi₂. (Note: this has not been established, but could be by quenching a reaction rapidly and evaluating the size of Mo particles obtained.) Adding the molybdenum source compound slowly to a vigorously stirred Mg/Si alloy may result in rapid formation of MoSi₂ with little growth, or possibly even direct nucleation of MoSi₂. These conditions would more nearly approximate those of the solution-based reaction, but without the organic solvent. Further, this strategy would minimize the quantity of reducing metal required to dissipate the heat of the reduction.

3.3 Solid-State Route to MoSi₂

The preparative chemistry of MoSi₂ is rather limited. Primarily, bulk MoSi₂ has been prepared by the metallothermic reductions that were discussed in the previous sections, or by direct reaction of the elements, which has been accomplished by innumerable methods [27]. Very few alternative reactions have appeared in the literature. Among those that have are a solid-state metathesis reaction (Equation 3.6)[28] and the displacement of carbon (or oxygen) in the solid-state from molybdenum to silicon (Equation 3.7)[29]. All of these methods have disadvantages in requiring high energy inputs, resulting in large grains, and/or yielding byproducts that are inconvenient to remove. This section presents a solid-state reaction analogous to that of Equation 3.7, but with chlorine as the displaced element (Equation 3.8). This reaction has a low activation barrier, generates a volatile byproduct, and is capable of generating ultrafine particles.



General Procedures. All reactions were conducted in a Lindbergh Blue M tube furnace under argon. Reaction mixtures were prepared and products collected under N_2 . MoCl_3 (Alfa-Aesar, 99.5%), Si (1-5 μm , Alfa-Aesar, 5N), LiCl (Aldrich, 99%), and ZnCl_2 (Aldrich, 98%) powders were used as received. XRD and TEM analyses were conducted as in Section 3.1. All reaction products were treated as air stable for these analyses unless otherwise noted.

Preparation of MoSi_2 by Solid-State Reaction of MoCl_3 and Si. This reaction was conducted on several scales and the procedure reported here is for 8 g of MoSi_2 (theoretical yield). MoCl_3 (10.760 g, 53.189 mmol) and Si (4.111 g, 146.4 mmol) were thoroughly mixed in a mortar until the powder was homogeneous in appearance. This mixture was added to a quartz tube which possessed a reaction zone (1" diameter) and a byproduct collection zone (1") separated by a constricted zone (1/4", 3 cm long). The tube was inserted into a furnace with the constriction situated at the opening (Figure 3.20). The mixture was heated under argon with a ramp rate of $20^\circ\text{C}/\text{min}$ to 500°C . A soak time of 5 minutes was adequate for completing the reaction. The reaction tube was allowed to cool, and then a colorless byproduct liquid that condensed in the collection zone of the tube was stripped *in vacuo*. 7.589 g (94.8% yield) of a dark gray product that analyzed as $\alpha\text{-MoSi}_2$ by XRD was collected.

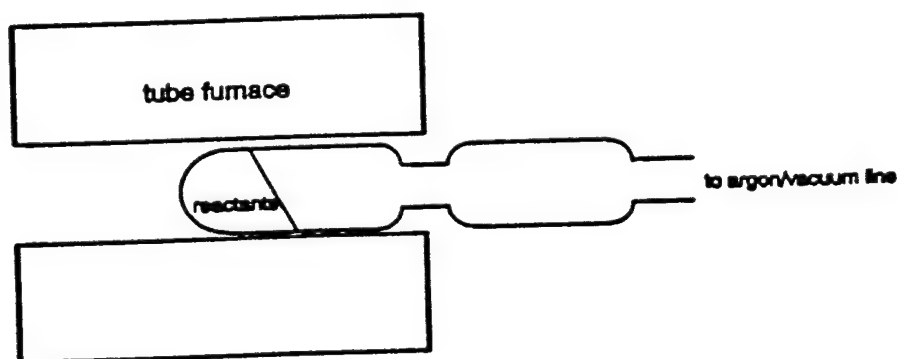


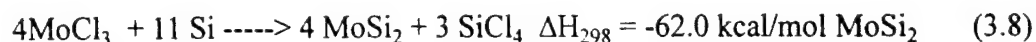
Figure 3.20 Diagram of the solid state reaction tube. The constriction minimizes blow out of the reactants and products.

Preparation of MoSi_2 by Solid-State Reaction of MoCl_3 and Si with Added Diluent. These reactions were analogous to that mentioned above, but with an inert salt mixed in with the reactants. Generally the diluent was LiCl, but ZnCl_2 was also used. The diluent/ MoCl_3 molar ratio was varied from 0.5 to 10. The typical reaction was conducted with 3.273 g (16.18 mmol) MoCl_3 and 1.248 g (44.44 mmol) Si. Diluent was removed

after reaction by annealing under dynamic vacuum (10^{-3} torr) at 500°C (ZnCl_2) or 750-900°C (LiCl), or by washing with MeOH .

Preparation of Mo by Solid-State Reaction of MoCl_3 and Si. MoCl_3 (g, mmol) and Si (g, mmol) were mixed, reacted and worked-up by the same procedure as described above for MoSi_2 . The mixture was soaked at 500°C for 12 h. Nano-Mo was obtained according to XRD, but MoCl_2 and other impurities were also present.

Preparation of MoSi_2 by Cl Displacement. MoSi_2 was prepared by heating mixtures of MoCl_3 and Si (Equation 3.8). The first indications of reaction were noted at



temperatures as low as $\sim 400^\circ\text{C}$. Some small, yellow crystals began to grow in the quartz tube just outside the furnace. X-ray diffraction on such crystals gave a pattern with several unidentifiable reflections, but MoCl_2 , which is a yellow solid,^x appeared to be a constituent phase. MoCl_2 is not a volatile species at these temperatures, so a vapor phase transport mechanism may have been operating, perhaps with byproduct SiCl_4 being the carrier.

Moments after a furnace temperature of 500°C was reached, a vigorous reaction was initiated that proceeded to completion within a few seconds with the liberation of much heat (The furnace thermocouple, which was not in contact with the tube, registered a temperature elevation of $\sim 50^\circ\text{C}$.) A large quantity of volatile byproduct was expelled during this process (along with some gray powder) and condensed as a colorless liquid in the tube outside the furnace. This liquid was identified as SiCl_4 by ^{29}Si . A dark gray powder was left in the reaction zone after the reaction, which consisted of primarily α - MoSi_2 possessing an average crystallite size exceeding 100 nm according to XRD (Figure 3.21). TEM showed that the dimensions for most of the particles fell only slightly outside the nanometer regime in the 100-200 nm range. Most of these particles exhibited some degree of sintering with other particles (Figure 3.22). EDS indicated that Cl elimination as SiCl_4 was essentially complete, as well less than 1 atom percent of Cl was detected in the product.

It has not been established how hot the reaction mixture became during the exothermic reaction, but given that a thermocouple not in direct contact with the reaction mixture registered a dramatic temperature elevation, and considering that the total heat of this highly exothermic reaction was released in seconds, the ultimate temperature must have been quite high. As for the metallothermic reactions, then, it was reasoned that smaller particles within the nanometer regime could be obtained if the reaction were moderated with a diluent. For practical applications, this diluent could be a desired reinforcement phase, such as SiC . The goal here, however, was to generate monolithic nano MoSi_2 for mechanical properties testing. Therefore, LiCl , which can be readily sublimed at about 750°C or washed away with methanol, was initially used.

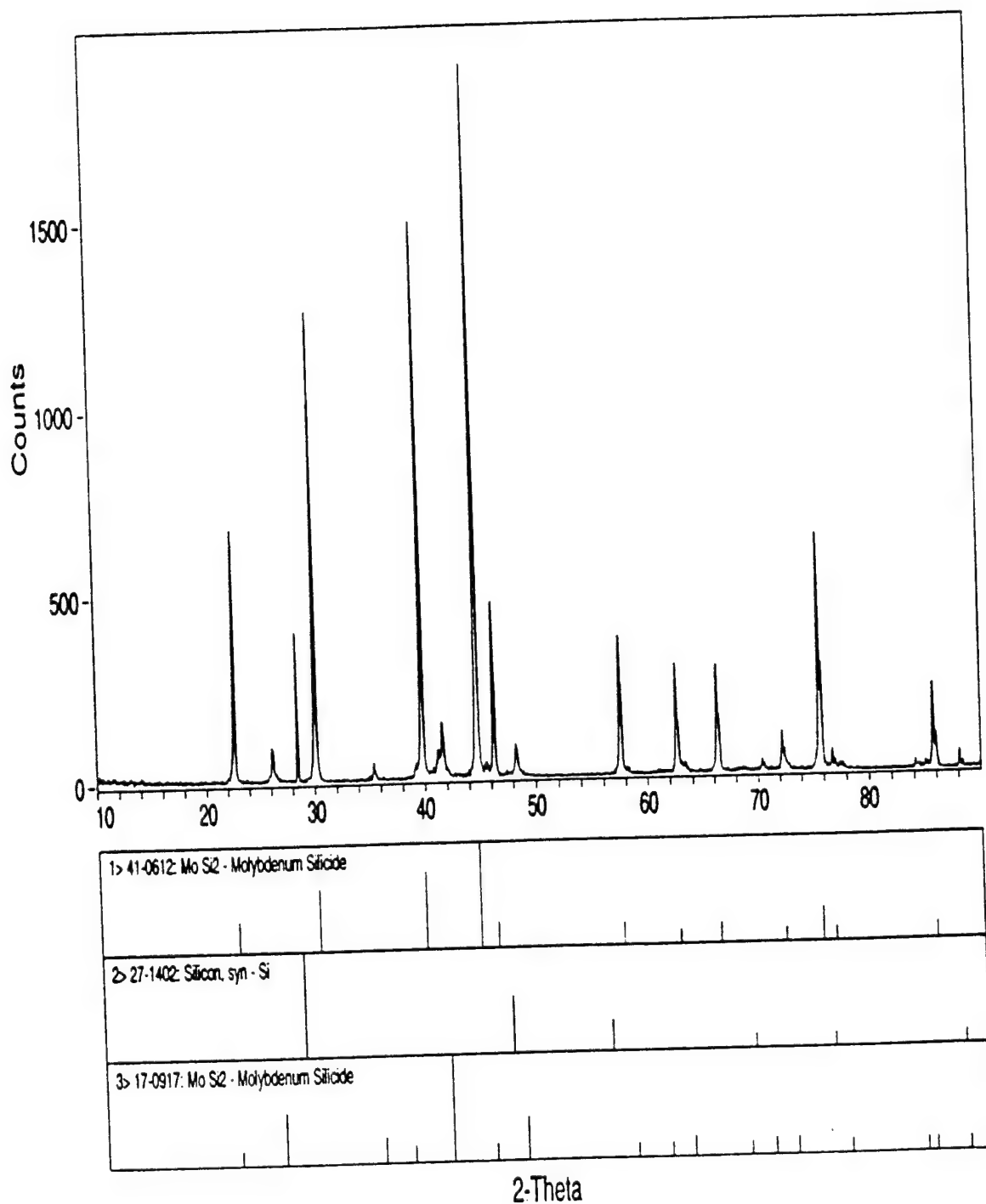


Figure 3.21 XRD pattern for the solid product obtained from equation 3.8. The coherence length is greater than 100 nm.



Figure 3.22 TEM image of the product obtained from equation 3.8 showing sintered MoSi_2 particles. The scale bar is 100 nm. The product appears to border upon the nanometer regime, as many particles are less than 100 nm in diameter.

A series of reactions was conducted on the same scale (2.5 g MoSi_2 theoretical) with an increasing amount of LiCl diluent. Figure 3.23 shows the XRD patterns derived from products of these reactions. As the $\text{LiCl}/\text{MoCl}_3$ molar ratio was increased from 0 to 10, the intensity of the reactions diminished, as was evidenced by the slowed evolution of SiCl_4 from the reaction zone. For ratios of ≥ 2.5 , a few minutes were required for complete elimination of SiCl_4 (according to visible inspection) and no temperature elevation was registered by the furnace thermocouple. MoSi_2 crystallite sizes became smaller according to XRD line broadening as the reaction intensity diminished. However, the reactions also became increasingly less complete. Products with much LiCl contained unreacted Si and a mixture of lower silicides (Reflections did not always neatly match known silicide phases) despite application of extended soak times at 500°C (up to 36 h).

These reactions with much diluent were incomplete in terms of MoSi_2 formation, but not with respect to chlorine displacement from molybdenum to silicon. EDS analysis on a product derived from a ratio of 2.5 showed only about 0.2 atom percent of chlorine, indicating that almost all of the chlorine had escaped as volatile byproducts. Further, weight yields were consistent with the complete elimination of SiCl_4 (~98% yields), and chloride phases were not evident by XRD (except when a highly diluted reaction was quenched after only 2 minutes.). These results are consistent with the visual observations that indicated SiCl_4 elimination was completed within just a few minutes.

For products that were derived from reactions with a large amount of diluent, formation of MoSi_2 could be completed during sublimation of LiCl . The MoSi_2 particles thus obtained were nanocrystalline, despite the very large dimensions of the silicon particles in the products prior to annealing. Figure 3.24 shows the XRD pattern for a sample ($\text{LiCl}/\text{MoCl}_3 = 2.5$) heated under vacuum for 12 h at 900°C . The average grain size was calculated as 54 nm, and TEM images appeared relatively consistent with this (Figure 3.25). A few crystallites reached as large as 200 nm, but these were uncommon, while the smallest particles around 20 nm were relatively abundant. Appreciable sintering was observed in this sample, including some dense, spherical, aggregates that occasionally exceeded 1 μm (Figure 3.26). These spheres may have formed to minimize surface contact with molten LiCl . The particles were nanocrystalline presumably because the reaction of MoCl_3 and Si generated nanocrystalline Mo particles. Because Si diffuses into Mo much more rapidly than the reverse [30], Mo particle size should dictate the grain sizes initially..

ZnCl_2 was also used as a diluent because it can be rapidly sublimed at 500°C , and it is highly soluble in methanol or ether, making it easier to remove than LiCl . Very different results, however, were obtained. With a $\text{ZnCl}_2/\text{MoCl}_3$ ratio of only 0.625, there was no abrupt exothermic ignition, and the reaction actually proceeded much more slowly than the highest $\text{LiCl}/\text{MoCl}_3$ ratios studied. This was evidenced by the retention of the red color of MoCl_3 after 20 min and the very slow evolution of SiCl_4 (It would not condense because it accumulated more slowly than the rate of evaporation and escape with the argon effluent). Therefore, the mixture was soaked at 500°C for 14 h (including

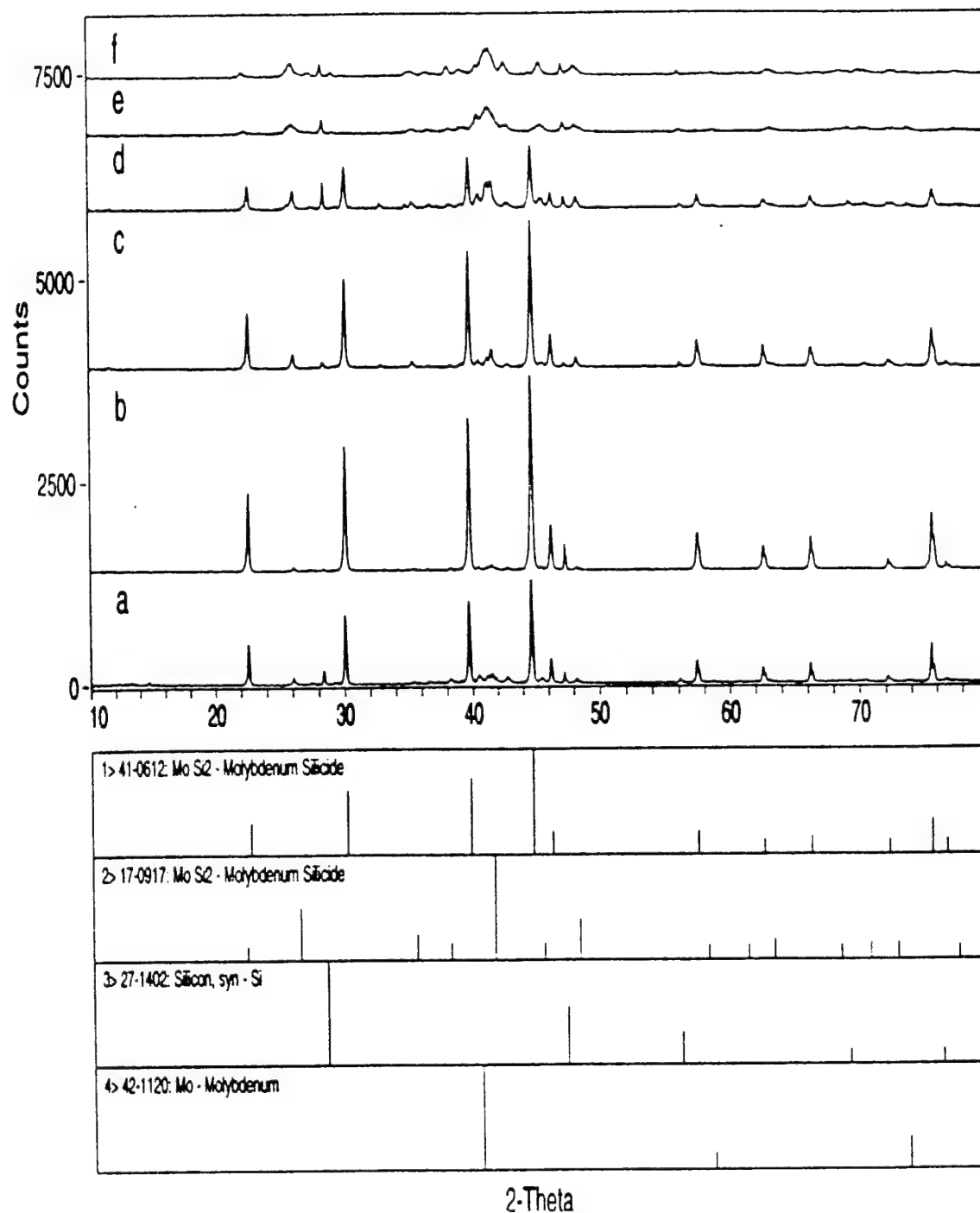


Figure 3.23 . XRD Patterns of products obtained from equation 3.8 conducted in the presence of varying amounts of LiCl. $\text{LiCl}_3:\text{MoCl}_3$ ratios, annealing times at 500°C .

(a) 0:1, 2 min, $\alpha\text{-MoSi}_2$ (> 100 nm); (b) 0.5:1, 2 min, $\alpha\text{-MoSi}_2$ (~ 100 nm); (c) 1:1, 2 min, $\alpha\text{-MoSi}_2$ (90 nm); (d) 1.5:1, 1 h, $\alpha\text{-MoSi}_2$ (75 nm); (e) 2.5:1, 36 h, $\beta\text{-MoSi}_2$ (< 10 nm); (f) 10:1, 24 h, $\beta\text{-MoSi}_2$ (< 10 nm). All rxns. were on a 2.5 g scale.

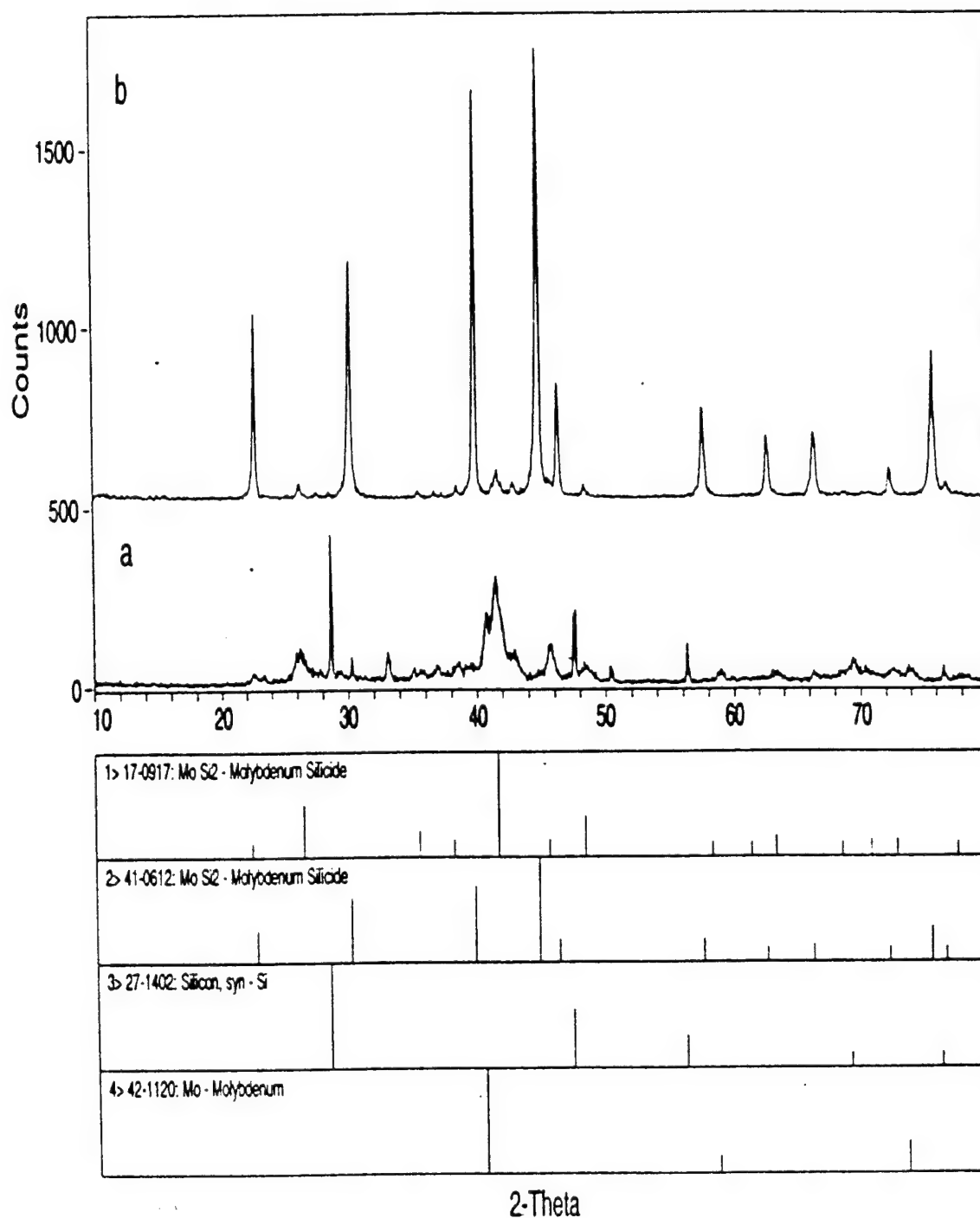


Figure 3.24. XRD patterns for the product of equation 3.8 conducted with a 2.5:1 LiCl:MoCl₃ molar ratio.

(a) heated to 500°C for 1 h; (b) subsequently heated to 900°C for 12 h. The primary phase in b is α -MoSi₂ (54 nm).

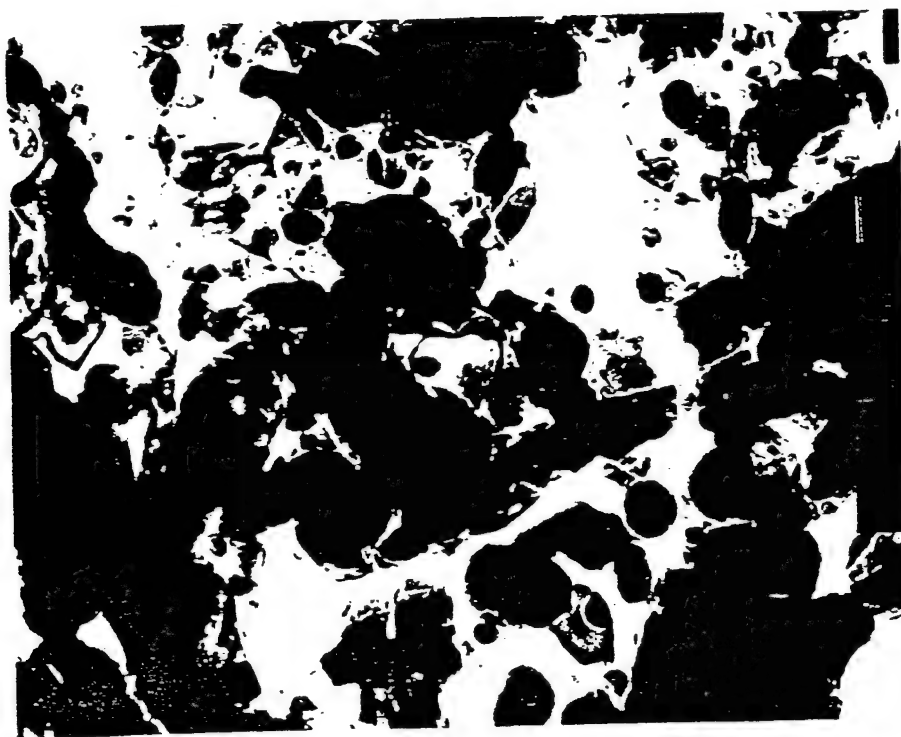
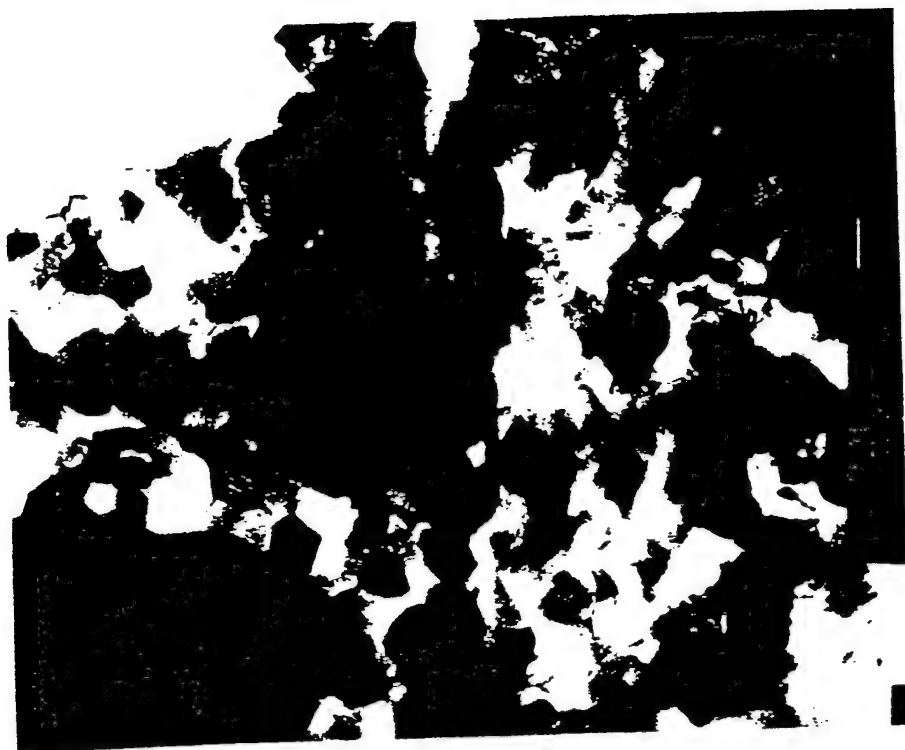


Figure 3.25. TEM images showing highly sintered (top) and loose (bottom) MoSi₂ crystallites. Scale bars are 50 nm.

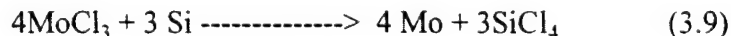


Figure 3.26. TEM images of product in Figure 3.24 showing a combination of dense spherical agglomerates, and less dense, irregular agglomerates (top), and focusing in on a spherical agglomerate, which appears to be comprised of nanocrystallites (bottom). The scale bar on top is 2 micrometers and on bottom is 50 nm.

4h under vacuum to remove ZnCl_2) to ensure complete elimination of Cl, though it was probably complete when the powder had finally turned gray in about 1 hour. The ultimate product was collected in a 94% yield based on theoretical MoSi_2 mass, indicating that most of the chlorine was eliminated as SiCl_4 . Further, XRD showed no evidence of chloride phases. But it did indicate that the reaction was more incomplete with respect to MoSi_2 formation than any of the LiCl reactions, as Si and Mo peaks were much more predominant with respect to $\beta\text{-MoSi}_2$ (Figure 3.27a). As for the LiCl reaction products, however, these products could be converted to MoSi_2 with further annealing. Figure 3.27c shows the XRD obtained for a product annealed for 12 h at 900°C for which the average particle size was determined to be 53 nm.

These results indicate that the solid-state reaction discussed herein can be moderated with a minimal quantity of diluent with proper diluent selection. $\text{ZnCl}_2/\text{MoCl}_3$ ratios far below 0.5 may accomplish the same result as a $\text{LiCl}/\text{MoCl}_3$ ratio of 2.5. The explanation postulated for the improved efficiency of the ZnCl_2 diluent is that, unlike LiCl, it is molten (m.p. = 283°C) at the temperature that the solid-state reaction initiates. It may thereby wet and passivate the MoCl_3 reactant particles, hence resulting in a dramatic drop-off in the reaction rate and the consequent maximum reaction temperature.

Preparation of Mo. Cl displacement from Mo to Si has also been performed in the absence of excess Si to establish whether nanocrystalline Mo could be obtained (Equation 3.9). The reaction was conducted identically to the MoSi_2 reactions.



The reaction was vigorous, but it was not as rapid or as intense as for MoSi_2 reactions using the same molar quantity of MoCl_3 . This was a consequence of the exothermic heat due to MoSi_2 formation not being released in this reaction. The gray product exhibited a yellow tinge, which is indicative of MoCl_2 , even after 12 hours of soaking the mixture at 500°C . The Cl elimination, then, appeared incomplete, unlike for any of the MoSi_2 reactions. This was verified by XRD, as MoCl_2 was identified along with the desired nanocrystalline Mo (Figure 3.28). Some poorly crystallized molybdenum silicides and a significant amorphous band in the region where most of the intense molybdenum silicide reflections appear ($30\text{-}50^\circ 2\theta$) were also present. EDS established that the product contained approximately 10% Si. It is believed that some of the Si was probably scavenged by Mo to form amorphous silicides, hence leaving a deficiency of Si for formation of SiCl_4 . The stability of the Mo-Si bonds would have rendered that Si energetically unfavored for reaction with MoCl_2 , so the reaction consequently could not go to completion. Possibly, addition of diluent to the reaction to diminish the vigor of the reaction would minimize Si diffusion into Mo and allow the reaction to proceed to completion. However, inadequate mass transport under mild conditions in the absence of excess silicon may prohibit completion of the reactions in a reasonable time.

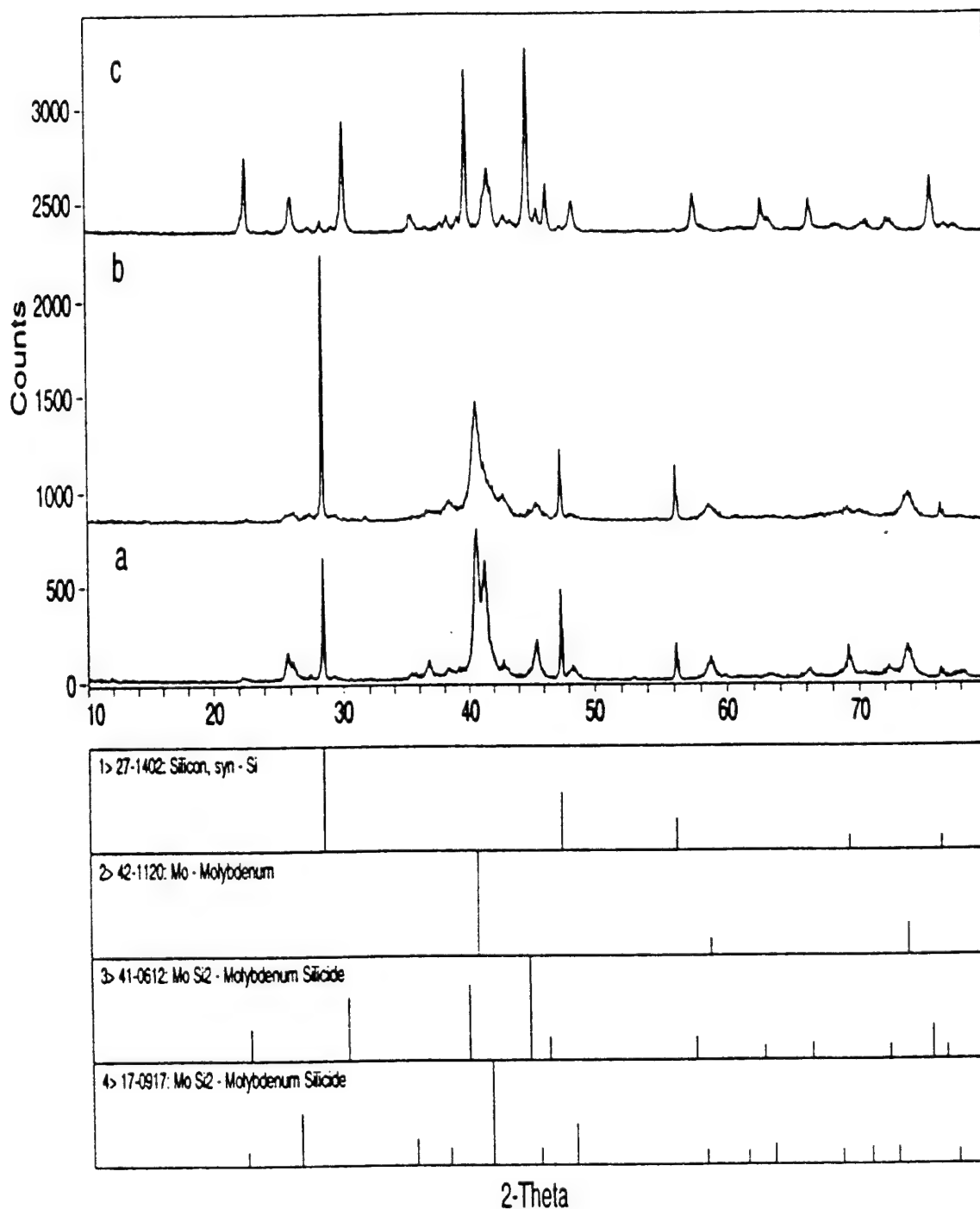
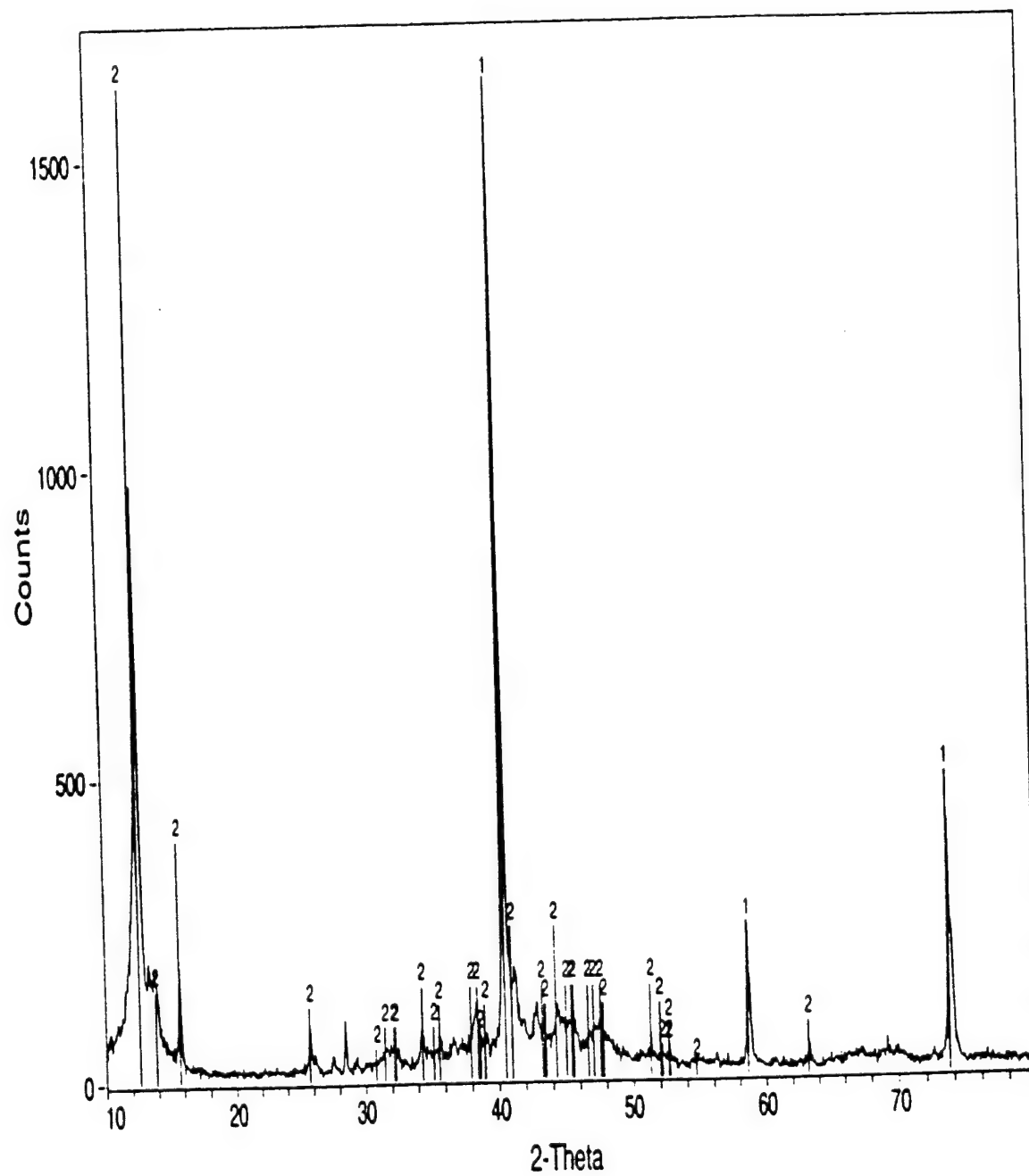


Figure 3.27. XRD patterns for the products of equation 3.9 conducted with ZnCl₂ diluent: (a) 0.625:1 ZnCl₂:MoCl₃, 500°C for 14 h; (b) 2.5:1 ZnCl₂:MoCl₃, 500°C for 14 h; (c) the product in b annealed at 900°C for 12 h. The major products were Si, Mo, and β -MoSi₂ for a, Si and Mo for b, and α -MoSi₂ (53 nm) for c.



1> 42-1120: Mo - Molybdenum

2> 17-0653: Mo Cl₂ - Molybdenum Chloride

Figure 3.28 XRD pattern of a production from equation 3.9

Rapid, solid-state reactions that are highly exothermic, such as metallothermic reductions or gasless combustion of the elements, frequently generate large particles due to accelerated diffusion rates. The temperatures attained by the reaction mixtures discussed herein have not yet been established. The theoretical maximum temperature would have been the adiabatic temperature (T_{ad}) for the reaction system [31]. This is the temperature that would be achieved if all of the heat generated by the reaction was absorbed by the products rather than dissipated to the surroundings, a condition that is approached when the reaction rate is fast relative to thermal diffusion rates. For the undiluted Cl displacement reaction, T_{ad} was calculated as > 2293 K (the melting point of $MoSi_2$), which is greater than that for the gasless combustion of Mo and Si (1900 K), but yet very fine particles not much greater than 100 nm were obtained. This may indicate that despite the rapidity of the reaction, it did not proceed adiabatically. Indeed, this is believed to be true because no luminous flash was observed as is typical of an exothermic ignition, and the quartz tube was not damaged by the intense heat. However, this is likely too simplistic of an explanation. The product structure is surely related to mechanism. It was observed for diluted reactions that nanocrystalline Mo was nucleated, and this converted to nanocrystalline $MoSi_2$ with diffusion at elevated temperatures. With undiluted reactions, much of the Mo may react with Si before nucleating so nanocrystalline $MoSi_2$ is directly formed as tiny nanoparticles, or at least $MoSi_2$ is rapidly formed with Si diffusion into the Mo. These particles are formed in conjunction with expanding, byproduct gas. The byproduct mass is evolved, leaving behind a very porous material in which the small $MoSi_2$ particles have little contact with one another. This inhibits diffusional growth. Further, the porosity provides for more surface exposed to the atmosphere and perhaps a significant acceleration in cooling rate.

Prospectus for Self-Propagating Synthesis. The Cl exchange reaction of equation 3.8 is comprised of a redox reaction (essentially Equation 3.9) activating the reaction of Mo and Si. Reaction of the elements can be ignited with a localized heat source so as to undergo a self-propagating high-temperature synthesis (SHS) of $MoSi_2$. This may, then, be possible for the Cl displacement reaction as well (though this has not yet been attempted), since this reaction is more exothermic (vs. kcal/ $moSi_2$), has a lower barrier to initiation, and has more favorable kinetics (Solid-state diffusion is assisted by the elimination of large Mo particles, and disproportionations lead to vapor phase reactants.).

Effecting the reaction in this way is desirable for several reasons. 1) Less energy input and cost would be required. 2) Lower combustion temperatures (the temperature achieved by the reaction mixture) could be achieved. The temperature that an exothermic reaction mixture reaches depends on the prereaction temperature of the mixture. Reducing powder temperatures by nearly 500°C could yield nearly as large a reduction in combustion temperature. This would have an impact on particle sizes, and perhaps the average particle sizes could be reduced to the high end of the nanometer regime without the need of a diluent. 3) Elimination of a preheat to effect reaction initiation could make the reaction process amenable to the more available (cheaper) molybdenum pentachloride. This reactant is not suitable under the reaction parameters studied herein because it volatilizes at 268°C before reaction can be initiated. But, in a self-propagating

mode of reaction, only the reactant immediately preceding the reaction front is heated, so if the reaction propagates rapidly enough, it can be completed before the reactant escapes. This possibility has been demonstrated by Jacubinas and Kaner, who self-propagated a solid-state metathesis (SSM) reaction between MoCl_5 and Mg_2Si (Equation 3.7).[28] Products derived from the pentachloride and trichloride reactants could differ (particularly in particle size) because the pentachloride is more exothermic (meaning potentially higher combustion temperatures and reaction rates) and would convert a higher percentage of Si to SiCl_4 . 4) The reactions conducted herein were thermal explosions which could become more vigorous as the reaction scale is increased and heat can not be as readily dissipated. This could lead to larger particles or violent outventing of SiCl_4 , which should not be problems with localized ignition. The influence of reaction scale has been observed in this research, as is illustrated by the comparison of XRD patterns of the products derived from 0.2, 2.5, and 8 g reaction scales (Figure 3.29). 5) It may be possible to learn more about the reaction mechanism. SHS reactions can be quenched and the microstructure preceding and following the reaction front can be examined.

It is not certain whether powdered mixtures as studied herein will actually be capable of self-propagating a reaction following a localized ignition. The powders may need to be pressed to improve contacts and consequent reaction rates, as is necessary for SHS from the elements (which require at least 30% of theoretical density to self-combust without preheating [32]). However, reaction mechanisms and kinetics using the halide reagents differ from reaction of the elements. The low activation barrier for this reaction compared to the SHS from the elements indicates that it will probably propagate more readily at lower densities. This is supported by the success of Jacubinas and Kaner with igniting unpressed powders containing halide reactant in the SSM synthesis of MoSi_2 . [28]

The combustion temperatures should be much lower than for SHS from the elements accomplished with dense reactants (which combusts at temperatures very near to T_{ad} , which is 1900K), since it is not believed that this combustion would be adiabatic (see above). If the density were increased, however, the combustion temperatures should elevate, as should rates. A problem could arise in that SiCl_4 would be prevented from escaping until the pressure builds up and causes an explosion that breaks apart the pellet. Altering reactant densities, then, could exert some control over product structure. It would be interesting to compare this product structure with that obtained from SHS at comparable combustion temperature.

Reaction with SiH_4 . Rather than reacting molybdenum halides with Si, it may be advantageous to use SiH_4 . Such reactions comprise the conventional chemical vapor deposition route to silicide thin films [33], but large scale reactions to generate a powder have not been attempted to the knowledge of this author. Clearly the use of SiH_4 will not be as practical as Si because it is a comparatively expensive and hazardous material

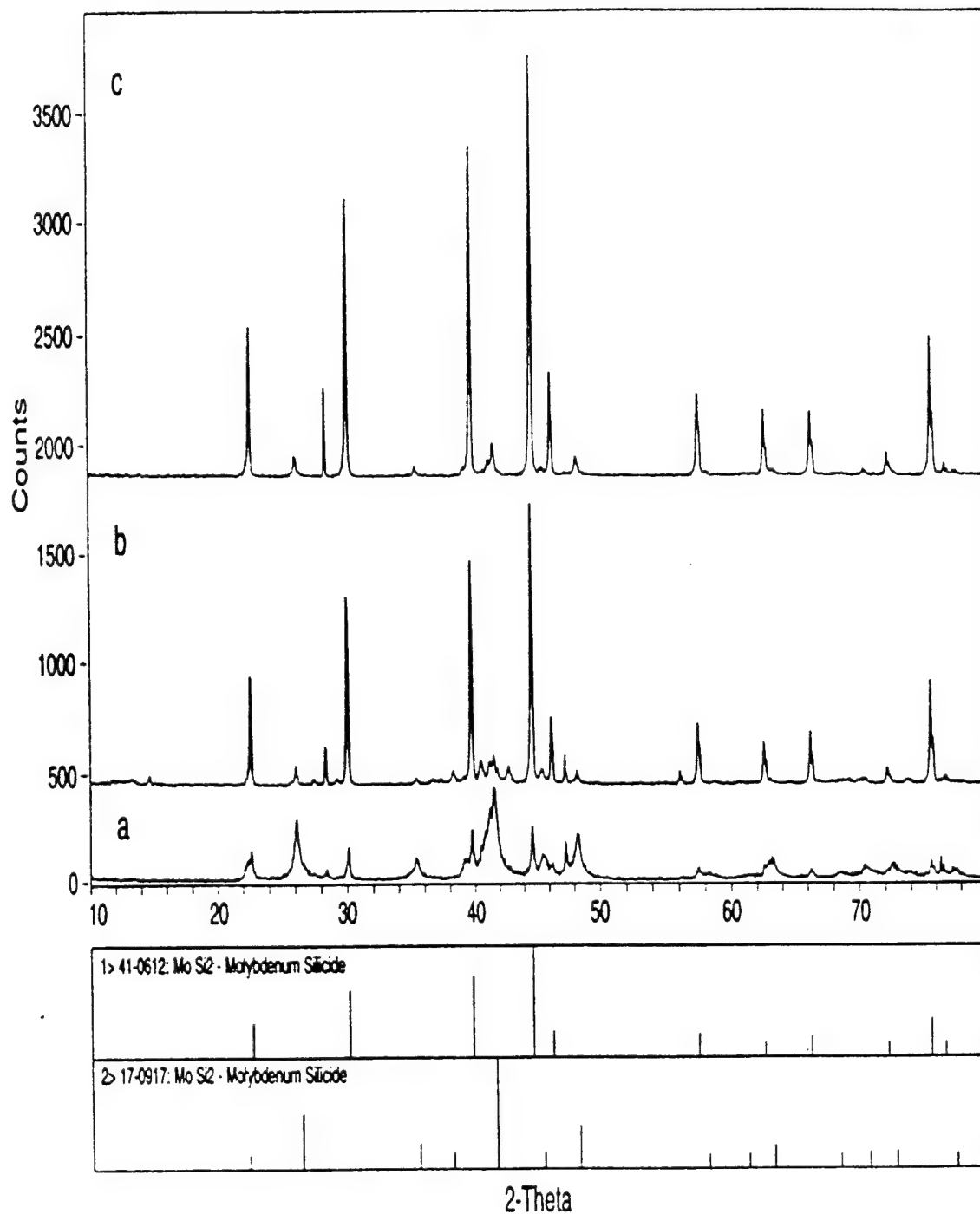


Figure 3.29. XRD patterns for productions of equation 3.9 conducted on varying scales: (a) 0.2 g theoretical MoSi₂ yield; (b) 2.5g; (c) 8 g. As the scale is increased, the exothermic reaction becomes hotter, and the XRD patterns exhibit greater crystallinity.

requiring specialized equipment. However, it is more reactive than Si, and it eliminates the constraints of solid-diffusion encountered with Si. This may allow for the preparation of smaller nanoparticles under milder conditions than can be accomplished with the solid-state reaction. Further, this reaction would not require a diluent. Preliminary reactions have been attempted in a high pressure bomb (in the presence of a solvent), but the temperature limit (350°C) was not adequate for inducing significant reaction. This method, of course, will only be of interest if it affords nanostructures that can not be prepared by other methods.

Cl Displacement as a General Strategy for Preparing Intermetallic or Ceramic Materials. Formation of SiCl_4 provides a sufficient thermodynamic driving force for many of the transition metal halides to undergo analogous displacement reactions to that presented herein. However, the exothermicity of few such reactions approach that of equation 5.3 for MoSi_2 . One such reaction having a lesser enthalpic driving force was attempted for the the preparation of VSi_2 (Equation 3.10). Reaction did



not initiate until 600°C, and the combustion was incomplete. Only trace silicide was obtained without further annealing at 900°C. Unlike the annealed reaction products of diluted MoSi_2 reaction mixtures, the VSi_2 obtained by annealing was not nanocrystalline by XRD. It is not clear, then, that chlorine displacement reactions will provide a viable strategy for preparing a variety of nanocrystalline silicides. Clearly some of the more desirable refractory silicides, Ti_5Si_3 and Zr_5Si_3 , will not be obtained by this reaction strategy, as the titanium and zirconium halides are too stable, making the balanced reactions endothermic. Such reactions have been attempted and indeed were unsuccessful.

Consideration has been given to whether other intermetallics and ceramics, such as transition metal borides, aluminides, carbides, germinides, phosphides, etc. could be prepared by similar chlorine displacement reactions. Most of these ceramic or intermetallic compounds, however, do not have very negative heats of formation, so they would only procede if the byproduct chloride is sufficiently negative. Because the heat of formation of most of the product compounds is not very great, the byproduct halide must be very stable for the enthalpic driving force of a reaction to be sufficient for spontaneous ignition. Of the byproduct halides, only the heat of formation of AlCl_3 (-139.4 kcal/mole) is not inferior to SiCl_4 (-157.03 kcal/mole) on a per-mole-of-chlorine basis. The byproduct halides generated by most such reactions would be inferior to SiCl_4 as a driving force. The exception is AlCl_3 , which has a heat of formation of -139.4 kcal/mole compared to -157.03 kcal/mole for SiCl_4 , hence making it superior on a per mole of chlorine basis. This strategy may be suitable, then, to the preparation of aluminides. One interesting possibility would be to mix aluminum and silicon with MoCl_3 to make an $\text{Mo}(\text{Si},\text{Al})_2$ alloy. This may stabilize the C40 structure of MoSi_2 [34], which has more

slip systems and may therefore exhibit superior ductility and fracture toughness over C11b MoSi₂ below 1000°C. [35]

4 CONSOLIDATION OF NANOPARTICLES

4.1 Development of a Micromechanistic Model.

To realize the full benefits of nanocrystalline features, the nanoparticles should be compacted to dense products with the retention of nanograins, minimal contamination, and free of nanopores and other defects. Room and elevated temperature uniaxial compaction, cold isostatic pressing (CIP) / cold uniaxial compaction followed by conventional sintering, sintering followed by rolling, rapid sintering, plasma-activated sintering, sinter-forging, and hot isostatic pressing (HIP) are some of the commonly used methods for consolidation. With the exception of a few investigations [36-41], the consolidation parameters have thus far been selected mostly by trial and error and in most cases the processing conditions used have not produced the desired nanograined quality product.

Micromechanistic models for conventional powder densification [42,43] and related software / sensor tools [44] are not applicable to nanocrystalline systems [45] because of the following distinct and unique characteristics of nanoparticles: (a) Because of fine particle size, the possibility of new or different mechanisms of densification should be considered. Pronounced surface diffusion in nanoscale compacts enhances grain/interparticle sliding as well as vacancy diffusion [46]. Increased grain boundary volume, short bulk and boundary diffusion paths, the presence of vacancy clusters, diffusion of individual crystallites, and the dominant role of triple junctions may lead to altered bulk and grain boundary diffusion rates [47]. (b) The high interparticle adhesiveness compared to conventional powder leads to different levels of agglomeration [48,49]. This tendency to agglomerate can severely affect densification kinetics [50,51]. The adhesiveness leads to different levels of interparticle and interagglomerate friction. (c) Nanoparticle ensembles have large surface areas making them very susceptible to impurity intake relative to coarse powder. Both surface and bulk impurities play an important role in densification [52]. Oxygen contamination of powder during storage causes decreased compaction [53], impurity atoms increase interparticle friction [47], impurities stabilize nanopores and prevent their closure [47], impurities may segregate preferentially to boundaries and hinder mass transport [54], oxide layer delays densification [55,56,57], and the oxide problem is more severe at higher temperature due to increase in oxidation [56-58]. Internal pressure effects caused by adsorbed gases may be more pronounced in nanoparticle systems [47,53,55,56-59] due to drastic increase in surface area. (d) low dislocation density, and low stability of dislocations due to fine size in nanoparticles may reduce their plastic deformability and green compaction may require pressures greater than a threshold [38,39,47,60,61]. The different dislocation structure and behavior may alter the mechanism of creep which is a dominant densification mechanism in many material systems. It has been recently observed that the creep rates in nanocrystalline materials are not twelve orders of magnitude high. Creep rates calculated using Nabarro-Herring and Coble creep equations lead to several orders of magnitude higher creep rates in nanocrystalline materials than in conventional materials. However, only modest increases in creep rates have been observed in

nanocrystalline materials [62] mainly because the grain size dependent threshold stress for creep which becomes significant as the grain size is reduced to nanometer levels [63]]. (e) Other factors such as, diffusion induced grain boundary migration and boundary energy induced rotations may alter densification mechanisms [67].

A generalized and comprehensive model which takes into account a multitude of variables due to different densification processes, unique nature of nanoparticles, and densification parameters, is necessary to understand the nanoparticle densification process and aid in optimizing processing conditions. The observations in literature regarding densification behavior and mechanisms are in many cases conflicting and show a pronounced dependence on material system, synthesis, and processing variables, to a much larger extent than in the case of conventional powder [37,38,41,53-61,65-73]. In the area of modeling of densification of nanoparticles, there has been only limited work to date [79,80].

The objective of the present study was to theoretically model and understand the densification and microstructure evolution of nanoparticle systems with the incorporation of unique characteristics of nanoparticles. The hot isostatic pressing model developed by Ashby and co-workers [43] was used as a framework to generate density versus consolidation parameters diagrams to generate optimal consolidation conditions and obtain information on operative densification mechanisms. Comparison of model results with experimental data on densification behavior is presented in the next section.

Model Construction

The Helle-Easterling-Ashby (HEA) model [43] which successfully predicts the densification of conventional powders [86,88] was modified substantially to incorporate several factors unique to nanoparticle aggregates. The modified model takes into account the effect of grain boundary and bulk impurities, and different levels of agglomeration in nanoparticle systems, incorporates effects due to less number of dislocations per particle and low stability of dislocations due to fine size in nanoparticles, and leads to prediction of densification behavior and grain growth during densification of a general nanoparticle system. The present model considers both uniaxial as well as hydrostatic pressing, as these two are the most commonly used techniques for nanoparticle densification. The factors that were incorporated to account for nanoparticle systems are discussed in the following sections. Symbols have been kept consistent with those used by Ashby and co-workers [43,86] and are also explained in the material property data listed in appendix A.

Changes to Global Stresses

When a powder system is uniaxially pressed, the compressive stress is accurately known. However, the radial stresses are unknown and usually lower than the uniaxial stress. The lower radial stresses cause a lowering of the effective densification rates than those predicted for hydrostatic compaction. The rate equations during uniaxial pressing,

therefore, require modification. This was accomplished by introducing a factor involving stress localization functions as suggested by the modeling of Besson and Abouaf [88]. For a densifying powder mass, the densification rate ($\dot{\rho}$), where ρ the relative density, is related to the gross strain rate by the following:

$$-\frac{\dot{\rho}}{\rho} = \dot{\varepsilon}_{11} + \dot{\varepsilon}_{22} + \dot{\varepsilon}_{33} \quad (4.1)$$

Besson and Abouaf derived equations for the strain rates during HP and HIP using stress localization factors. Applying equation (1) to the cases of HP and HIP and dividing the two results gave the factor by which densification rate in HP is lower with respect to HIP for each densification mechanism. This factor is:

$$F = \left\{ \frac{c(\rho)}{c(\rho) + 4f(\rho)} \right\}^{0.5} \quad (4.2)$$

where

$$c = 1 + \{k_1(1 - \rho)\}^{k_2} \text{ and } f = k_3(1 - \rho)^{k_4}. \quad (4.3)$$

The functions c and f were obtained by curve fitting experimental data on different metals. The values of k_1 , k_2 , k_3 , and k_4 used were 28.55, 1.678, 20.18, and 1.572, respectively. The HEA [43] HIP rate equations have to be multiplied by this factor for correcting for the stress state during hot pressing.

The effect of the can shielding during HIP was taken into account according to the analysis of Wadley et al. [86]. The reduction in effective pressure on the powder inside the can is given by:

$$\Delta P = 0.07\sigma_y^{\text{can}}(T) \quad (4.4)$$

Effect of Impurities

The effect of impurities was taken into account by using impurity modified bulk diffusivities, grain boundary diffusivities, surface energies, and grain boundary energies [89-91]. The surface energy and grain boundary energy are reduced due to impurities [92]. For a trace impurity (dilute) system, assuming the Langmuir isotherm holds, it may be combined with the Gibb's adsorption isotherm, which yields the equation for surface or grain boundary free energy

$$\Delta\gamma_{\text{surf}; gb} = RT\Gamma_b^o \left[1 - \frac{\Gamma_b}{\Gamma_b^o} \right] \quad (4.5)$$

where

$$\frac{\Gamma_b}{\Gamma_b^0} = \beta_b X_c \quad (4.6)$$

$$\Gamma_b^0 = \left(\frac{1}{N_a a_{su}^2} \right) \quad (4.7)$$

where Γ_b^0 is the quantity of solute in mol/m², N_a is Avogadro's number, β_b is the enrichment ratio, and X_c is the concentration in mol fraction of the segregant species. The change in surface and grain boundary energies were taken into account in the following manner:

$$\gamma_{surf}^{imp} = \gamma_{surf} - \Delta\gamma_{surf} \quad (4.8)$$

$$\gamma_{gb}^{imp} = \gamma_{gb} - \Delta\gamma_{gb} \quad (4.9)$$

The bulk diffusivity in a material with segregated impurities is given by [59]:

$$D_v^* = D_v (1 + b_v X_c) \quad (4.10)$$

where b_v is the segregation factor and X_c is the bulk concentration in mol fraction of solute. The segregation factor may assume positive or negative values depending on the material system. The grain boundary diffusivity is modified as [89]:

$$D_b^* = D_b \left[1 + \left\{ b_v - \frac{2\Delta}{m_i} \times \left(\frac{a_{sv}}{a_{su}} \right)^2 \beta_b \right\} X_c \right] \quad (4.11)$$

where m_i is the number of effective layers of the impurity atoms, a_{sv} is the size of the solvent atom, a_{su} is the size of the solute atom, Δ is the grain boundary width, and β_b is the enrichment factor. The number of layers of impurities in the grain boundary is given as:

$$m_i = \frac{\Delta}{a_{su}} \quad (4.12)$$

Values of β_b and b_v are listed for several material systems in Refs. [90,91].

The above equations are only applicable to dilute systems. In highly impure systems, a different approach was followed. Since the diffusivity is dependent on the change in the activation energy, the following equations were used for evaluation of

modified activation energies and modified pre-exponents. The change in activation energy for boundary diffusion due to impurities is given as:

$$Q_b^{\text{imp}} = Q_b + N_a \alpha'_{\text{imp},1} a_{\text{su}}^2 + N_a \alpha'_{\text{imp},2} a_{\text{su}}^2 + \dots \quad (4.13)$$

depending on the number of impurities segregated to the grain boundary [92]. For example, the presence of trace amounts of carbon in a Ni-16Cr-9Fe alloy resulted in an increase of grain boundary activation energy by 50 kJ/mol, corresponding to a factor of 10^{-5} decrease in diffusivity [93]. The lattice activation energy modified due to the impurities in the bulk or on the interface are given as:

$$Q_v^{\text{imp}} = \frac{Q_b^{\text{imp}}}{0.66} \quad (4.14)$$

or

$$Q_v^{\text{imp}} = Q_v + \Delta E \quad (4.15)$$

where ΔE is the activation energy associated with decrease in defect migration due to drag of defects by impurity atoms [94]. The pre-exponents for the diffusivities in both trace impurity and impure systems were modified as:

$$D_o^{\text{imp}} = D_o \exp\left(\frac{-\delta S}{R}\right) \exp\left(\frac{-C}{RT}\right) \quad (4.16)$$

and [94]

$$\delta S = \frac{\lambda \delta Q}{T_m} \left\{ \frac{T_m}{G_o} \times \frac{\partial G}{\partial T} \right\} \quad (4.17)$$

where λ is a constant equal to 0.55 for fcc and 1 for bcc materials, G is the shear modulus, T_m is the melting temperature, δQ is the difference in activation energy due to impurities, and C is $\sim 10 - 50$ kJ/mol [94]. The diffusivities in the high impurity systems are then given by the normal Arrhenius relationship with the modified pre-exponents and activation energies.

Effect of Frictional Forces

The effect of die-wall friction in reducing the effective uniaxial stress on the compact during hot pressing was taken into account using the results obtained by Wilkinson [84]. The effective pressure is given as:

$$P_{\text{eff}}^{\text{dw-friction}} = P_{\text{appl}} \exp\left\{-\frac{2\mu_{\text{dw}} Ht(\rho)}{\text{Dia}}\right\} \quad (4.18)$$

and

$$Ht(\rho) = Ht_o \left(\frac{\rho_o}{\rho}\right) \quad (4.19)$$

where μ_{dw} is the die-wall friction, $Ht(\rho)$ is the instantaneous height of the compact, and Dia is the diameter of the compact.

The interparticle friction effects become more severe in nanoparticle systems due to the high adhesiveness of the nanoparticles [95,96]. Following the approach suggested by Geguzin [97], the effect of interparticle friction in reducing effective stress for densification was developed. As shown in Figure 4.1, the spherical particles are modeled as cubes to aid in analysis. The effective force, due to the external applied pressure is F_{eff} minus the frictional force, $F_{\text{frictional}}$, at the two surfaces of contact. It can be derived that the reduced effective applied pressure, due to the interparticle friction effect, is:

$$P_{\text{appl}}^{\text{ip-friction}} = P_{\text{appl}} \exp\left[-\left(\frac{\mu_{\text{ip}}}{\sqrt{3}}\right) \times \left(\frac{\rho - \rho_o}{1 - \rho_o}\right)^{1/2}\right] \quad (4.20)$$

for stage 1. There is no interparticle friction effect in stage 2. In a similar fashion, the factor for inter-agglomerate friction can be derived. It has the same form as that for interparticle friction, except that the friction coefficient, μ_{ia} , is different for interagglomerate friction.

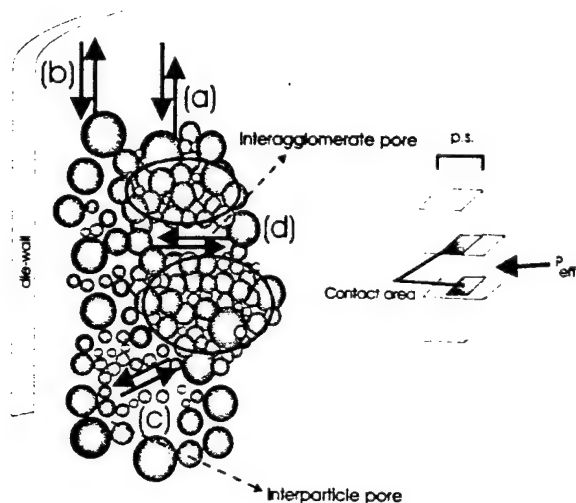


Figure 4.1: Schematic of die-wall friction for agglomerates (a) and particles (b), interparticle friction (c), and interagglomerate friction (d), effects in reducing the effective pressure for densification. The schematic on the right is an aid to derive the interparticle friction equation (Eqn. (4.20)).

Effect of threshold stress

The threshold stress reduces the effective stress during creep and was incorporated into the densification rate equations due to power law creep, Nabarro-Herring creep, and Coble creep. The threshold stress was previously given as [74]:

$$\sigma_t = \frac{GK}{g} \exp\left\{\frac{U}{kT}\right\} \quad (4.21)$$

where G is the shear modulus, K is a constant with units of length, g is the grain size, and U is a constant with units of energy. The value of U was found to be of the order of 10 kJ/mol in the magnesium system without impurities [98]. In this regard, this paper was one of the first to report the observation of the threshold stress in a pure material. Usually, the threshold stress has been observed only in impure systems, multi-phase systems, or materials with precipitates or dispersoids [99,100]. The threshold stress due to fine grain size seems to be related to the motion or restriction in motion of grain boundary dislocations [98,99]. It must be realized that the concept of threshold stress for creep is not well understood.

Two problems are associated with equation (4.21). The first is the constant K which is not dimensionless. The other is the reciprocal of grain size dependence, which leads to unrealistic values of the threshold stress at nanocrystalline grain sizes. The nature and values of U are also material dependent. The following modification were made to

the original threshold stress function, i.e. equation (4.21). Hansen [101] states that for fine grain sized materials, the strength vs. grain size relationship is given as:

$$\sigma = \sigma_o + \alpha G \sqrt{\varepsilon} (C_2 b)^{1/2} g^{-1/2} \quad (4.22)$$

where α and C_2 are constants, G is the shear modulus, b is the Burger's vector, g is the grain size, and ε is a constant strain. If the threshold stress is due to dislocation phenomena near grain boundaries, it should be related to G , b , and g in a similar fashion as in equation (4.22). The value of 10-20 kJ/mol for the activation energy term, U , is approximately equal to $(Q_{core}/10)$ in the case of magnesium. Combining this and the earlier observation, the equation for threshold stress was derived to be

$$\sigma_t = KG \sqrt{b} g^{-1/2} \exp \left\{ \frac{0.1 Q_{core}}{RT} \right\} \quad (4.23)$$

where the constant K is $\sim 10^{-3}$ for a variety of materials (Mg, Cu - SiO₂, Cu - 2% Cr - 0.3% Zr, and so on). The advantage with equation (23) is that the constant K is now dimensionless, and a universal equation is available which predicts threshold stress values which are reasonable. Figure 4. 2 shows plots of σ_f vs. g and σ_f vs. T/T_m . The threshold stress effect can be substantial for small grain/particle sizes. It can be noted that at high grain sizes the threshold stress is similar to the Peierl's stress ($\sim 0.5 - 1$ MPa). It can be argued that the nanocrystalline material is a two phase material with the grain boundary phase making a substantial fraction of the volume. The threshold stress may also explain the lower Hall-Petch slopes in nanocrystalline metals. A recent description of grain boundary morphologies at ultrafine grain sizes [102] suggests that the intrinsic, orientation sensitive, grain boundary stress state may play a significant role in effecting deformation at the relatively high applied stresses that are reached because of Hall-Petch strengthening. The concept of threshold stress needs further investigation, both in nanocrystalline materials and conventional materials. Following the analysis of HEA [43] and equation (4.23), the pressure terms corresponding to threshold stress are:

$$\Delta P_{appl}^{ts} = \frac{1}{3} KG \sqrt{\frac{b}{d}} \exp \left[\frac{0.1 Q_{core}}{RT} \right] \left\{ \frac{\rho^2 (\rho - \rho_o)}{1 - \rho_o} \right\} \text{ for stage 1, and} \quad (4.24)$$

$$\Delta P_{appl}^{ts} = \frac{1}{3} KG \sqrt{\frac{b}{g}} \exp \left[\frac{0.1 Q_{core}}{RT} \right] \text{ for stage 2.} \quad (4.25)$$

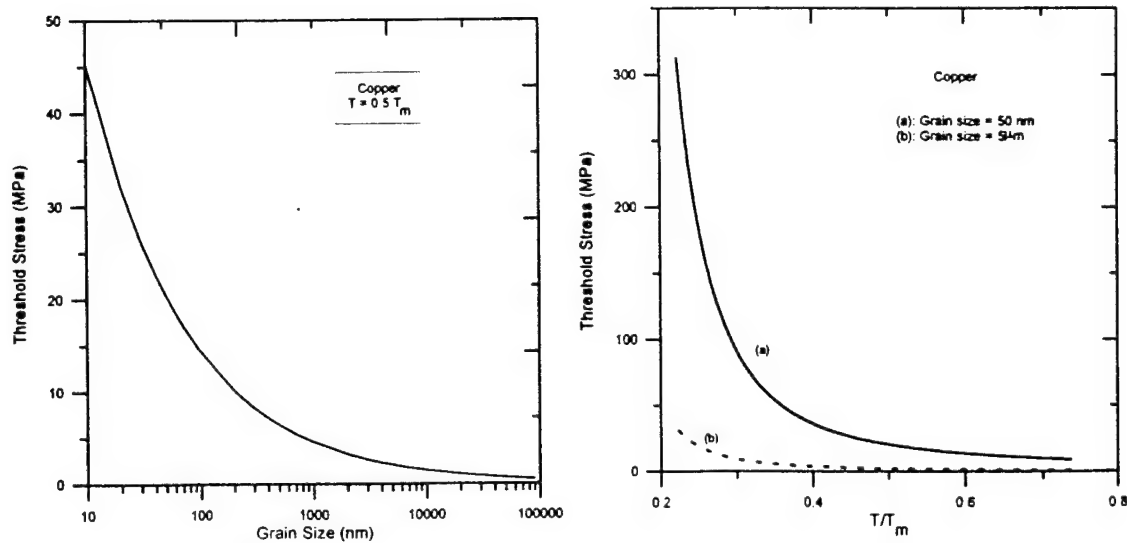


Figure 4. 2: Threshold stress for creep vs. (left) grain size at $T = T_m/2$, and (right) T/T_m at grain size of 50 nm and 5 μm . The model material is copper. For material property data used to draw these plots see Ref. [85].

Effect of agglomeration

The effects of agglomeration were incorporated using the approach of Lange [103]. The powder system is assumed to consist of some volume fraction of agglomerated particles (which for the unagglomerated case will be zero) and the remaining volume fraction is unagglomerated. The agglomerated region (region I) is shown by the region enclosed by ellipses in Figure 4.1. The densification of the powder ensemble is modeled as these two systems densifying in a simultaneous manner. Thus, the rate equations are integrated for the different regions and the densities obtained for the two regions are added using a rule-of-mixtures equation based on the volume fractions of each region. As suggested by Ashby and co-workers [43] the densification in each region is in itself modeled as in two stages. In the first stage the nanoparticles/domains/agglomerates are distinguishable from each other. This is the stage of interconnected porosity (Stage 1). The second stage is modeled as the elimination of an array of closed pores and is equivalent to the stage of closed porosity (Stage 2).

Other Modifications

The diffusion rates have generally been written as dependent on the third (N-H) or fourth (Coble) inverse power of grain size. However, this is because in conventional powder systems the grain size is approximately equal to the pore radii. However, in nanocrystalline systems this is not necessarily the case and the pore radii may be orders of magnitude different from the particle size. This factor was pointed out by Mayo and Chen [104] and has been included as a modification in the rate equations used in the present study. The effect of decreasing number of pores on the densification rate has been

studied by Evans and Hsueh [105] and was included as a modification of the surface tension assisted densification rate equations. As suggested by Evans and Hsueh [74] this factor plays a major role only in surface tension driven rate equations and is insignificant in pressure driven rate equations. This factor, which is to be multiplied to the rate equations due to surface tension driven mechanisms, is given by:

$$G = \left\{ \frac{1 - \rho}{1 - \rho_0} \right\}^{m_p/3} \quad (4.26)$$

where m_p is a constant and is ≈ 3 for conventional powders and is $\approx 8 - 12$ for nanocrystalline powder systems.

Grain growth law

It has been shown [106] that the normalized shrinkage rate of large pores is linearly related to the normalized grain growth rate as:

$$\frac{1}{r_p} \frac{\partial r_p}{\partial t} = -\beta \frac{1}{g} \frac{\partial g}{\partial t} \quad (4.27)$$

where β is a constant of proportionality. This equation can be integrated to give a relation between pore radii and grain size as:

$$g = g_0 \left[1 + \frac{1}{\beta} \left(1 - \frac{r_p}{r_p^0} \right) \right] \quad (4.28)$$

The pore radii is given as:

$$r_p = \left\{ \frac{3(1 - \rho)}{4\pi N_v} \right\}^{1/3} \quad (4.29)$$

and the pore number density as a function of relative density (ρ) is given as:

$$\frac{N_v}{N_0} = \left(\frac{1 - \rho}{1 - \rho_0} \right)^m \quad (4.30)$$

Using equations 4.28, 4.29, and 4.30, the relationship between grain size and relative density can be derived as:

$$g = g_o \left[1 + \frac{1}{\beta} \left(1 - \frac{1-\rho}{1-\rho_o} \right)^{(m+1)/3} \right] \quad (4.31)$$

Lange [107] has argued that such grain size - density correlations arise from a thermodynamic constraint against sintering in the absence of grain growth. Large voids intersecting many grain boundaries will sinter only until the pore intersects a critical number of boundaries. Grain growth is then required to increase the number of boundaries intersected for continued sintering. Full densification requires the elimination of all pores which in turn requires that pores remain in contact with grain boundaries. Contact is maintained if mobility of pores is greater than that of the boundaries. For large pores, the coefficient β is small, of the order of 0.05 - 0.1. At this stage, the grain growth rate is much greater than pore shrinkage rate due to the small potential for sintering [105]. For small pores, on the other hand, when the pore size is similar to grain size in nanoparticle systems, β is larger. This is because the grain growth rate is reduced and there is a high potential for sintering [105]. Mayo et al [108] have observed in their sintering and sinter-forging studies on nanocrystalline ceramics (TiO_2 and Y_2O_3) that pore shrinkage occurs only when grains reach a critical size with respect to the pore size. The grain size in nanocrystalline ceramics was observed to be similar to the average spacing of open pores. It is intuitive to correlate this parameter β with the coordination number of particles of each pore. Lange and Kellet [109] have shown that for a simple array of particles the grain size increases as a function of the coordination number of particles near a pore, and this correlation is given by:

$$g = g_o 2^{m/3} \quad (4.32)$$

where m is related to the ratio of the original coordination number (n_o) and the critical coordination number (n_c) below which pores are unstable and will close immediately. This relation is given as:

$$m = \frac{\log \frac{n_o}{n_c}}{\log 2} \quad (4.33)$$

If the following equation is used for the factor in relation to the pore coordination numbers:

$$\beta = \frac{1}{2^{m/3} - 1} \quad (4.34)$$

then, the arbitrary constant β can be explained in a physical sense. Also, this relationship results in values of $\beta \approx 0.05 - 0.1$ for large pores (large initial pore coordination number) and reasonable values, $\approx 0.4-0.6$, for small pores. For $n_o = n_c$, i.e., when the

critical pore coordination number is reached, the value of β is infinite, indicating that the pore is unstable and shrinkage occurs without any or little grain growth. The grain growth law used in the model calculations for the large and small pore region utilize equations 4.31 - 4.33 to predict grain size in the as-pressed compacts. Since the two regions (interparticle and interagglomerate) achieve full densification at different times during pressing, the region that is fully dense earlier will experience normal grain growth while the other region is densifying. Once both regions are dense, the whole compact will experience normal grain growth for any excess pressing time. A grain growth law of the type:

$$g^3 = g_o^3 \exp \left\{ \frac{-Q_{gg}}{RT} \right\} (t - t_d) \quad (4.35)$$

can be employed to predict final microstructures. This simple extension can be added to the code developed in this work. However, it must be realized that nanocrystalline compacts may not exhibit normal grain growth behavior in some cases. In fact, abnormal grain growth have been reported in nanocrystalline compacts of copper [110,111] and nickel [112].

Model Implementation

A computer code capable of generating diagrams of density versus the consolidation parameters (T, p, t) was developed by incorporating the effects on densification of the above factors, namely, impurities, agglomeration, and less number of dislocations per particle and low stability of dislocations due to fine size in nanoparticles. Additionally, densification rates can be plotted against the densification parameters. Finally, microstructural features in the as-pressed compacts, such as interface, triple junction, grain boundary, and pore volumes, can be predicted as discussed in detail in Ref. [113]. The computer code utilizes user specified information regarding the kind and level of impurities, and the level of agglomeration which can be easily obtained or estimated by experimental methods on the nanoparticles. The code is primarily divided into powder consolidation by: (1) cold pressing, (2) hot pressing, and (3) hot isostatic pressing, though the model is also capable of predicting densification behavior during pressureless sintering.

The calculations conducted by the computer code are completed in 4 basic steps. The flow chart for the model calculations is given in Figure 2. The first step is the calculation of cold pressed density. The density that is achieved due to the an applied pressure, p, is [43]:

$$\rho = \left[\frac{(1 - \rho_o)(p - \Delta p_{1,l})}{1.3\sigma_y(T)} + \rho_o^3 \right]^{1/3} \quad (4.36)$$

where σ_y is the yield strength of the nanoparticle in the unagglomerated region and is the yield strength of the agglomerate in the agglomerated region. This is accomplished by using equation (4.36) and iteratively calculating the value. Iteration is required since the pressure modification terms (internal pressure, and so on) are density dependent. The second step is the calculation of density after plastic yielding at the specific temperature. This also utilizes equation (4.36) and iteratively calculates the value. This value is the starting density for other time dependent mechanisms. Depending on the case, that is, impure, trace impurity, or pure, the specific modifications are made as outlined previously. Depending on the stress state, that is, uniaxial or hydrostatic, the rate equations are modified as outlined earlier. The third step is the calculation of final relative density by integrating the densification rate equations for stage 1 and 2 of region I (volume fraction of unagglomerated powder), and similarly for region II (volume fraction of agglomerated powder). Stage 1 represents densification occurring while the pores are interconnected, and stage 2 represents the final stage when pores are isolated. The fourth step is the calculation of grain size.

Miscellaneous equations that are required for the model, such as, smoothing functions, which smooth the transition from stage 1 to stage 2, as used by Schaefer [86] were used in the present code. The term for decrease in pressure due to entrapped or evolving gases [43] is given as:

$$\Delta P_{\text{int}} = P_{\text{int}}^{\text{initial}} \left(\frac{\rho}{1-\rho} \times \frac{1-\rho_o}{\rho_o} \right) \left(\frac{\rho^2(\rho-\rho_o)}{1-\rho_o} \right) \text{ for stage 1, and} \quad 4.37)$$

$$\Delta P_{\text{int}} = P_{\text{int}}^{\text{initial}} \left(\frac{\rho}{1-\rho} \times \frac{1-\rho_c}{\rho_c} \right) \text{ for stage 2.} \quad (4.38)$$

The following are the densification rate equations for the densifying powder compact under hydrostatic stress state. The factor, F (equation (2)), can be multiplied to each rate equation if the stress state is uniaxial. Densification rate due to a mechanism was assumed to be zero if the applied stress (due to pressure or surface tension) was less than internal pressure during stage 1. However, in stage 2, where the pores are isolated, negative densification rates were allowed. As mentioned previously, symbols have been kept consistent with those used by Ashby and co-workers [43,86] and are also explained in the accompanying article [65].

Plastic Yielding:

Assuming time to achieve final pressure is small, the densification rate is infinite if applied pressure exceeds the yield strength of the nanoparticle. Below this critical stress, the densification rate is zero. The density attained due to application of pressure is given by equation (77). This density is reached "instantaneously" after the pressure is

applied to the powder compact. This equation is only applicable to stage 1 of the densification process.

It has been realized [38,39,47,60,61] that there exists a threshold stress for nanoparticle compaction, below which there is no appreciable change in density. Skandan et al [38,39] explain the effect on the basis of the driving force for densification. The driving force is given as:

$$DF = \gamma\Omega K + g^* P_{appl} \quad (4.39)$$

where γ is the surface energy, Ω is the molecular volume, K is inversely proportional to grain size, g^* is a geometric constant, and P_{appl} is the applied pressure. It was argued that at very small grain sizes the pressure term is insignificant. However, the explanation may not be correct in all cases. Raj [114] has shown that the true driving force for surface tension driven densification is given as:

$$DF = \frac{2\gamma_b}{g} \pm \frac{2\gamma}{r} \quad (4.40)$$

where g is the grain size and r is the pore curvature, and depending on curvature, the second term can be positive or negative. Depending on the size ratio of pore to particle/grain the curvature may be different. Especially in agglomerated powders, the pore size may be much greater than grain size. Evans and Hsueh [105] have schematically shown that as the grain size is decreased, under the condition that pore size \gg grain size the driving force for densification is high. In this case pressure application is beneficial to enhanced densification. Only in the case of pore and grain size being similar, the explanation of Skandan et al [38] is valid.

The threshold stress for cold compaction has been explained in terms of low dislocation density resulting in high strength of nanoparticles [47,60,61]. The present model follows a similar approach for cold compaction. The initial threshold is to break the agglomerate, as described in [85]. The final threshold is to plastically deform individual nanoparticles. The threshold stress factor is evident from examination of equation (4.36), where $p \ll \sigma_y$ implies very little or no compaction. The yield strength of the nanoparticles and agglomerates are calculated as described in the accompanying paper [85].

Volume diffusion - pressure driven, Stage 1, Region I:

$$\dot{\rho}_{vd-pd,1,1} = \frac{D_v \Omega}{r^2 kT} \left[43 \frac{(1-\rho)^2}{(\rho - \rho_o)} S_1(\rho) \right] (p - \Delta p_{1,1}) \quad (4.41)$$

Volume diffusion - pressure driven, Stage 2, Region I:

$$\dot{\rho}_{vd-pd,2,I} = \frac{D_v \Omega}{r^2 kT} \left[270 \sqrt{1-\rho} \left(\frac{1-\rho}{6} \right)^{1/3} S_2(\rho) \right] (p - \Delta p_{2,I}) \quad (4.42)$$

Volume diffusion - surface tension driven, Stage 1, Region I:

$$\dot{\rho}_{vd-st,1,I} = G \frac{D_v \Omega}{r^2 kT} \left[72 \frac{1-\rho}{\rho - \rho_o} \rho_o S_1(\rho) \right] \left\{ \frac{1-\rho}{1-\rho_o} \right\}^{m/3} \left(\frac{2\gamma_{surf}}{r_p} - \Delta p_{1,I} \right) \frac{r_p}{2} \quad (4.43)$$

Volume diffusion - surface tension driven, Stage 2, Region I:

Figure 4.4. $\dot{\rho}_{vd-st,2,I} = G \frac{D_v \Omega}{r^2 kT} \{ 36 S_2(\rho) \} \left(\frac{2\gamma_{surf}}{r_p} - \Delta p_{2,I} \right) \frac{r_p}{2} \quad (4.44)$

Boundary diffusion - pressure driven, Stage 1, Region I:

$$\dot{\rho}_{bd-pd,1,I} = \frac{\Delta D_b \Omega}{r^3 kT} \left[43 \frac{(1-\rho)^2}{(\rho - \rho_o)^2} S_1(\rho) \right] (p - \Delta p_{1,I}) \quad (4.45)$$

Boundary diffusion - pressure driven, Stage 2, Region I:

$$\dot{\rho}_{bd-pd,2,I} = \frac{\Delta D_b \Omega}{r^3 kT} \left[18 \left(\frac{1-\rho}{6} \right)^{-1/3} S_2(\rho) \right] (p - \Delta p_{2,I}) \quad (4.46)$$

Boundary diffusion - surface tension driven, Stage 1, Region I:

$$\dot{\rho}_{bd-st,1,I} = G \frac{\Delta D_b \Omega}{r^3 kT} \left[18 \left(\frac{1-\rho_o}{\rho - \rho_o} \right) \left(\frac{\rho}{\rho - \rho_o} \right) S_1(\rho) \right] \left(\frac{2\gamma_{gb}}{r} - \Delta p_{1,I} \right) \times r \quad (4.47)$$

Boundary diffusion - surface tension driven, Stage 2, Region I:

$$\dot{\rho}_{bd-st,2,I} = G \frac{\Delta D_b \Omega}{r^3 kT} \left[18 \left(\frac{1-\rho}{6} \right)^{-1/3} S_2(\rho) \right] \left(\frac{4\gamma_{gb}}{g} - \Delta p_{2,I} \right) \left(\frac{g}{4} \right) \quad (4.48)$$

Nabarro-Herring and Coble Creep, Stage 1, Region I:

$$\dot{\rho}_{nhcc,1,I} = \left\{ \frac{D_v}{g^2} + \frac{\pi \Delta D_b}{g^3} \right\} \frac{\Omega}{kT} \left\{ 14.4 \left(\frac{1 - \rho_o}{\rho - \rho_o} \right)^{1/2} S_1(\rho) \right\} (p - \Delta p_{1,I}) \quad (4.49)$$

Nabarro-Herring and Coble Creep, Stage 2, Region I:

$$\dot{\rho}_{nhcc,2,I} = \left\{ \frac{D_v}{g^2} + \frac{\pi \Delta D_b}{g^3} \right\} \frac{\Omega}{kT} \{ 32(1 - \rho) S_2(\rho) \} (p - \Delta p_{2,I}) \quad (4.50)$$

Power Law Creep, Stage 1, Region I:

$$\dot{\rho}_{plc,1,I} = D_{crp} \left(\frac{p - \Delta p_{1,I}}{\sigma_{ref}} \right)^n \frac{3.1 \rho \sqrt{\rho - \rho_o}}{\sqrt{1 - \rho_o}} \left(\frac{1 - \rho_o}{3 \rho^2 (\rho - \rho_o)} \right)^n S_1(\rho) \quad (4.51)$$

Power Law Creep, Stage 2, Region I:

$$\dot{\rho}_{plc,2,I} = D_{crp} \left(\frac{p - \Delta p_{2,I}}{\sigma_{ref}} \right)^n 15 \rho \left(\frac{1.5}{n(1 - (1 - n)^{1/n})} \right)^n S_2(\rho) \quad (4.52)$$

Interparticle Sliding - pressure driven, Stage 1, Region I:

$$\dot{\rho}_{ips-pd,1,I} = \Delta D_b a_{sv}^2 (p - \Delta p_{1,I}) \left(\frac{1 - \rho_o}{2 r_p k T \rho^{7/3} (\rho - \rho_o)} \right) S_1(\rho) \quad (4.53)$$

Interparticle Sliding - surface tension driven, Stage 1, Region I:

$$\dot{\rho}_{ips-st,1,I} = G \frac{\Delta D_b a_{sv}^2}{k T r_p r} (1 - \rho_o) \left\{ \frac{1 - \rho_o}{\rho^{7/3} (\rho - \rho_o)} \right\} \left(\frac{2 \gamma_{surf}}{r_p} - \Delta p_{1,I} \right) S_1(\rho) \quad (4.54)$$

Interparticle sliding is absent during stage 2.

Interagglomerate sliding - pressure driven, Stage 1, Region II:

$$\dot{\rho}_{ias-pd,1,II} = \frac{\Delta D_b a_{sv}^2}{k T 2 r} (1 - \rho_o) \left\{ \frac{1}{\rho^{7/3} (\rho - \rho_o)} \right\} (p - \Delta p_{1,II}) S_1(\rho) \quad (4.55)$$

Interagglomerate sliding - surface tension driven, Stage 1, Region II:

$$\dot{\rho}_{ias-st, I, II} = G \frac{\Delta D_b a_{sv}^2}{k T r_p r} (1 - \rho_o) \left\{ \frac{1}{\rho^{7/3} (\rho - \rho_o)} \right\} \left(\frac{2\gamma_{surf}}{r_p} + \frac{2\gamma_{gb}}{r} - \Delta p_{I, II} \right) S_1(\rho) \quad (4.56)$$

Total densification rate for region I:

$$\dot{\rho}_I = \sum_{y=1}^2 \dot{\rho}_{x,y,I} \quad (4.57)$$

where x denotes the mechanism and y denotes the stage.

The pressure term in each equation is suitably modified depending on the effective internal pressure and the factors of reduction in pressure due to interparticle or interagglomerate friction. The densification rate equations for region II can be readily written by replacing the pore radii terms with the pore radii of the large interagglomerate pores, by replacing the Δp term with the appropriate term for region II, and suitably modifying other factors like the exponent for changing number of pores. The total densification rate for region II is, then:

$$\dot{\rho}_{II} = \sum_{y=1}^2 \dot{\rho}_{x,y,II} \quad (4.58)$$

where x denotes the mechanism and y denotes the stage. The densification rate equations for each mechanism is linearly added and integrated to calculate the relative density corresponding to a specific combination of pressure, temperature, and time. The same calculation is performed for region II. The two density results are weighted according to the volume fraction of large and small pores as suggested by equation (90). If necessary, the densification rates themselves can be evaluated for densification rate versus consolidation parameter maps. Depending on the volume fraction of the small or large pores in the system, the final density calculation is made by a rule-of-mixtures.

$$\rho_{final} = v_f^I \rho_I + v_f^{II} \rho_{II} \quad (4.59)$$

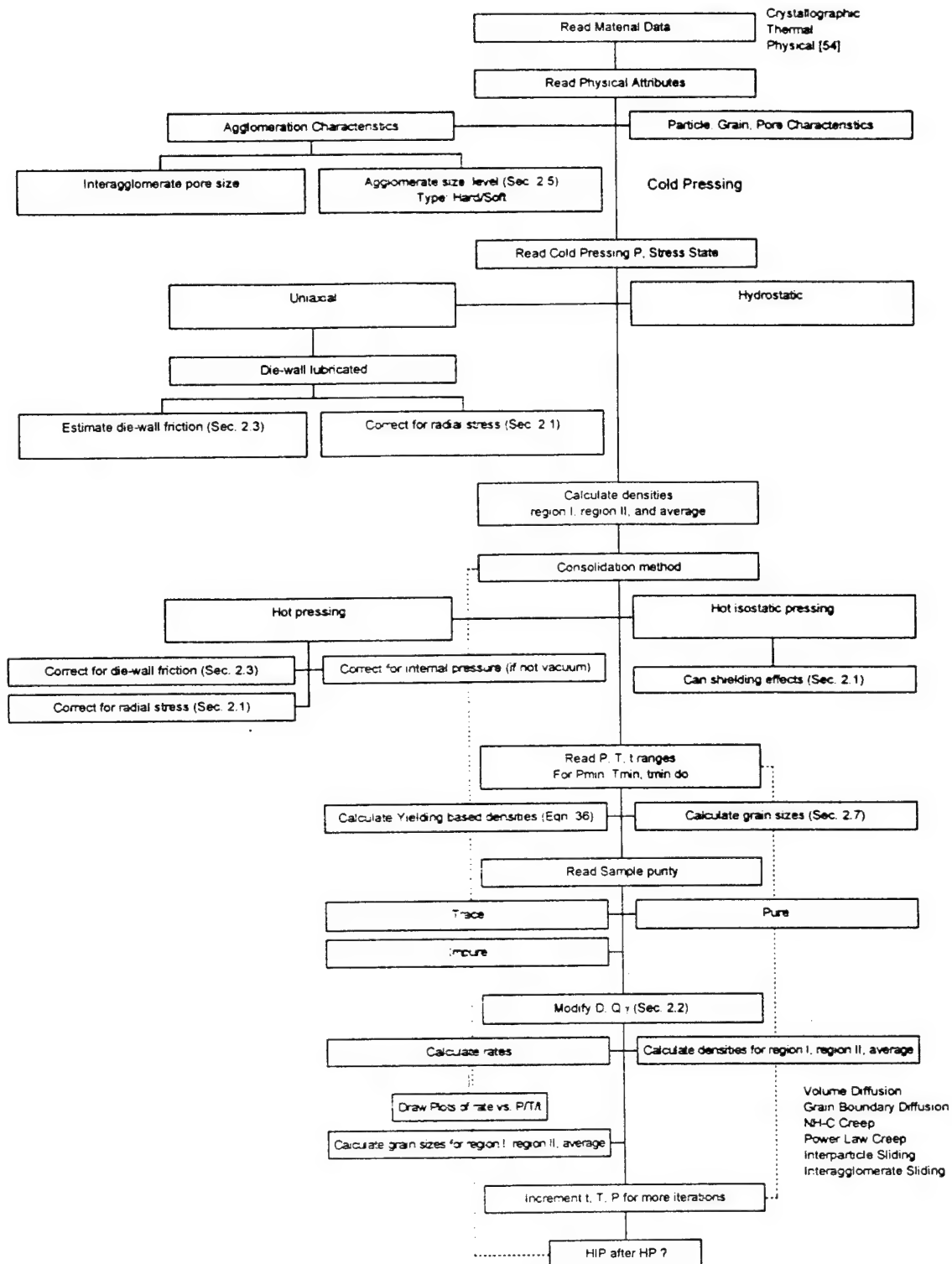


Figure 4.3: Flow chart used to write codes for calculation of density variation with applied pressure, temperature, and time; to calculate optimal combination of P, T, and t. Material data consists of values of diffusion constants, creep constants, viscous flow constants, mechanical property values etc. Physical data consists of initial density, grain/particle size, and so on.

Model Predictions:

Model calculations were performed using material property data, listed in Table A1 (Appendix A). The material property data includes, atomic, physical, mechanical, thermal data, and information about agglomeration, impurities, and so on. Appendix A lists the sources of various data and discusses different estimations used.

Figures 4.4 -4.8 show the effects of various process and material parameters on densification of MoSi_2 .

4.2 Comparison of Model Predictions with Experimental Measurements:

Nanoparticles were pressed by uniaxial hot pressing and/or hot isostatic pressing. The samples were cold pressed before being pressed at elevated temperatures. Powders of the initial batches that contain impurities due to exposure to air during pre-compaction handling, and powders that were not exposed to air, were pressed to compare densification behavior and quantitatively determine effects of impurities on densification.

Consolidation by Vacuum Hot Pressing (VHP) and Inert-atmosphere Hot Pressing (IHP):

A vacuum hot press with the maximum capability of 1650°C and 140 MPa pressure was used to press the nano powders. Pressure of 100-140 MPa and temperatures depending on the material system were used to hot press powder for a period of 2 - 4 hours. The die has an inner diameter of 12.7 mm and a height of 25.4 mm. The powder was cold pressed in air and the die-punch assembly was inserted in the vacuum chamber and the chamber was evacuated for sufficient time (usually overnight) until the vacuum was better than 1×10^{-5} Torr. A pre-load of 20 - 50 MPa was always maintained to hold the inside assembly in alignment. The furnace was heated using a temperature controller with a precision of $\pm 2^\circ\text{C}$. After the required temperature was reached, the final pressure was applied for a specified time. Once pressing was complete temperature was lowered at a rate of $\sim 10^\circ\text{C}$ per min. and pressure was brought back to the pre-load level. After total cool down the die-punch assembly was removed and the sample was carefully removed from the inside. There are, however, some shortcomings of the vacuum hot pressing system. The location was away from the nanoparticle synthesis facility. Even with extreme care during transportation, this leads to exposure of nanocrystalline powder to air (O_2), resulting in impure materials which can reduce densification rates during pressing. Also, cold pressing is done in air, leading to further exposure of the sensitive nanoparticles to air. The pressure capacity of the press is also limited to 140 MPa. Therefore, a new hot press was constructed, and was located in an Ar glove box. This allows the powder to be pressed without (less than 3 ppm) exposure to oxygen. Also, the capacity of the press is ~ 1 GPa (on a 12.7 mm cross section), which implies \sim five-ten

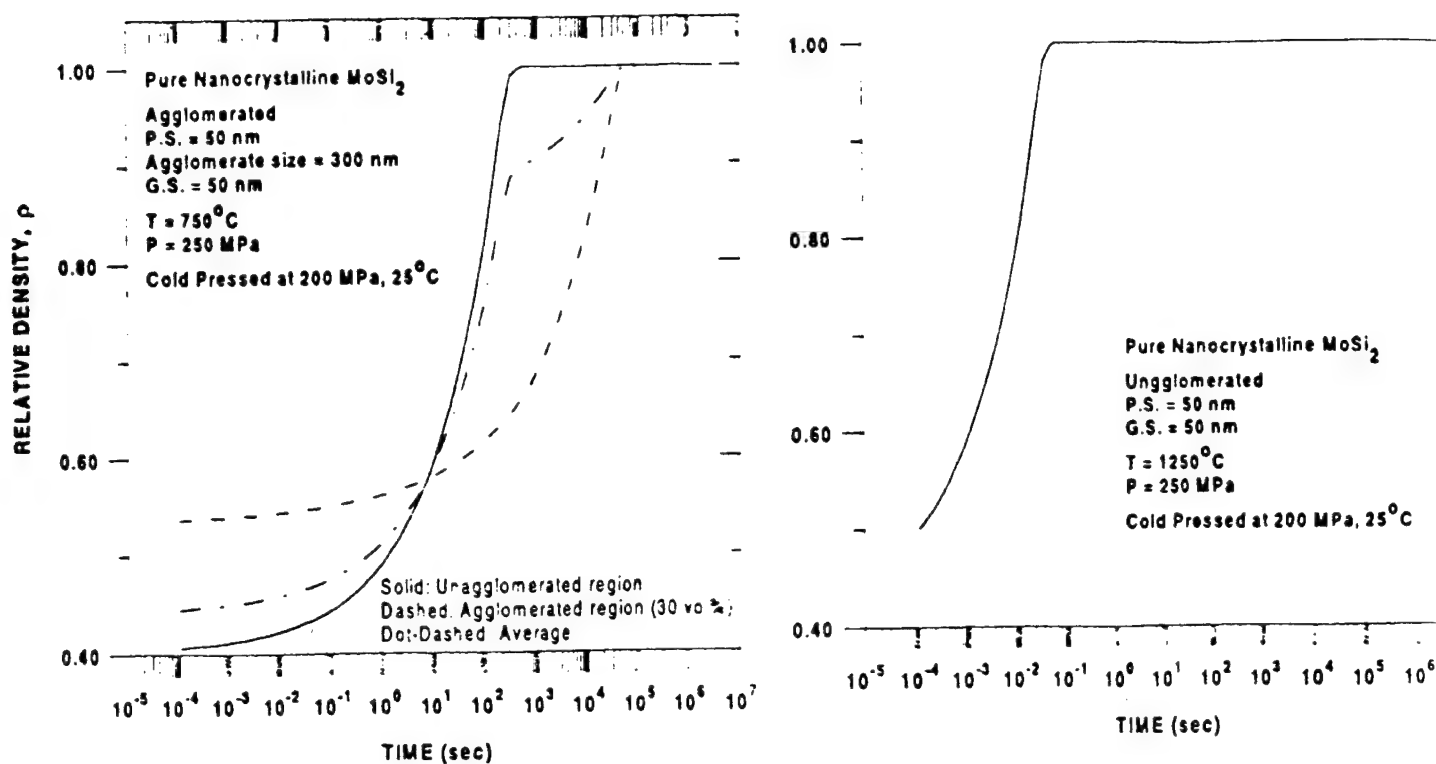


Figure 4.4 Model predictions for densification of MoSi₂ showing the effect of temperature at constant pressure 250 MPa (a) $T = 750^\circ\text{C}$ (b) $T = 1250^\circ\text{C}$.

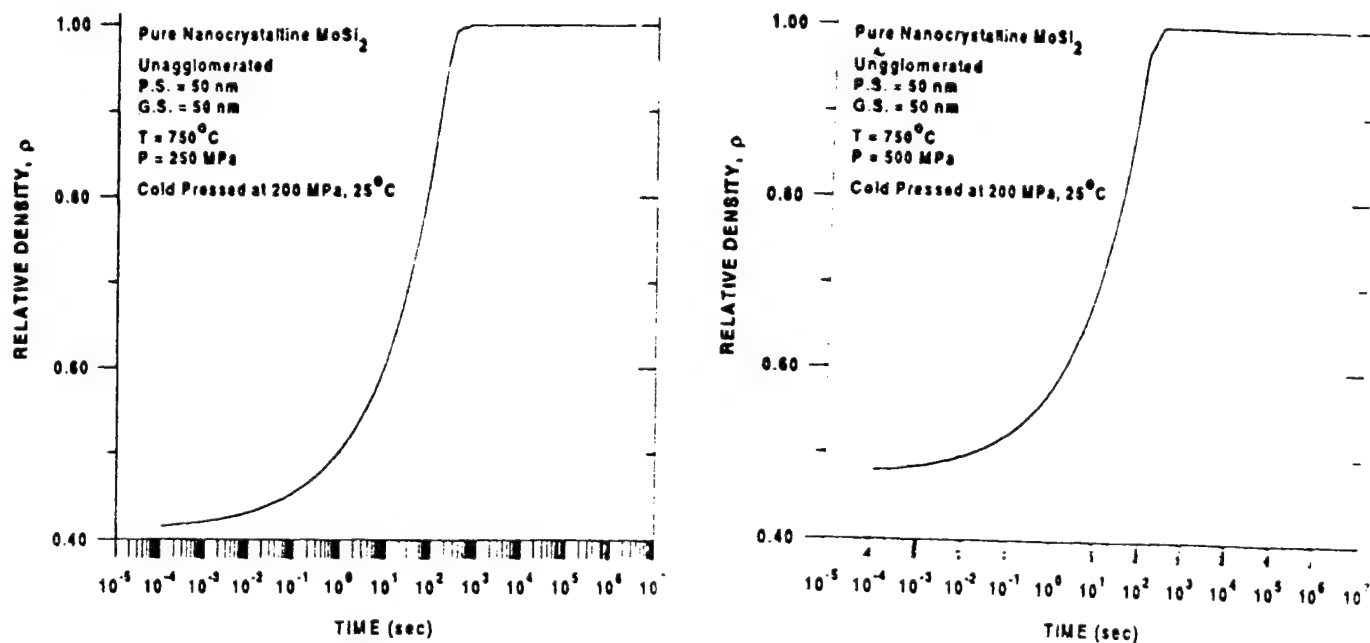


Figure 4.5. Model predictions for densification of MoSi₂ showing the effect of pressure at constant temperature 750°C (a) $P = 250\text{ MPa}$, (b) $P = 500\text{ MPa}$.

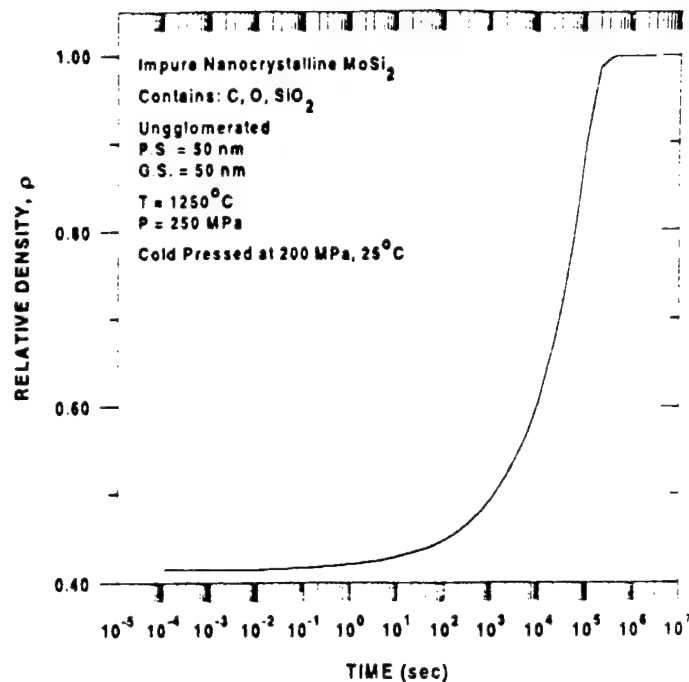
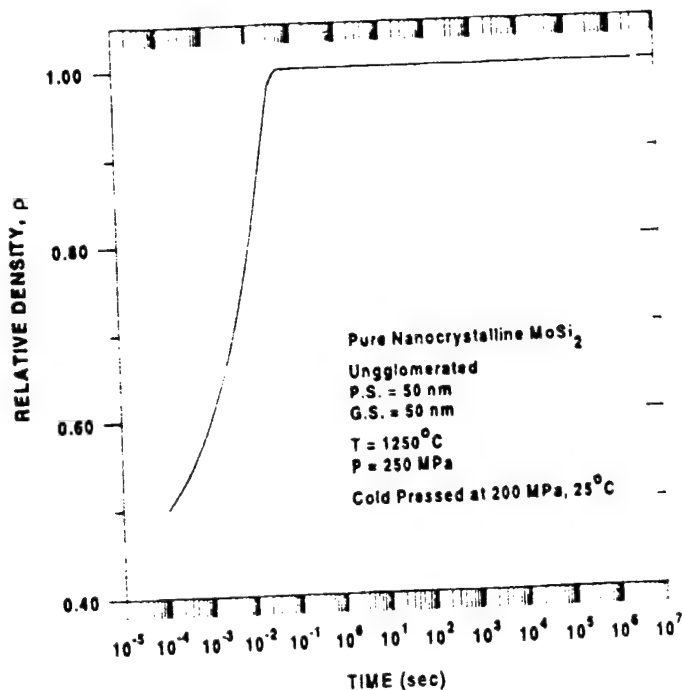


Figure 4.6 Model predictions for densification of nanocrystalline MoSi_2 showing the effect of impurities on densification at constant temperature of 12150°C, pressure of 250 Mpa. (a) Pure nanocrystalline MoSi_2 , (b) Nanocrystalline MoSi_2 containing C, O, and SiO_2 impurities.

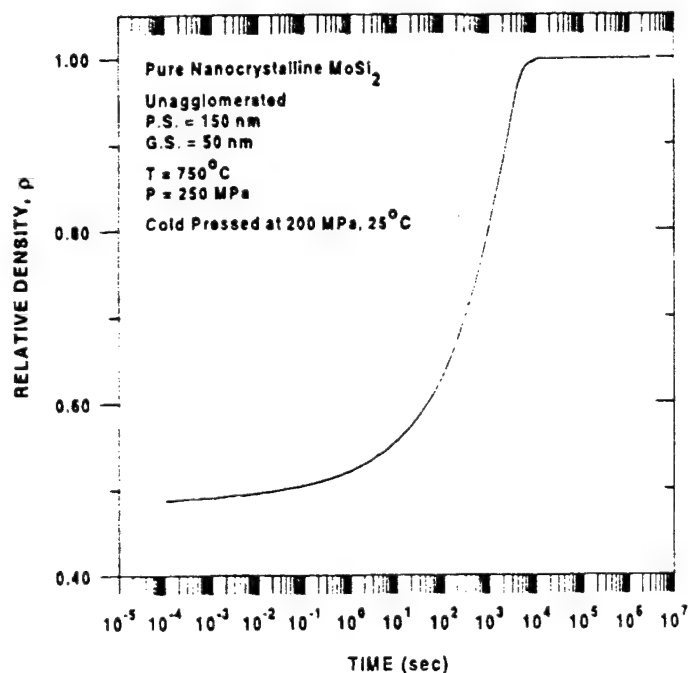
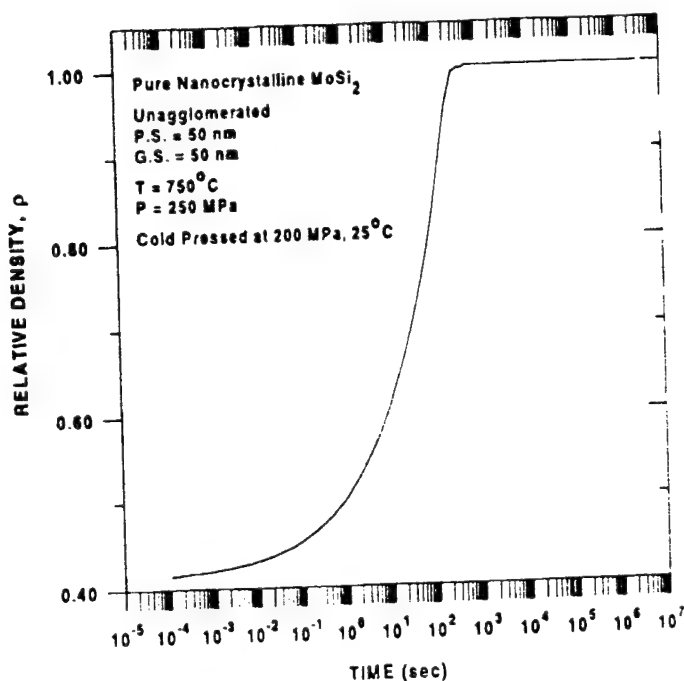


Figure 4.7. Model predictions for densification of nanocrystalline MoSi_2 showing the effect of particle size on densification at constant temperature of 750°C, and pressure of 250 Mpa. (a) Particle size = 50 nm, (b) particle size = 150 nm.

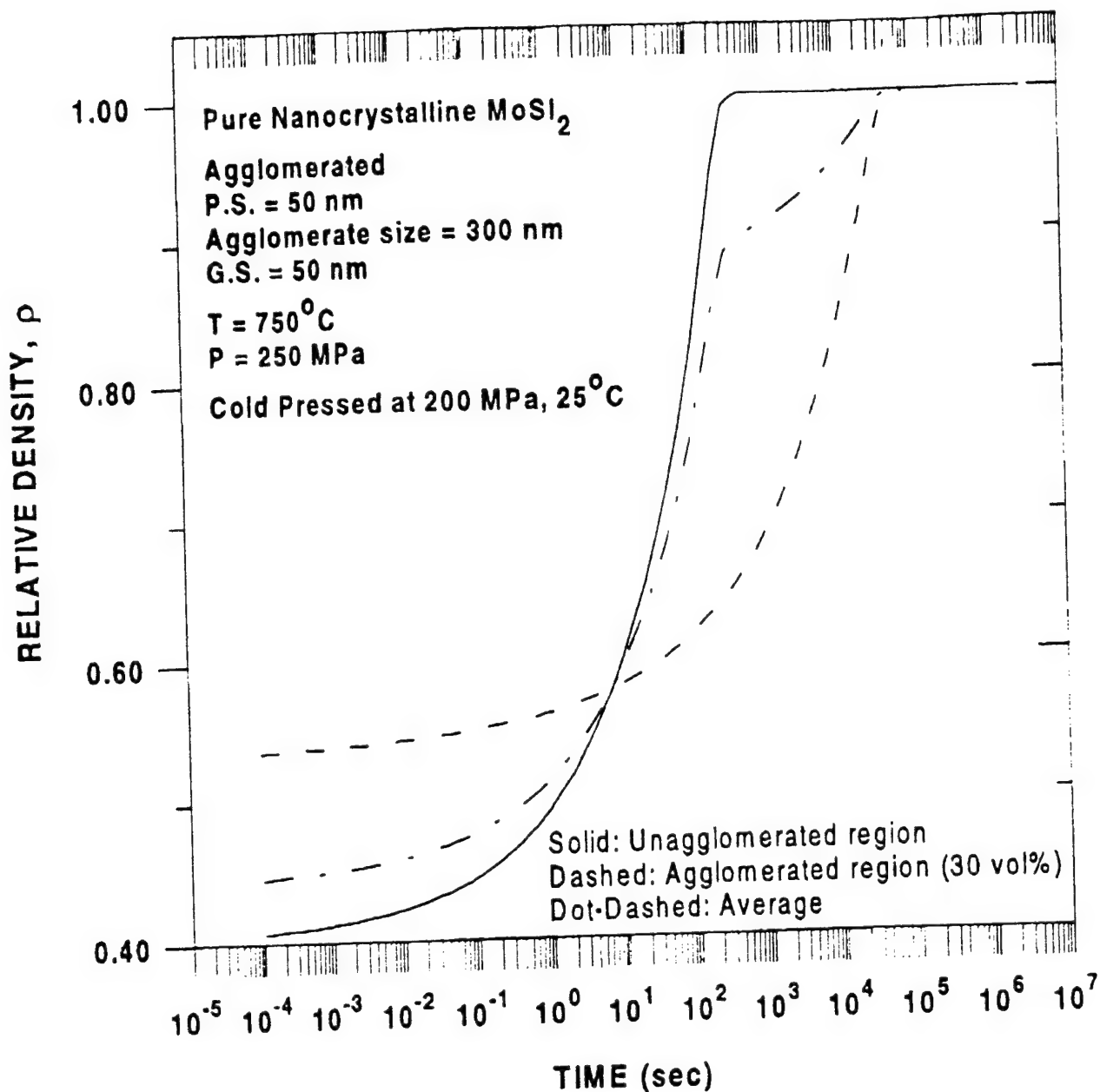


Figure 4.8 Model predictions for densification of nanocrystalline MoSi₂ showing the effect of agglomeration on densification at constant temperature of 750°C, pressure of 250 Mpa.

times the pressure of the vacuum press system. The temperature capacity of this press is comparable with a maximum of 1600°C .

A schematic of the argon hot press is given in Figure 4.9

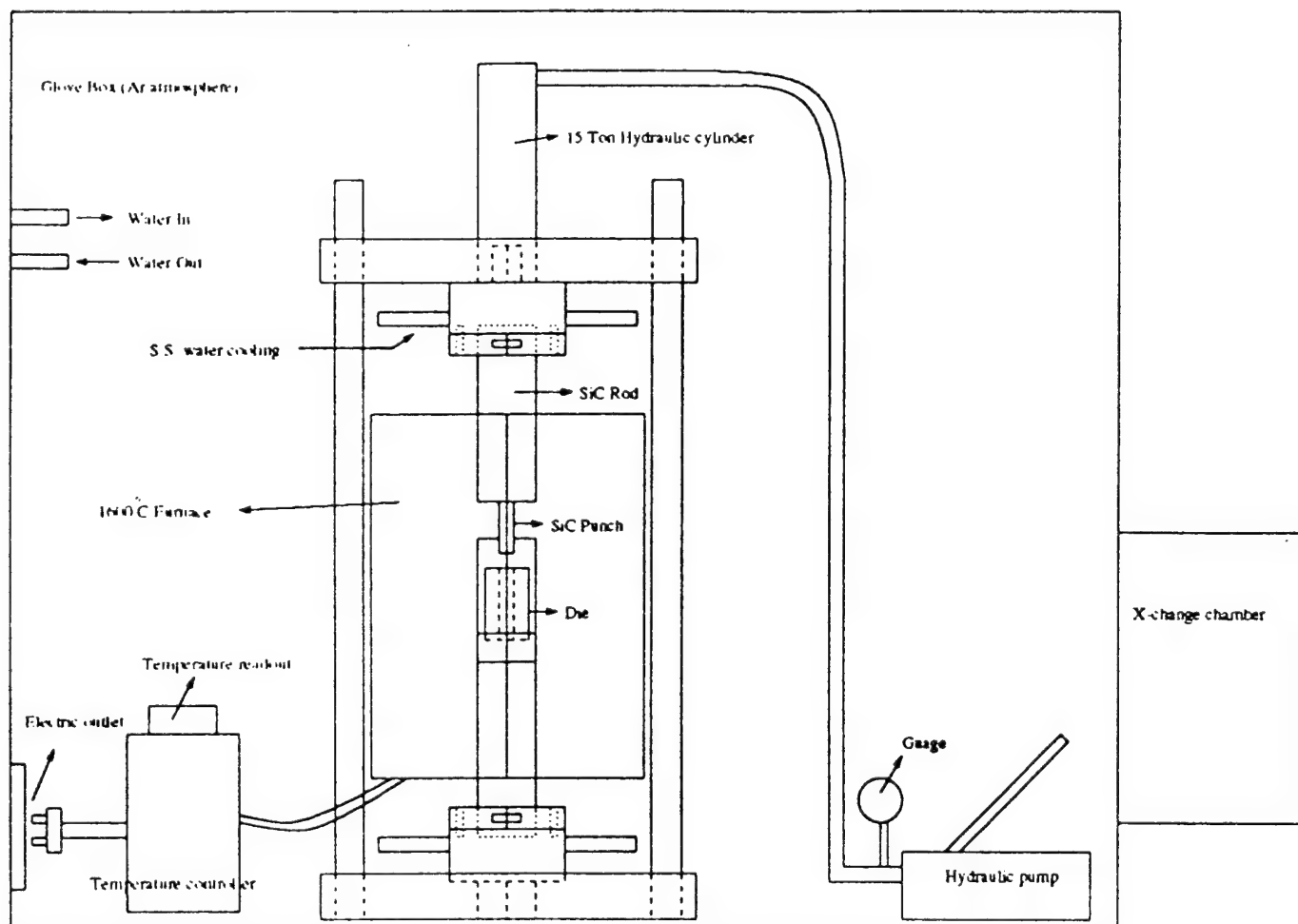


Figure 4.9: Uniaxial hot press in the argon glove box. The hydraulic press has a maximum pressure capacity of 1 GPa (12.7 mm diameter die) and a temperature capacity of 1600°C .

Consolidation by Hot Isostatic Pressing (HIP):

A hot isostatic press (ASEA model Q1H3, Sweden) was used to isostatically press, both un-pressed powder and nanopowder samples which had been initially pressed by cold/hot pressing or sintering, to obtain samples with high densities. The HIP is capable of a maximum pressure of 207 MPa and a maximum temperature of 1800°C. The sample to be pressed is sealed in-vacuo using a titanium or niobium can. The sample is then HIP'ed according to a schedule (depending on the material) and cool down is controlled to minimize thermal gradient induced microcracking in the samples.

Consolidation of MoSi₂ Nanoparticles:

MoSi₂ nanoparticles produced by sonochemistry exhibited very poor cold compaction. These MoSi₂ nanoparticles were cold pressed to ~ 20% relative density at 150 MPa. Solid-state reaction synthesized MoSi₂ powder exhibited better cold compaction behavior. These MoSi₂ nanoparticles were cold-compacted at 175 MPa to ~ 30% relative density. Pressure of 100 - 140 MPa and temperatures of 1200-1250°C were used to hot press powder for a period of 2 - 4 hours using VHP. IHP was also used to press MoSi₂ nanoparticles with pressures of 375 MPa, temperatures of 800 - 1400°C, for periods of 1 - 4 h. High density samples exhibited severe macro-cracking in the as-pressed state. To avoid this, cool-down was slowed and temperature was lowered at ~ 100°C per 0.5 h down to 900°C, followed by fast cool down. Pressure was also brought down to ~ 20 MPa at the start of cool-down. Some powders of MoSi₂ were directly HIPed at 207 MPa, for 4 h at temperatures ranging from 1000 - 1600°C. In yet other cases, the previously HPed samples were further densified by HIP.

Precision density measurements were performed by the Archimedes principle technique using a precision microbalance. Since accurate chemical compositions were determined for the nanocrystalline copper samples, the relative density calculations were based on the value for single crystal copper containing impurities. For the calculation of density of copper containing impurities, it was assumed that the impurities were in interstitial or substitutional sites depending on their size relative to that of copper. Relative density calculations for MoSi₂ were based on the value for single crystal pure MoSi₂. This simplification may result in underestimating density values due to impurities of C and O, and the possibility of amorphous SiC phases in the starting powder. Optical metallographic analysis and scanning electron microscopy were performed to measure porosity independently and determine grain and pore structures.

The consolidation conditions, sample and powder designations, and the density and grain size results obtained are listed in Table 4.1. Most samples have relative.

densities in the range of 70 - 90% of the theoretical density of MoSi₂. Samples that were only VHP'ed exhibited large pores and tended to be brittle. Samples that were only HIP'ed exhibited similar pore structures. The samples that were HIP'ed after HP'ing exhibited much finer sized spherical porosity. Samples pressed with higher pressures and high temperatures in the argon hot press exhibited only fine scale pores. The relative densities in these samples were in the > 90% range

Table 4.1: Powder, sample, consolidation technique, consolidation conditions, impurity, relative density of MoSi₂ samples in the study.

Powder ^a	Purif. ^b	Phases ^c	PS ^c (nm)	Pellet	CP ^c	Press ^c	T/P/t (°C-MPa-h)	Phases ^c	GS ^c (nm)	ρ (%) ^d	VHN ^d (GPa)	K _{IC} ^d (MPa√m)
SB1	900			SB1A	Air	VHP	1200-100-1	C,A	45	71.1		
SB2	900	A,J	22	SB2A	Air	VHP	1200-100-2	A,B,C,D		61.6		
				SB2A'		HIP	1200-207-4	A,B,C,D	70	62.2	11.5	
SB3	H ₂ O ^d	H		SB3A	Air	VHP	1250-140-2	B,E,D,G		78.9	11.1	
SB4	900	A	19	SB4A	Air	VHP	1100-140-4	A	19			
				SB4A'		HIP	1200-207-4	A,B	79	81.1	13.4	
SB4	900	A	19	SB4B	Air	VHP	1150-140-4	A	38	77.8	15.3	3.8
SB5	900	A,C	< 20	SB5A	Air	VHP	1175-140-5	A,B	26	79.0	10.9	
SB6	900	A,B	28	SB6A	Air	VHP	1200-100-4	A	43	81.2	12.5	4.3
SB7	900	A,C	47	SB7A	Air	VHP	1200-100-0.25	A,B				
				SB7A'		HIP	1100-207-4	A,B	44	83.0	14.3	4.3
SB6,7	900	A,C,B		SB6,7A	Air	HIP	1000-207-4	A,B	66	73.6	12.0	
SB8	900	A,C	42	SB8A	Air	HIP	1300-207-4			75.4	12.6	
SB9	900+H ₂ O	A,C	35	SB9A	Air	HIP	1400-207-4	A,B,C,D	40	67.0	16.6	5.6
SB10 ^{SC}	900+H ₂ O	A,F,C	47	SB10A	Air	HIP	1500-207-4	C,F,D,B	36	60.4	14.1	9.1
SS1	500	H,I,A,E,B	< 20	SS1A	Ar	AHP	800-700-4 ⁱ	A,B		70.9		
SS1	500	H,I,A,E,B	< 20	SS1B	Ar	AHP	900-525-4 ⁱ	A,B				
SS2	MeOH	A,H,I,E	< 20	SS2A	Ar	AHP	1400-375-0.5	A	40	>90 ^m	12.5	4.0
SS2	MeOH	A,H,I,E	< 20	SS2B	Ar	AHP	1400-375-4	A	32	>95 ^m	15.0	4.8
SS3	MeOH	A,H,I,E	< 20	SS3A	Ar	AHP	1300-175-4	A	82	79.7 ^m	14.4	3.2
SS4	MeOH	A,H,I,E	< 20	SS4A	Ar	AHP	1400-375-0.5	A	38	97.9	16.3	3.2
SS4	MeOH	A,H,I,E	< 20	SS4B	Ar	AHP	1400-280-1	A	91	90.7 ^m		
SB11	900	A,B,C	< 20	SB11A	Ar	AHP	1400-260-0.5	A				
				SB11A'		HIP	1500-207-4	A,C,F	95	80.0		

^a SB = solution-based reaction, SS = solid-state reaction using a diluent (ZnCl₂ for SS1, and LiCl for the others), Blanks designate further consolidation of the pellet from the previous row. SB10 contained 35 vol% (excluding impurities) SiC whiskers

^b Purification (salt elimination): 900 = sublimation at 900°C, 500 = sublimation at 500°C, H₂O = washing with water, 900+H₂O = annealing at 900°C and then washing with H₂O, MeOH = washing with methanol

^c Phases detected by XRD listed in order of decreasing X-ray intensities: A = MoSi₂, B = Mo₅Si₃, C = Mo₃Si₃C, D = SiO₂, E = Mo₃Si, F = SiC, G = Mo₂C, H = Mo, I = Si, J = MoO₂.

- d* Particle or grain size determined by XRD line broadening of MoSi_2 reflections ($\text{Mo}_5\text{Si}_3\text{C}$ for SB10A)
- e* Cold press atmosphere: Air (150 MPa applied) or argon (175 MPa applied).
- f* Elevated temperature press: VHP = vacuum hot press, HIP = hot isostatic press, AHP = argon hot press
- g* Percent of the density of single crystal $\alpha\text{-MoSi}_2$
- h* Vickers hardness numbers
- i* Fracture toughness values
- j* Possible air leakage during VHP as source of SiO_2 (D)
- k* Water washing without annealing is believed to have leached Si from this powder, therefore the compact contained greater silicon deficiency and higher density than other water washed samples containing excessive SiO_2 content.
- l* The graphite sleeve containing the powder broke during consolidation, which prevented good densification, so lower pressure was required for consolidation by AHP
- m* Density determined by metallography

Model predictions for nanocrystalline MoSi_2 are compared with experimentally measured densities in Figure 4.10. A density versus pressure plot is shown for IHP and VHP conditions. Model results for densification during HIP in the form of a density versus temperature map were reported previously [115]. Experimental data from samples that were hot pressed (Table 4.1) are plotted in Figure 4.10. Experimental data on nanocrystalline MoSi_2 from the work of Ref. [116] is also plotted for comparison. In this work nanocrystalline MoSi_2 was synthesized by attrition milling and compaction was achieved by cold isostatic pressing (CIP) followed by HIP. Their samples contained 4.12-6.33 wt% O_2 and 2.12-3.18 wt% N_2 , apart from other trace impurities. It must be realized that both the model predictions as well as experimental density measurements are subject to errors. Model predictions depend on input material property data. Although realistic input data has been used, the predictions are only as good as the values used to generate the diagram [117,118]. Experimental calculations of relative densities suffer from errors due to uncertainties in the intrinsic densities of the samples containing impurities. As previously mentioned, all relative density calculations have been performed on the basis of the density of single crystal pure MoSi_2 . Model results show that in the impure agglomerated powder system, use of low pressures (< 0.5 GPa) and elevated temperatures during pressing results in the nano pores closing first and the large pores requiring about 200°C higher temperature for their elimination, a result similar to that in nanocrystalline Cu. Experimental data on nanocrystalline MoSi_2 indicate similar behavior of pores.

In samples made from powders that were water washed (M-D and M-L), large interconnected pores are evident. The effect of impurity due to pesting (oxide) and the silica layer resulted in poor compaction. In the relatively purer samples (M-E, M-I, M-M to M-T), large pores are absent and high magnification images reveal nano sized pores. These samples were made from powders that were either annealed or alcohol washed to remove salts (Table 4.1). The difference in densification behavior and final pore structures is primarily due to the different nature of agglomerates in the water washed and alcohol washed / annealed powder. The water washed powders consist of "hard" agglomerates and the non-water washed powder consists of "soft" agglomerates. Similar observations of hard and soft agglomerate formation due to different washing medium have been reported [119-123]. Water washed powders usually produced hard agglomerates which on sintering / pressing gave compacts with inhomogeneous densification. Alcohol washed powder produced soft agglomerates which packed uniformly and could be pressed to high density. Shi et al [121] concluded from their work on compaction behavior of ZrO_2 that non agglomerated powder compacts densify much faster than agglomerated powder compacts, partially agglomerated particle systems with relatively small inter-agglomerate pore size need high temperature to remove these pores (presumably due to topological factors), and totally agglomerated powder systems with relatively large inter-agglomerate pores can only develop porous microstructures even at high temperatures.

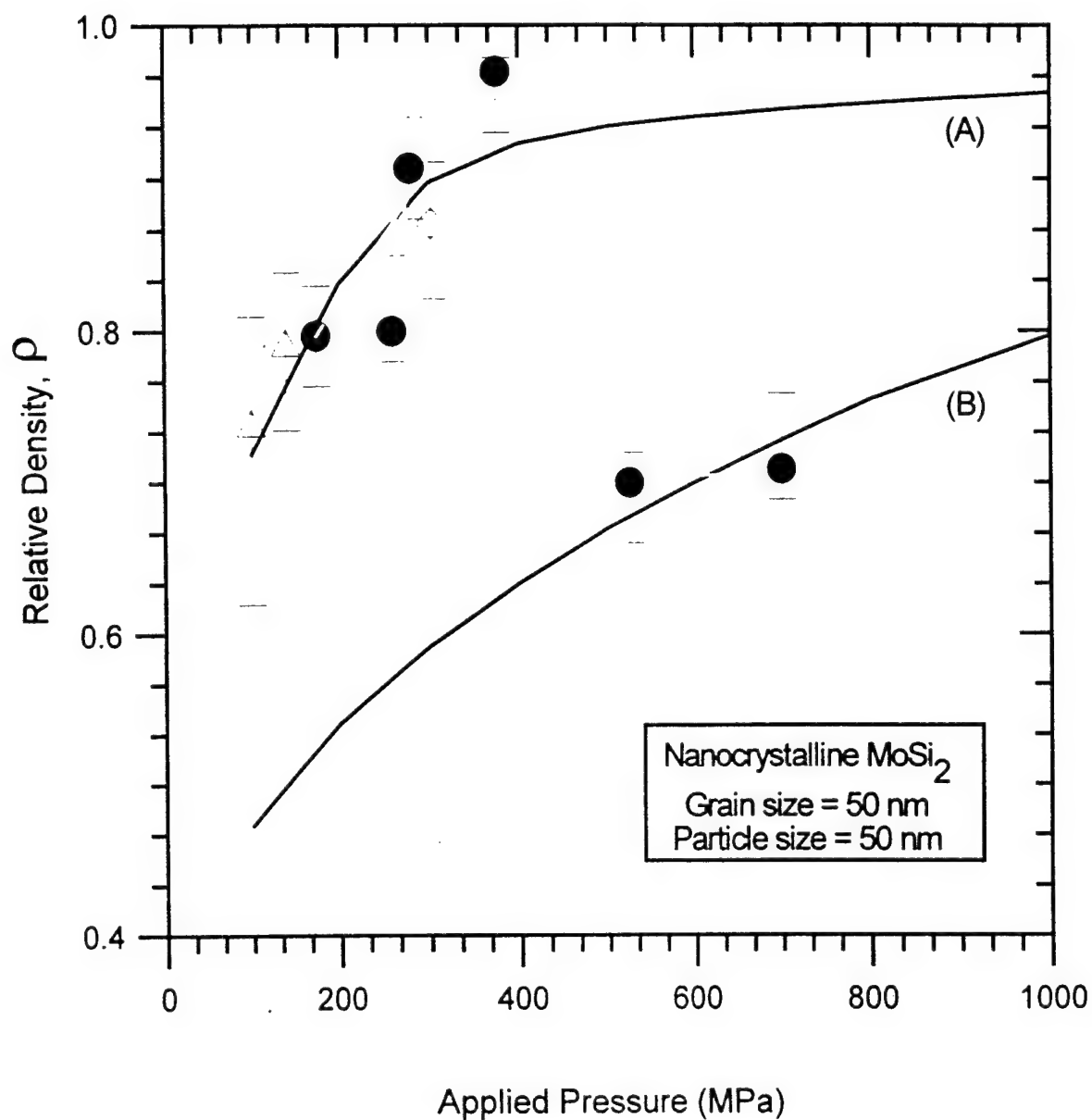


Figure 4.10: Hot pressing diagram for nanocrystalline MoSi_2 . Model predictions are for 50 nm grain size, 50 nm particle size, and 4 hr. A density versus pressure plot is shown for agglomerated powder with trace impurity. Cold pressing pressure is 200 MPa. Cold pressed density is 0.318/0.504 in regions I and II, respectively. Curve (A) is for 1350°C and (B) is for 900°C. Legend for experimental data: ●: M-M and M-N, ○: M-Q through M-T, △: M-A, M-C through M-H, ◇: Data from Ref. [116]. See Ref. [116] and Table 4.1 for details of consolidation conditions for each sample.

Model calculations were performed for the case of elevated temperature, high pressure, for material with low impurity levels (Figure 4.10b). At the initial stage of densification the dominant mechanisms of densification were plastic yielding followed by interparticle and interagglomerate sliding. This is similar to results obtained for the consolidation of nanocrystalline Y_2O_3 - stabilized ZrO_2 during rapid hot pressing (1.6 GPa, 1100 - 1300°C, 10 sec) by Matthews and Pechnick [124]. In their study densification consisted of closing of large pores whereas small pores were largely unaffected and the major mechanism of densification was rearrangement and sliding of grains around large pores. During the final stage, model results indicate that boundary diffusion and power law creep are dominant and were responsible for closure of final nano porosity

Consolidate Characterization:

Solution Based Reaction Products: The pore structure within compacts varied depending on the consolidation procedure. Samples that were consolidated by HP followed by HIP, such as the sample shown in Figure 4.11 contained only fine scale interagglomerate pores of less than 1 μm in diameter (typically 100-300 nm) and interparticle pores of about 30 nm. The pores were not interconnected. Samples that were consolidated only by HP or HIP, contained some much larger interagglomerate pores, but they were still isolated. For powders that were washed with water at some point during processing, porosity was often large and interconnected.

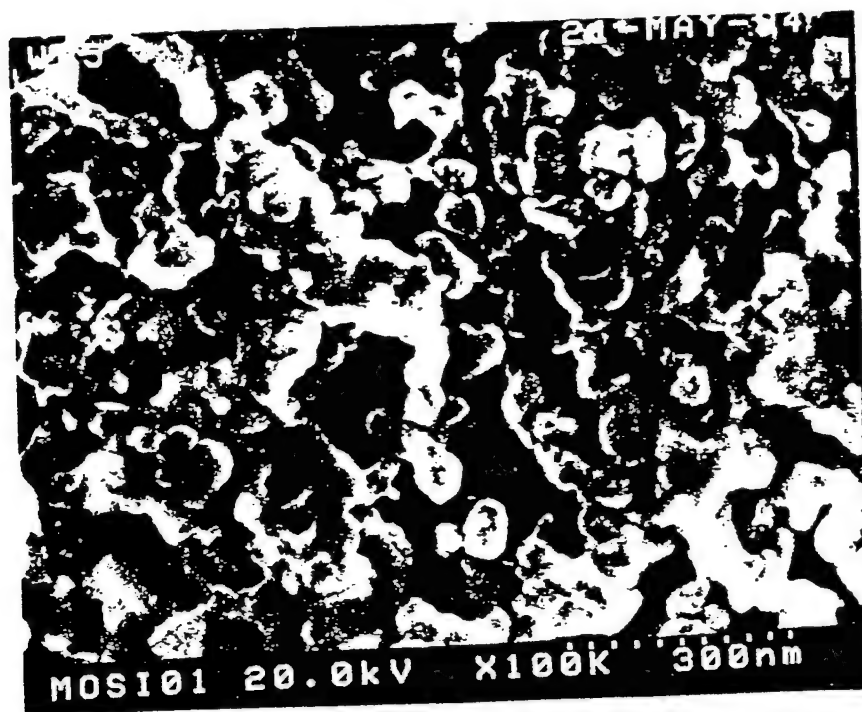
Average grain sizes were less than 100 nm for all compacts derived by solution-based processing. Figure 4.12 shows an SEM image of an etched surface of sample SB4B. The grains were around 50 nm, reasonably consistent with the coherence length of the XRD pattern. This represented more than a doubling of the particle size indicated by XRD for the precursor powder. Other compacts exhibited no growth, while some demonstrated even greater grain growth. Grain size cannot presently be correlated with consolidation parameters because sufficient control of preparative methods had not been established to afford precursor powders of uniform composition and structure, and a systematic investigation of pressing conditions implementing consistent pressure and temperature ramping schedules was not conducted. As would be anticipated, however, the sample consolidated at the highest temperature contained the largest grains. Sample SB11A consolidated by AHP at 1400°C and then HIP at 1500°C possessed grains averaging 95 nm according to XRD. Often samples that were consolidated by HIP following HP possessed larger grains (> 50 nm).

Solid-State Products: According to XRD, all compacts derived from solid-state reaction products consisted of phase pure $MoSi_2$ except those that were pressed at below 1000°C for which the diffusion reaction between molybdenum and silicon was incomplete. Mo_5Si_3 was probably not observed because little oxygen or carbon was available to leach



nMoSi2 30.0kV X2.00K 15.0µm

Figure 4.11 SEM image of a polished surface of compact SB7A showing a low level of very fine scale porosity (<10 vol.%).



4/26/94 WUHP #8



Figure 4.12. SEM images of a polished then etched surface of compact SB4B showing nanoscale grains of around 50 nm.

silicon from MoSi_2 , as air exposure was not allowed, and the powders were not prepared in an environment containing organics. EDS, however, did indicate some O and C impurity in the compacts. This may have arisen from methanol used to wash away LiCl. Also, carbon was probably incorporated by diffusion from the graphite lubricating sleeve used to contain the material during consolidation. Indeed, carbon was more prevalent on surfaces of the pellet that were exposed to the graphite sleeve, and dispersoids of $\text{Mo}_5\text{Si}_3\text{C}$ were observed by SEM. Finally adventitious oxidation is difficult to entirely eliminate.

Solid-state compacts were nanocrystalline but not fully dense. Consolidation by AHP at 1400°C and 375 Mpa, however, did result in densities much greater than 90% of the density of single crystal MoSi_2 and as high as 97.9%. Figure 4.13 shows an SEM image of a polished surface of sample SS2B illustrating the very low level of fine scale porosity in these compacts. This compact clearly possessed greater density than those of the solution-based samples examined, a consequence of the higher consolidation pressures and temperatures. Average grain sizes for these compacts were 50 nm according to XRD despite the high consolidation temperatures. This was reasonably consistent with SEM images, which showed that many grains were less than 50 nm while some approached or slightly exceeded 100 nm (Figure 4.14).

Samples consolidated at slightly lower pressure and/or temperature exhibited greatly diminished densities and larger grains by XRD (>80 nm). Samples SS3A consolidated at 1300°C and 175 Mpa possessed a density of only 79.7% and contained large interagglomerate pores. The lower pressure is believed to account for this result. When high pressures are applied, interagglomerate pores are closed by plastic deformation rapidly, hence obviating diffusional growth as pore closure mechanism. When the lower pressure was used, the large pores were not closed and diffusional sintering was enabled, hence resulting in some grain growth.

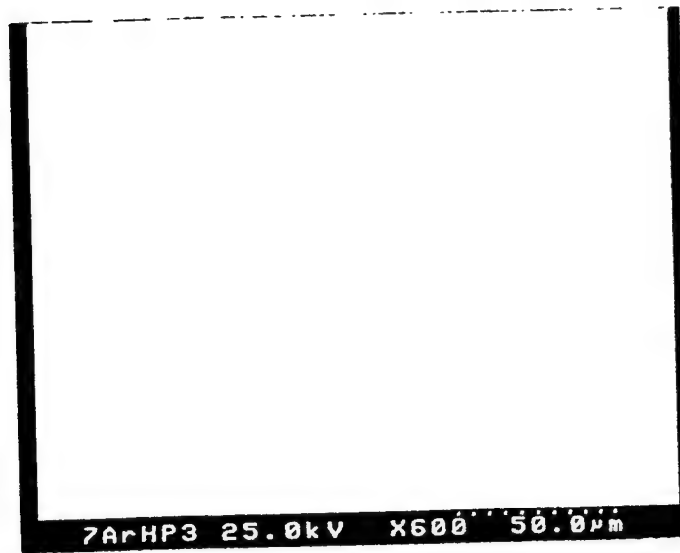


Figure 4.13. SEM image of a polished surface of compact SS2B showing a very low level of porosity.

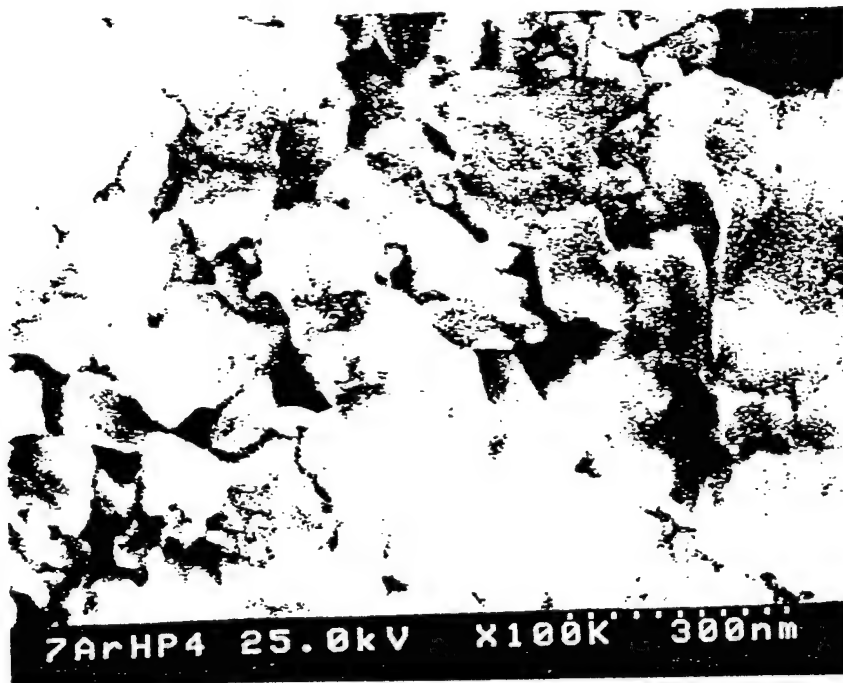


Figure 4.14. SEM image of a polished and etched surface of compact SS2B showing grains of less than 100 nm.

5. MECHANICAL PROPERTIES OF NANOCRYSTALLINE MoSi₂

Microhardness, indentation fracture toughness, three point bend strength, room and high temperature compression strengths were measured on the MoSi₂ and the composite samples.

Hardness:

Hardness values were established for most of the compacts prepared from both solution-based and solid-state reaction products. The results for the solid-state products should more accurately reflect the hardness enhancement due strictly to reducing MoSi₂ grain size into the nanometer regime because they possessed low porosity, which would tend to artificially lower hardness values, and they possessed little content. The hardness of the most dense compact was 16.3 Gpa, which constitutes a 75% increase over the conventional, microcrystalline MoSi₂ hardness of 9.3 Gpa [129]. The less dense samples exhibited lower hardness values down to 12.5 Gpa; the overall average was 14.6 Gpa.

Compacts derived from solution-based powders theoretically should possess higher hardness values than the solid-state compacts because the powders contained 20 vol.% or more of SiC, which has much higher hardness (25 GPa [129]) than does MoSi₂. A conventional MoSi₂-20 Vol.% SiC composite has been shown to possess a hardness of 14 Gpa. For the nanocrystalline composite, then a value of more than 20 Gpa could be anticipated if the hardness enhancement due to grain size scales proportionately with the monolithic case. This was not observed, however, because these powders were exposed to air and therefore also contained SiO₂, which is a much softer material than MoSi₂ and probably compensated for the SiC. Most of the solution-based compacts actually exhibited hardness that was less than the hardness values for the conventional composite and for the solid-state compacts and higher than conventional MoSi₂ monoliths. The values of these compacts ranged from 10.9 to 16.6 Gpa with an average of only 13.0 Gpa. Surprisingly, the compact possessing the highest hardness was derived from a powder that was washed with water and contained a very large quantity of SiO₂ as evidenced by substantial SiO₂ reflections by XRD. This indicates that SiO₂ alone does not account for the low hardness of the samples. Much higher porosity compared to the solid-state products, and other structural features are of importance. . A hardness value of 14.1 Gpa was observed for nanocrystalline MoSi₂ containing 35 volume % SiC whiskers. This value is considerably lower than that expected from rule of mixtures.

Strength:

Compression tests at 25 °C and 1100 °C were conducted on compacts prepared from solution-based MoSi₂ particles and compacts containing SiC whiskers. Ultimate tensile strength and total plastic strain obtained from these tests are listed in table 5.1 . Results from microcrystalline samples are also given for comparison. The flow curves are shown in Figure 5.1

Table 5.1. Compression Strength and Plastic Strain of Nanocrystalline and Microcrystalline Molybdenum Silicide-Based Materials.

	σ_c at RT (MPa)	Plastic Strain at RT (%)	σ_c at 1100°C (MPa)	Plastic Strain at 1100°C (%)
n-MoSi ₂ (SB7A' from Table 6.1)	2875	0	227	25
m-MoSi ₂ ^{1,10}	1503	0	827	2-3
m-MoSi ₂ ¹⁸	1544	0	NA	NA
m-MoSi ₂ /30%SiC _p ¹⁸	1760	< 0.1	NA	NA
n-Mo ₅ Si ₃ C/35%SiC _w (SB10A from Table 6.1)	636	0	381 310	1-2 1-2

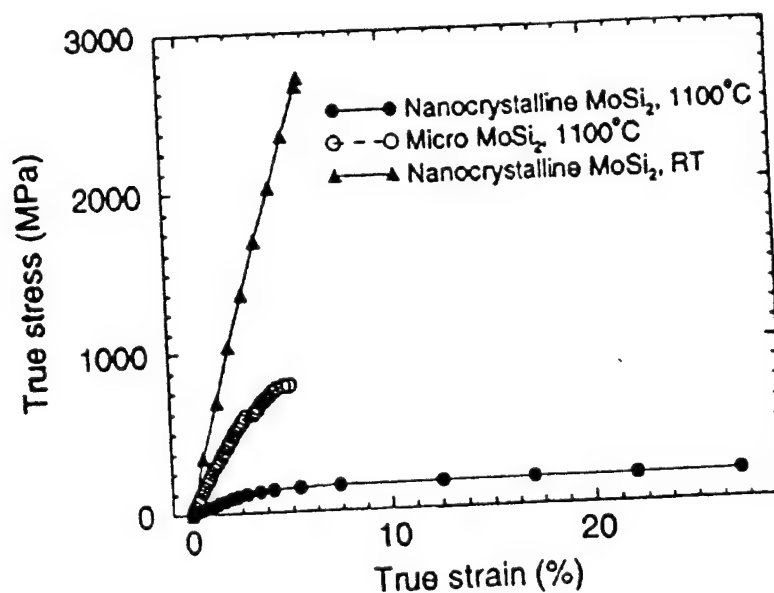


Figure 5.1 Flow curves for nanocrystalline MoSi₂ (SB7A') and microcrystalline MoSi₂.

At room temperature the solution-based, nanocrystalline product (SB7a') exhibited a substantial improvement in strength over conventional, microcrystalline MoSi₂. The ultimate tensile strength for the nanocrystalline sample was 2875 Mpa. As there was no plastic deformation before failure (Figure 5.1), this also constituted the yield stress for this compact. This stress is 85% greater than the ultimate stress for coarse-grained MoSi₂ and 65% greater than for a MoSi₂/SiC composite. This latter comparison is made because solution-based products may have contained more than 20 vol.% SiC. The strength of the nanocrystalline compact was obviously limited by fracture, as the compact failed without yielding. Because premature failure would arise due to porosity, it may be possible to improve the strength of the nanocrystalline material further with better densification. This should be feasible considering that this sample was consolidated at relatively low pressure and temperature compared to some of the other powders (see table 5.1). The strength improvement observed for this sample is greater than that projected from hardness enhancement of 50% over microcrystalline MoSi₂.

At 100⁰C, a degradation rather than improvement in strength was observed for nanocrystalline MoSi₂. The ultimate strength of the nanocrystalline compact was only 227 Mpa, while a microcrystalline compact had a strength of 827 Mpa. The plastic strains in nanocrystalline and microcrystalline compacts were 25% and 3 % respectively. The very large degree of plastic yielding for the nanocrystalline sample indicates that the brittle-to-ductile transition temperature for this material was less than 1100⁰C. Plastic deformation most likely proceeded by grain boundary sliding, which was probably accelerated by softening of the considerable quantity of grain-boundary silica (melting point 1610⁰C) that was introduced into the material by air exposure of the powder prior to consolidation. A nanocrystalline sample possessing little silica, such as perhaps a solid state product, is therefore expected to exhibit much better high-temperature strength.

The compact that contained SiC whiskers exhibited low strengths at both room temperature (636 Mpa) and at 1100⁰C (381 Mpa). At room temperature the specimen failed without plastic yielding, and at high temperature the specimen exhibited only 2% ductility before fracture. The lower ductility of the composite at high temperature can be attributed to the SiC whisker reinforcements inhibiting creep by grain-boundary sliding or dislocation glide and climb. The room temperature strength was limited by fracture as for the other nanocrystalline sample. This sample, however, contained larger scale porosity (as all water washed powders did after consolidation), which could have caused premature fracture under the much lower level of stress that was observed. The low strength is also in part due to a much larger SiO₂ content in this sample, which was evident by substantial SiO₂ reflections present in the XRD pattern of the compact.

Fracture Toughness:

Enhanced toughness was evidenced for the nanocrystalline compacts of this study in that higher indentation loads (1 kg vs. 500 g) were required in many instances to induce cracking than was necessary for microcrystalline MoSi₂ using the same indenter.

Further, whereas the cracks in microstalline samples were irregular, those in the nanocrystalline products extended linearly from indent vertices (Figure 5.3). Fracture toughness values were calculated from these cracks for several of the solution-based and solid-state reaction derived compacts. Modest improvements over the conventional value of $3.0 \text{ Mpa.m}^{1/2}$ were determined. Values for solution-based compacts ranged from 3.8 to $5.6 \text{ Mpa.m}^{1/2}$. The values for the solid-state compacts were lower, having an average of $3.8 \text{ Mpa.m}^{1/2}$ and a range of only 3.2-4.8 $\text{Mpa.m}^{1/2}$. These values were calculated assuming the elastic modulus of the compacts was equivalent to that for single crystal MoSi_2 (440 GPa)[132].

The value of 440 GPa for modulus may have been an underestimate, as Mahmood and Chumbley have established a value of elastic modulus of 541 GPa for nanocrystalline MoSi_2 prepared by high-energy milling [133]. As fracture toughness is directly related to modulus (as a square root term) by the Antis equation [134], the toughness may actually have been greater than was calculated. Using 541 GPa in the calculation resulted in the fracture toughness values of $5.0 \text{ Mpa.m}^{1/2}$ for solution-based compacts and $4.2 \text{ Mpa.m}^{1/2}$ for solid-state compacts. It is not likely, however, that both the solution-based and solid-state compacts possess the same modulus. A somewhat higher level of porosity and considerable SiO_2 content should lower the elastic modulus of the solution-based product, which may equalize the toughness values calculated for the compacts obtained from both preparative methods. From these results, it is clear that the toughness values of 15-20 $\text{Mpa.m}^{1/2}$ required for implementation of MoSi_2 based materials in structural applications [135] were not achieved. It is noteworthy, however, that despite significant porosity in the compact, some enhancement in toughness was observed. Improved nanocrystalline particles, complete densification may result in higher fracture toughness values. The compact prepared in this study with SiC whisker was determined to have a toughness of $9.1 \text{ Mpa.m}^{1/2}$ which is the highest value reported to date for molybdenum silicide-based material possessing discontinuous brittle reinforcements.

The mechanical property data of our study compare favorably with the data obtained with mechanically milled MoSi_2 reported by Mahmood and Chumbley[133]. Compacts described in reference 133 have porosities of > 8.7%. The maximum hardness reported in [133] is 10.43 GPa compared to a minimum value of 10.9 GPa in our study. The toughness values obtained by Mahmood and Chumbley are generally greater than 5 $\text{Mpa.m}^{1/2}$ and as high as $6.91 \text{ MPa.m}^{1/2}$.

6 CONCLUSIONS

Two successful solution phase synthesis methods were developed for the preparation of nanocrystalline (<100 nm size) MoSi_2

Solution phase reductions of molybdenum and silicon chlorides followed by annealing under vacuum to remove byproduct salts and effect crystallization affords a convenient method for obtaining large quantities of nanocrystalline MoSi_2 (20-50 nm). The products, however, are not monolithic, as they contain substantial quantities of SiC, which may prove advantageous for practical applications because this is a valuable reinforcement phase for conventional MoSi_2 . Good control over the quantity of SiC in the reaction products, or over the size of MoSi_2 nanoparticles has yet to be established

Conducting metallothermic reductions in the presence of a large excess of reducing agent that can serve as both a heat sink and a solvent for silicon leads to submicron MoSi_2 crystallites encroaching on the nanometer regime.. It is believed that grain-size refinement would be possible, and nanoparticles free of carbon would be obtained. The chief limitation to this strategy is the impracticality of working with such large quantities of reducing metals that would require subsequent removal.

Heating a mixture of MoCl_3 and Si in a furnace at 500°C results in the complete formation in only seconds of MoSi_2 possessing average crystallite sizes slightly larger than 100 nm. Byproducts SiCl_4 is volatilized during the reaction, so subsequent isolation of product is not required. Adding a diluent to the reaction allows for the preparation of nanocrystalline product. The diluents that were used were LiCl and ZnCl_2 . The latter moderated the reaction much more efficiently. Both can be readily sublimed or washed away, and therefore provide little added complication to the

A theoretical model for nanoparticle densification by uniaxial and/or hot isostatic pressing was developed. The model predicts the dominant densification mechanisms during nanoparticle densification under a specific combination of applied pressure, temperature, and time; predicts grain growth behavior during compaction; and provides guidelines for the optimal consolidation parameters for a general nanoparticle system this model represents the first rigorous and comprehensive attempt at developing a micromechanism based model for nanoparticle consolidation.

Hot pressing diagrams in the form of relative density versus time and pressure were constructed for nanocrystalline MoSi_2 . Model predictions were validated by density measurements and microstructural determination of pore volume fractions of compacts of nanocrystalline copper and MoSi_2 produced from solution-phase synthesized nanoparticles. The model predictions agreed well with experimental results, not only in the values of the final densities but also in microstructural features like pore structure and

grain size. The model predictions agreed well with results of consolidation experiments in literature for a wide range of consolidation parameters.

Near theoretical densities could not be obtained in MoSi_2 . High density MoSi_2 samples exhibit microcracking. Higher temperatures, better control of impurities, and/or the use of dopants is necessary to consolidate MoSi_2 nanoparticles into quality products.

Nanocrystalline MoSi_2 and MoSi_2/SiC composites exhibit significantly higher (50-75%) hardness and compression strength, over their conventional counterparts at room temperature.. However, at high temperatures (1100 oC ductilities are higher and strengths are lower in the nanocrystalline samples than in microsrystalline MoSi_2 samples. Modest increases in room temperature fracture toughness of 15-30% were observed in nanocrystalline samples.

REFERENCES

1. R. P. Andres, R. S. Averback, W. L. Brown, L. E. Brus, W. A. Goddard III, A. Kaldor, S. G. Louie, M. Moscovits, P. S. Peercy, S. J. Riley, R. W. Siegel, F. Spaapen, and Y. Wang, *J. Mater. Res.*, **4**[3], 704-736 (1989).
2. R. A. Andrievski, *J. Mater. Res.*, **29**, 614-631 (1994).
3. H. Gleiter, *Prog. Mater. Sci.*, **33**, 223-315 (1989).
4. C. Suryanarayana and F. H. Froes, *Metall. Trans. A*, **23A**, 1071-1081 (1992)
5. A.K. Vasudevan and J.J. Petrovic, *Mater. Sci. Eng.*, A 1992, 155, 1.
6. Y. Umakoshi, T. Sakagami, T. Hirano, and T. Yamane, *Acta Metall. Mater.* 1990, 38, 909.
7. M.J. Maloney, and D. Shah, in *Physical Metallurgy and Processing of Intermetallic Compounds*: N.S. Stoloff and V.K. Sikka, Eds., Chapman & Hall: New York, 1996; Ch. 11.
8. L. Xiao, Y.S. Kim and R. Abbaschian, *Mater. Res. Soc. Symp. Proc.* 1990, 194, 399
9. T.C. Lu, A.G. Evans, R.J. Hecht and R. Mehrabian, *Acta Metall. Mater.* 1991, 12, 1671
10. A.K. Vasudevan, J.J. Petrovic, and K. Sadananda, 12th Riso Proc. 1991, 707
11. D.P. Pope and R. Doralia, *MRS Bulletin*, 1996, 21(5), 30
12. J.J. Petrovic, R.E. Honnell, T.E. Mitchell, T.E. Wade, and K.J. McClellan, *Ceramic Eng. Sci. Proc.* 1991, 12, 1633
13. R.W. Siegel, *MRS Bulletin*, 1990, 15 (10), 60.
14. J.L. Garin and R.L. Mannheim, *Powder Diffr.* 1993, 8, 65
15. J.L. Crane, Ph.D. Dissertation, Washington University, St. Louis, Aug. 1994.
16. J.L. Crane, Washington University, St. Louis, MO. Unpublished results.
17. J.J. Ritter, *Adv. Ceram.* 1987, 21, 21
18. R.A. Schunn in *Transition Metal Hydrides*: E.L. Muetterties, Ed., Marcel Dekker, New York, 1971, Ch. 5
19. D. Zeng and M.J. Hampden-Smith, *Chem. Mater.* 1993, 5, 681
20. D. Zeng, M.J. Hampden-Smith, and L.M. Wang, *Mater. Res. Soc. Symp. Proc.*, 1994, 322, 127 (Note: the phases were incorrectly identified as MoSi₂, SiC, and an unknown phase in this publication)
21. F.J.J. van Loo, F.S. Smet, G.D. Rieck, and G. Verspui, *High Temp.-High Pressures* 1982, 14, 25
22. D.H. Killeffer and A. Linz, *Molybdenum Compounds*; Interscience: New York, 1952: p. 11
23. R. Abramovici and G.T. Hida U.S. Patent 5011 800, 1991.
24. L. Brewer and R.H. Lamoreaux, in *Molybdenum: Physico-Chemical Properties of its Compounds and Alloys*: L. Brewer, Ed: International Atomic Energy Agency: Vienna, 1980, p. 271.
25. V.K. Lamer and R.H. Dinegar, *J. Am. Chem. Soc.* 1950, 72, 4847
26. A.S. Bereznoi, *Silicon and its Binary Systems*; Consultants Bureau: New York, 1960: p. 57.
27. Y.L. Jeng and E.J. Lavernia, *J. Mater. Sci.* 1954, 29, 2557

28. R.M. Jacubinas and R.B. Kaner, *Mat. Res. Soc. Symp. Proc.*, 1994, 322, 133
29. D. Zeng, M.J. Hampden-Smith, and L.M. Wang, *J. Mater. Chem.*, 1993, 3, 777
30. S.C. Deevi, *Mater. Sci. Eng., A*, 1992, 149, 241
31. Z.A. Munir, *Ceram. Bull.* 1988, 67 (2), 342
32. S. Zhang and Z.A. Munir, *J. Mater. Sci.*, 1991, 26, 3685
33. S. Inoue, N. Toyokura, T. Nakamura, M. Maeda, and M. Takagi, *J. Electrochem. Soc.*, 1983, 130, 1603
34. W.J. Boettinger, J.H. Perepezko, and P.S. Frankwicz, *Mater. Sci. Eng., A*, 1992, 155,
35. Y. Umakoshi, T. Sakagami, T. Hirano, and I. Yamane, *Acta Metall. Mater.* 1990, 38,
36. P. G. Sanders, J. A. Eastman, and J. R. Weertman, in *Processing and properties of nanocrystalline materials*, TMS Symp. Proc., vol. 379, Warrendale, PA (1996).
37. D-J. Chen and M. J. Mayo, *Nanostr. Mater.*, 2, 469-478 (1993).
38. G. Skandan, H. Hahn, B. H. Kear, M. Roddy, and W. R. Cannon, *Mater. Lett.*, 20, 305-309 (1994).
39. G. Skandan, *Nanostr. Mater.*, 5 [2], 111-126 (1995).
40. K-N. P. Kumar, K. Keizer, A. J. Burggraaf, T. Okubo, H. Nagamoto, and S. Morooka, *Nature*, 358, 48-51 (1992).
41. J. Hebeisen, P. Tylus, D. Zick, D. K. Mukhopadhyay, K. Brand, C. Suryanarayana, and F. H. Froes, *Metals and Materials*, 2 [2], 71-74 (1996).
42. H. F. Fischmeister and E. Arzt, *Powder Metall.*, 26 [2], 82-88 (1983).
43. A. S. Helle, K. E. Easterling, and M. F. Ashby, *Acta Metall.*, 33, 2163 (1985).
44. R. J. Schaefer, *Intl. J. Powder Metall.*, 28 [2], 161-173 (1992).
45. E. Y. Gutmanas, L. I. Trusov, and I. Gotman, *Nanostr. Mater.*, 4 [8], 893-901 (1994).
46. M. G. McKimpson, *Proc. ASME Conference*, Baltimore, MD, June 1996.
47. V. G. Gryaznov and L. I. Trusov, *Prog. Mater. Sci.*, 37, 289-401 (1993).
48. W. Romanowski, *Highly Dispersed Metals*, Wiley (1987).
49. Y. I. Petrov, *Clusters and Small Particles*, Nauka (1986).
50. M. J. Mayo, In *Mechanical properties and deformation behavior of materials having ultrafine microstructures*, M. Nastasi et al. (Eds.) Kluwer, Dordrecht, The Netherlands, p. 361 (1993).
51. W. H. Rhodes, *J. Amer. Ceram. Soc.*, 64 [1], 19-22 (1981).
52. P. K. Higgins and Z. A. Munir, *Powder Metall.*, 4, 188-194 (1978).
53. R. A. Andrieviski, *Intl. J. Powder Metall.*, 30 [1], 59-66 (1994).
54. J. Blendal, NIST, Gaithersburg, MD, in *Abstracts of the Penn State Workshop of Small Particle Sintering*, R. M. German (Chair), State College, PA, November 1993.
55. Y. Sakka, *J. Less-Common Metals*, 168, 277-287 (1991).
56. Y. Sakka and T. Uchikoshi, *Powder Metall.*, 36 [3], 179-186 (1993).
57. Y. Sakka, T. Uchikoshi, and E. Ozawa, *J. Mater. Sci.*, 28, 203-217 (1993).
58. G. E. Fougere, J. R. Weertman, and R. W. Siegel, *Nanostr. Mater.*, 5, 127 (1995).
59. Y. Sakka, *J. Mater. Sci. Lett.*, 10, 426-429 (1991).
60. O. Dominguez, M. Phillipot, and J. Bigot, *Scripta Metall. Mater.*, 32 [1], 13-17 (1995).
61. B. Gunther, A. Baalman, and H. Weiss, In *Mater. Res. Soc. Symp. Proc.*, 195, 611-615 (1990).

62. G. W. Nieman, J. R. Weertman, and R. W. Siegel, *J. Mater. Res.*, **6** [5], 1012-1027 (1991).
63. D. L. Wang, Q. P. Kong, and J. P. Shui, *Scripta Metall.*, **31** [1], 47-51 (1994).
64. A. H. King, *Scripta Metall.*, **31** [11], 1493-1494 (1994).
65. Y. H. Zhou, M. Harmelin, and J. Bigot, *Scripta Metall.*, **23**, 1391-1396 (1989).
66. H. Y. Lee, W. Riehemann, B. L. Mordike, *J. European Ceram. Soc.*, **10**, 245-253 (1992).
67. R. A. Andrievski and S. E. Zeer, *Science of Sintering*, **19** [1], 11 (1987).
68. S. H. Risbud, C-H. Shan, and A. K. Mukherjee, *J. Mater. Res.*, **10** [2], 237-239 (1995).
69. S-C. Liao, K. D. Pae, and M. J. Mayo, *Mater. Sci. Engg A*, **A204**, 152-159 (1995).
70. B. R. Murphy and T. H. Courtney, *Nanostr. Mater.*, **4** [4], 365-369 (1994).
71. Y. C. Zhou and M. N. Rahaman, *J. Mater. Res.*, **8** [7], 1680-1686 (1993).
72. R. S. Averback, H. Hahn, H. J. Hofler, J. L. Logas, and T. C. Shen, In *Mater. Res. Soc. Symp. Proc.*, **153**, 3 (1989).
73. M. D. Matthews and A. Pechnik, *J. Amer. Ceram. Soc.*, **74** [7], 1547-1553 (1991).
74. S. Komarneni, E. Fregeay, E. Brewal, and R. Roy, *J. Amer. Ceram. Soc.*, **71** [1], C26-C28 (1988).
75. M. J. Readey, R. R. Lee, Halloran J. W., and A. H. Heuer, *J. Amer. Ceram. Soc.*, **73** [6], 1499-1503 (1990).
76. G. Skandan, H. Hahn, and J. C. Parker, *Scripta Metall.*, **25**, 2389-2393 (1991).
77. M. M. R. Boutz, L. Winnubust, and A. J. Burggraaf, *J. Amer. Ceram. Soc.*, **78** [1], 121-128 (1995).
78. P. Lu, S. C. Danforth, and W. T. Symons, *J. Mater. Sci.*, **28**, 4217-4222 (1993).
79. D. C. Hague and M. J. Mayo, *Mater. Sci. Engg. A*, **A 204**, 83-89 (1995).
80. A. J. Allen, S. Krueger, G. Skandan, G. G. Long, H. Hahn, H. M. Kerch, J. C. Parker, and M. N. Ali, *J. Amer. Ceram. Soc.*, **79** [5], 1201 (1996).
81. R. Vaben and D. Stover, *Powder Tech.*, **72**, 223-226 (1992).
82. I. Shapiro and M. Kolthoff, *J. Phys. Colloid Chem.*, **51**, 483-493 (1947).
83. H. Zhu and R. S. Averback, *Mater. Sci. Engg. A*, **A 204**, 96-100 (1995).
84. D. S. Wilkinson, Ph. D. Thesis, Cambridge University (1978).
85. R. Suryanarayanan, T. J. Trentler, N. V. Gunda, W. E. Buhro, and S. M. L. Sastry, *Acta Mater.*, **xx**, xx (199x).
86. H. N. G. Wadley, R. J. Schaefer, A. H. Kahn, M. F. Ashby, R. B. Clough, Y. Geffen, and J. J. Wlassich, *Acta Metall.*, **39** [5], 979-986 (1991).
87. R. Suryanarayanan, S. M. L. Sastry, and K. L. Jerina, *Acta Metall.*, **42** [11], 3741-3750 (1994).
88. J. Besson and M. Abouaf, *J. Amer. Ceram. Soc.*, **75** [8], 2165-2172 (1992).
89. J. Bernardini, P. Gas, E. D. Hondros, and M. P. Seah, *Proc. R. Soc. Lond.*, **A 379**, 159-178 (1982).
90. A. D. LeClaire, *Thin Solid Films*, **25**, 1-14 (1975).
91. E. D. Hondros and M. P. Seah, *Intl. Metals Rev.*, December, 262-301 (1977).
92. E. D. Hondros and M. P. Seah, In *Physical Metallurgy*, R. W. Cahn and P. Haasen (eds.), Elsevier (1993).
93. J. L. Hertzberg and G. S. Was, *Scripta Metall. Mater.*, **32** [8], 1193-1199 (1995).

94. J. L. Bocquet, G. Brebect, and Y. Limoge, In *Physical Metallurgy*, R. W. Cahn and P. Haasen (eds.), Elsevier (1993).
95. K. L. Johnson, K. Kendall, and A. D. Roberts, *Proc. R. Soc. Lond.*, **A 324**, 301-313 (1971).
96. K. E. Easterling and A. R. Tholen, *Powder Metall.*, **16** [31], 112-118 (1973).
97. Y. E. Geguzin, *Sov. Phys. Sol. State*, **17** [7], 1277-1279 (1976).
98. I. G. Crosland and R. B. Jones, *Metal Sci.*, November, 504-508 (1977).
99. M. A. Morris and J. C. Joye, *Acta Metall. Mater.*, **43** [1], 69-81 (1995).
100. W. J. Clegg and J. W. Martin, *Metal Sci.*, **16**, 65-72 (1982).
101. N. Hansen, *Metall. Trans. A*, **16A**, 2169 (1985).
102. K. T. Aust, *Canad. Metall. Quart.*, **33**, 265-274 (1994).
103. F. F. Lange, *J. Amer. Ceram. Soc.*, **67** [2], 83-89 (1984).
104. M. J. Mayo and D. J. Chen, In *Nanostructured materials: Synthesis, properties, and uses*, A. S. Edelstien and R. C. Cammarata (eds.), Institute of Physics, Bristol (1994).
105. A. G. Evans and C. H. Hsueh, *J. Amer. Ceram. Soc.*, **69** [6], 444-448 (1986).
106. E. B. Slamovich and F. F. Lange, *J. Amer. Ceram. Soc.*, **76** [6], 1584-1590 (1993).
107. F. F. Lange, *J. De Phys. Coll.*, **47**, Suppl. 2, C1-205 (1986).
108. M. J. Mayo, D. C. Hague, and D. J. Chen, *Mater. Sci. Engg. A*, **A166**, 145-159 (1993).
109. F. F. Lange and B. J. Kellet, *J. Amer. Ceram. Soc.*, **72** [5], 735-741 (1989).
110. A. Kumpmann, B. Gunther, and H. D. Kunze, *Mater. Sci. Engg. A*, **A168**, 165-169 (1993).
111. B. Gunther, A. Kumpmann, and H. D. Kunze, *Scripta Metall.*, **27**, 833-838 (1992).
112. S. C. Mehta, D. A. Smith, and U. Erb, *Mater. Sci. Engg. A*, **A 204**, 227-232 (1995).
113. R. Suryanarayanan, D. Sc. Dissertation, Washington University, St. Louis (1996).
114. R. Raj, *J. Amer. Ceram. Soc.*, **70** [9], C210-C211 (1987)
115. R. Suryanarayanan, S. M. L. Sastry, K. L. Jerina, T. J. Trentler, B. E. Waller, and W. E. Buhro, in *Synthesis and Processing of Nanocrystalline Materials*, Proc. TMS Annual Meeting, Anaheim, CA, February 1996
116. M. S. Haji-Mahmood and L. S. Chumbley, *NanoStructured Mater.*, **7** [1/2], 95-112 (1996).
117. A. S. Helle, K. E. Easterling, and M. F. Ashby, *Acta Metall.*, **33**, 2163 (1985).
118. R. Suryanarayanan, S. M. L. Sastry, and K. L. Jerina, *Scripta Metall.*, **28** [7], 797-802 (1993).
119. S. Komarneni, E. Fregeau, E. Breval, and R. Roy, *J. Amer. Ceram. Soc.*, **71** [1], C26-C28 (1988).
120. M. J. Readey, R. R. Lee, Halloran J. W., and A. H. Heuer, *J. Amer. Ceram. Soc.*, **73** [6], 1499-1503 (1990).
121. J. L. Shi, J. H. Gao, Z. X. Lin, and D. S. Yan, *J. Mater. Sci.*, **28** [2], 342-348 (1993).
122. K. Kwon, C. S. Nordahl, and G. L. Messing, Proc. ASME Conference, Baltimore, MD, June 1996.
123. B. L. Armstrong, Proc. ASME Conference, Baltimore, MD, June 1996.
124. H. N. G. Wadley, R. J. Schaefer, A. H. Kahn, M. F. Ashby, R. B. Clough, Y. Geffen, and J. J. Wlassich, *Acta Metall.*, **39** [5], 979-986 (1991).

125. K. Kendall, N. McNalford, and J. D. Birchall, *Proc. R. Soc. Lond. A*, **412**, 269-283 (1987).
126. C. Frey, D. Sc. Dissertation, Washington University, St. Louis, MO 63130 (1995).
127. H. J. Frost and M. F. Ashby, *Deformation Mechanism Maps*, Pergamon (1982).
128. *Handbook of Chemistry and Physics*, D. R. Lide (ed.), 1996)

APPENDIX A

Material property data

It should be noted that, as far as possible, standard accepted values of material property data have been used. However, since the model requires several other parameters that are not established for the material, estimation is unavoidable. When the property is not known, reasonable estimate of the property is given..

A.1. A note about the power law creep equation:

The power law creep equation used by Ashby et al [117] was later replaced by Wadley et al [124] so that the Dorn's constant, which is not reliably known, is replaced by a reference stress for power law creep. Unfortunately, as shown previously [118], this change was also not free of error. In the present study, the usual power law creep equation

$$\dot{\varepsilon} = A_{Dom} \sigma^n \exp\left\{\frac{-Q_{PLC}}{RT}\right\} \quad (A1)$$

was used. This equation was preferred over the ones previously used for mainly two reasons. (1) Most experimental data is available and fitted to this form of the equation. (2) It does not predict very high creep rates when the temperature of consolidation exceeds the arbitrary $T_m/2$ used by Wadley et al [124]. The creep diffusivity as a function of temperature is then given as:

$$D_{PLC}(T) = A_{Dom} \exp\left\{\frac{-Q_{PLC}}{RT}\right\} \quad (A2)$$

For low temperature power law creep, where creep is core diffusion controlled, the value of exponent used was $n + 2$ instead of n [124].

A.2. A note about estimation of yield strengths:

The yield strength of the nanoparticle is approximated as: (a) $G(T)/20$, where G is the shear modulus, which is approximately the strength of a crystal with a very small dislocation density, or (b) by the Hall-Petch relationship using conventional Hall-Petch factors. The yield strength of the agglomerate can be estimated by the analysis of Kendall et al [125]. Using the results of Kendall et al [125] it can be derived that the stress required to separate two spherical particles of the same size is:

$$\sigma_{break} = 6 \left(\frac{\Gamma}{d} \right)^{1/3} \left\{ \frac{E}{4.5\pi(1-\nu^2)} \right\}^{2/3} \quad (A3)$$

where Γ is the interfacial energy of the spheres, d is the diameter of the particles, and ν is the Poisson's ratio. The above expression is for the local pressure at the contact spots for two particles, and for an agglomerate containing many particles, the average pressure will depend on surface forces due to other particles and the porosity in the agglomerate. For a particle assembly with nanocrystalline particle size, the stress to collapse the agglomerate can be as high as 0.5 - 1 GPa [125]. As an example, Figure A.1 shows the highly agglomerated nanoparticle system with particle sizes in the < 25 nm range. In this case, the stress required to break the agglomerates can be substantially high.

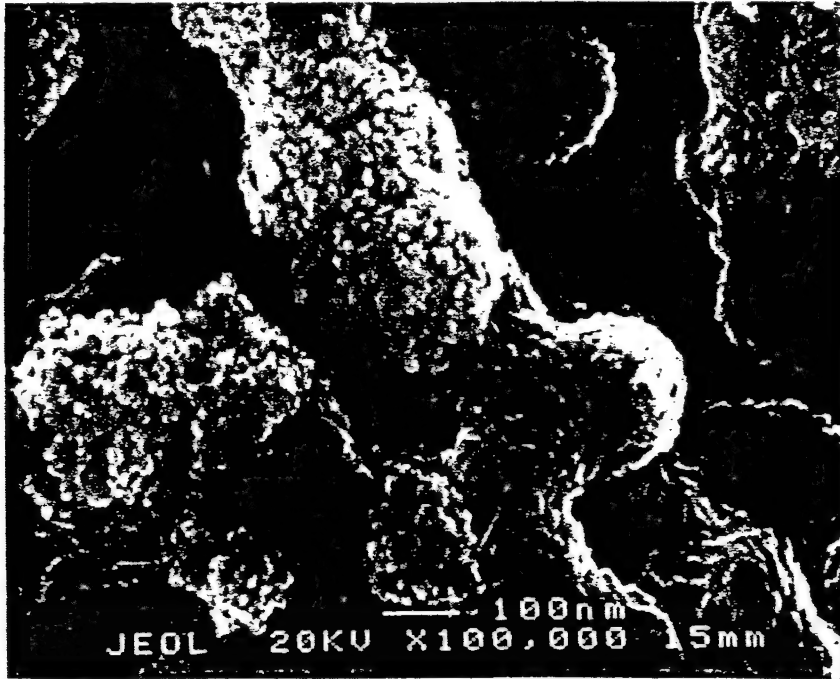


Fig. A.1: TEM micrograph of nanocrystalline TiB_2 particles exhibiting highly agglomerated structure. The stress required to break the interparticle bonds is predicted to be very high due to fine size of particles (Kendall et al, 1987 [125]). Re-printed with permission of author (C. Frey, 1995 [126]).

A.4. Material data for Molybdenum disilicide:

Most data are from Ref. [127]. Atomic radii of elements and molecules are from standard handbooks [128]. Other parameters are estimated as in the case of nanocrystalline copper.

Table A.1: Material property data used to generate densification maps.

Material Property		MoSi ₂
Atomic volume (m ³), Ω		8.06×10^{-29}
Free surface energy (kJ/mol), γ_{surf}		1.0
Grain boundary energy (kJ/mol) ¹ , γ_{gb}		0.3
Burgers vector (m), b		4.53×10^{-10}
Melting temperature (K), T_m		2303
Material density (g/cc), D		6.24
Molecular weight (g/mol), M		152.111
Pre-exp. lattice diffusion (m ² /sec) ² , D_{ov}		2.0×10^{-6}
Activation energy lattice diffusion (kJ/mol), Q_v		380
Pre-exponent boundary diffusion (m ³ /sec) ³ , D_{ob}		1.81×10^{-15}
Activation energy boundary diffusion (kJ/mol) ⁴ , Q_b	1	244
Pre-exp. core diffusion (m ⁴ /sec), D_{oc}		1.0×10^{-23}
Act. Energy core diffusion (kJ/mol), Q_{core}		244
Grain boundary width (nm), Δ		1
Loose powder relative density ⁵		0.15/0.35
Act. Energy PLC (kJ/mol) ⁶ , Q_{crp}		380
PLC exponent ⁷ , n		1.75
PLC constant, A (MPa ⁻ⁿ sec ⁻¹)		4.432×10^4

¹ If unknown, estimated as: $\gamma_{gb} = \frac{1}{3} \gamma_{surf}$

² $D_{v,b,core}(T) = D_{ov,ob,ocore} \exp\left\{\frac{-Q_{v,b,core}}{RT}\right\}$. The functions for the diffusivities in the material

containing bulk or interface impurities are the same as for the material without the impurities but with the impurity modified activation energies and pre-exponent.

³ If unknown estimated as [26]: $\Delta D_{ob} = 2bD_{ov}$

⁴ If unknown, estimated as [40]: $Q_b = Q_v - N_a \alpha' \gamma_{gb} a_{sv}^2$

⁵ Smaller value for nano region and larger value for coarse pore region.

⁶ The activation energy for creep is usually estimated to be equal to the activation energy for volume diffusion or in the cases of intermetallics estimated as $0.95 Q_{vol}$.

⁷ Smaller value corresponds to $> 0.5T_m$ and larger value to $< 0.3T_m$.

Shear Modulus at 300 K, (MPa) ⁸ , G_0		1.63×10^5
Temperature dependence, $(T_m/G_0) \times (dG/dT)$		0.35
Young's modulus at 300 K, MPa, E		3.79×10^5
Temperature dependence, $\{T_m/E\} \{dE/dT\}$		0.35
Change in surface energy (kJ/mol), $\Delta\gamma_{surf}$		0.1
Change in g.b. energy (kJ/mol) ⁹ , $\Delta\gamma_{gb}$		0.3
α' (interstitial)		1
α' (vacancy)		2
Die-wall friction coefficient ¹⁰ , μ_{dw}		0.2
Interagglomerate friction coefficient, μ_{ia}		0.05
Interparticle friction coefficient, μ_{ip}		0.1
Decreasing pore exponent ¹¹ , m_p		3/8
Density at stage 1 \rightarrow stage 2 ¹²		0.95
Volume fraction (region I), v_f^I		0.8-1
Volume fraction (region II), v_f^{II}		0-0.2
Particle radii (nm), r		25
Agglomerate radii (nm)		150
Pore radii (nm), r_p		25
Interagglomerate pore radii (nm)		150
Grain size (nm), g		50
Die diameter (in), Dia		0.5
Initial compact height in die (in), Ht		0.5
Grain growth exponent ¹³ , m		3.25-14

$$^8 G = G_0 \left[1 - \left(\frac{T - 300}{T_m} \right) \left(\frac{\partial G}{\partial T} \times \frac{T_m}{G_0} \right) \right]$$

⁹ Smaller value is for low impurity case and larger value for high impurity case.

¹⁰ Smaller value for high temperature case. Larger value for low temperature case.

¹¹ Higher value for smaller pores.

¹² For stage 2 of densification, ρ_0 is replaced by ρ_c which is ≈ 0.95 [26].

¹³ Smaller value for fine pore region.

Atomic radii, B (nm) ¹⁴ , a _{su} (B)		-
Atomic radii, O (nm)		0.06
Atomic radii, C (nm)		0.077
Atomic radii, Cu (nm)		-
Molecular radii, Cu ₂ O (nm)		-
Molecular radii, B ₂ O ₃ (nm)		-
Molecular radii, SiO ₂	-	0.3335
Molecular radii, MoO ₂ (nm)	-	0.5
Initial internal gas pressure (MPa) ¹⁵ , P _{int}		10 ⁻⁵ /0.1
C, vacancy-impurity (kJ/mol) ¹⁶		10-50
ΔE, vacancy-impurity (kJ/mol) ⁹		30
λ, fcc		-
λ, bcc, hcp	-	1.0
Segregation factor, b _v , O		-5
b _v , Cu ₂ O		-
b _v , C		-5
Enrichment factor, β _b , Cu ₂ O		-
β _b , B ₂ O ₃		-
Mol fraction solvent, O, X _c (O)		0.001
Mol fraction solvent, C		0.001
Mol fraction solvent, B		-
Mol fraction solvent, Cu ₂ O		-
Mol fraction solvent, B ₂ O ₃		-
Mol fraction solvent, MoO ₂		0.0
Mol fraction solvent, SiO ₂		0.001

¹⁴ If unknown, estimated by: $a_{sv,su} = 0.01 \left(\frac{M}{DN_a} \right)^{1/3}$

¹⁵ Smaller values for vacuum pressing or HIP. Larger values for pressing in Ar atmosphere.

¹⁶ Smaller value for low impurity and larger value for high impurity.

Yield strength, particle (MPa) ¹⁷		3500
Yield strength, agglomerate (MPa)		1000
Temperature dependence		0.3
Yield strength of Ti can (MPa) ¹⁸	-	800
Temperature dependence	-	1.3
Melting temperature of can (K)	-	1941

¹⁷ $\sigma_p = \sigma_o^p \left[1 - \left(\frac{T - 300}{T_m} \right) \left(\frac{\partial \sigma_p}{\partial T} \times \frac{T_m}{\sigma_o^p} \right) \right]$. Yield strength of agglomerate is given by a similar equation, except that the room temperature yield strength and the temperature coefficient of strength are different.

$$^{18} \sigma_y^{can}(T) = \sigma_o^{can} \left[1 - \left\{ \frac{T_m}{\sigma_o^{can}} \times \frac{\partial \sigma_y}{\partial T} \right\} \times \left\{ \frac{T - 300}{T_m} \right\} \right]$$